Solid-State ^{17}O NMR Spectroscopy of Fmoc-Protected Amino Acids

by

Brittney A. Klein

A thesis submitted in partial fulfillment of the requirements for the degree of

Master of Science

Department of Chemistry
University of Alberta

Abstract

Enhancing our understanding of the local structure and dynamics for different components within a biological system is key to unraveling their overall function. Nuclear magnetic resonance (NMR) spectroscopy has become an unparalleled technique for exploring both the structure and dynamics within these types of systems. Traditional NMR experiments have focused on investigating the hydrogen, carbon and nitrogen atoms comprising these systems which has provided us with invaluable information relating biological components to physiological processes and has led to more targeted development of pharmaceuticals. However, oxygen, which is another essential atom found in all biomolecules, has largely evaded incorporation into biomolecular NMR studies due to the only stable, NMR-active isotope of oxygen (^{17}O) having comparatively unfavorable NMR properties. Past solid-state NMR (ssNMR) studies investigating ^{17}O nuclei within biomolecules have faced significant hurdles trying to address the poor resolution and insensitivity associated with detection of this nucleus. Both these problems stem from the fact that ^{17}O has a very low natural abundance (0.034%), a small magnetogyric ratio ($\gamma = -5.774$ MHz T^{-1}) and is a quadrupolar nucleus (I = 5/2). To address these challenges a combination of isotopic enrichment, ultra-high magnetic fields, multidimensional and/or population transfer techniques have been used but implementing these solutions often translates to higher costs and/or longer experimental times. Despite these drawbacks, ^{17}O NMR data has helped to address some of the more intricate issues surrounding the chemical bonding and structural environments in biological systems that are unable to be resolved using traditional NMR experiments.

In this thesis, the ^{17}O NMR parameters for the carboxylic acid moieties in a selection of N-α-fluoren-9-yl-methoxycarbonyl-O-t-butyl (Fmoc)-protected amino acids are characterized using

a combination of isotopic enrichment and ultra-high magnetic fields for the first time. A "one-pot" multiple turnover reaction is utilized to introduce ^{17}O labels into both the carbonyl (C**O**) and hydroxyl (C**O**H) sites of Fmoc-L-isoleucine, Fmoc-L-tryptophan, Fmoc-L-proline, Fmoc-L-tyrosine and Fmoc-L-threonine. Both non-spinning and magic-angle spinning (MAS) ^{17}O solid-state NMR spectra were acquired at 14.1 and 21.1 T and used to extract the relevant quadrupolar and chemical shift parameters. These experimental parameters are then compared with computed NMR parameters determined from density functional theory (DFT) calculations. This work demonstrates key insights that can be gleamed from ^{17}O NMR studies of small molecules including how ^{17}O NMR spectroscopy can be utilized to monitor the protonation of labelled sites and highlights the importance of developing ^{17}O NMR as a probe to study larger biological systems.

Preface

The work presented in this thesis was conducted as original work by Brittney A. Klein. Portions of this thesis were reproduced from Klein, B. A., Tkachuk, D. G. Terskikh, V. V., Michaelis, V. K. (2021). "Expanding the NMR toolkit for biological solids: oxygen-17 enriched Fmoc- amino acids." *New Journal of Chemistry*, 45, 12384-12398 with the permission from the Centre National de la Recherche Scientifique (CNRS) and the Royal Society of Chemistry. I was the lead investigator, responsible for the vast majority of the data collection and analysis, as well as manuscript composition. D.G. Tkachuk performed the majority of the DFT calculations and V. V. Terskikh acquired the ^{17}O NMR data at 21.1 T (NRC, Ottawa). V.K. Michaelis was the supervisory author on this project and was involved throughout the project in concept formation and manuscript edits.

To JNL

Acknowledgements

First and foremost, I would like to thank my supervisor, Professor Vladimir K. Michaelis for the opportunity to work in his group and for providing me with the latitude to select a project that suited my research interests. Your scientific guidance has made learning the ins and outs of this field less daunting and has shown me some of the exciting applications that are possible with solid-state NMR spectroscopy. Also, I would like to say how much I appreciate your leadership and the endless advocating you have done on behalf of your graduate students throughout the pandemic to help keep morale high and research progressing in a timely fashion.

Also, this project would not have been possible without the assistance I received from a multitude of individuals, but I would especially like to thank Dr. Guy Bernard and Michelle Ha for the time they took to train me on the spectrometers and for their willingness and patience to always answer questions. I would also like to recognize Guy for his assistance in editing my manuscript and for his helpful insights and reassurances. A special thanks are extended to both Dylan Tkachuk and Dr. Victor Terskikh for their contributing work on this ^{17}O NMR project. I would also like to thank everyone at the University of Alberta's NMR facility, especially Mark Miskolzie, for his assistance with experimental set up and training on the Agilent spectrometers. Also, I would like to thank both Dr. Ed Fu and Béla Reiz for their help with purification and for performing the mass spectrometry on the samples used herein.

To my committee members, Dr. Alex Brown and Dr. Julianne Gibbs, thank you for your feedback and insights early on that helped to shape my graduate program.

I would like to extend my sincere gratitude to Prof. Brian D. Sykes for sparking my interest in NMR spectroscopy and for creating a welcoming environment where both research and learning were encouraged. My time in your laboratory taught me many of the technical skills I will carry with me throughout my career but also the importance of striking a work-life balance. I would also like to thank Brian for his continued mentorship and all the fruitful discussions we've had over gourmet donuts since commencing my Master's program.

To Dr. Anna Jordan, thank you for jumpstarting my career and providing me with the wonderful opportunity to work alongside one of your former students. Your advice over the years has always served me well and is much appreciated.

Finally, I would like to thank my family and friends. To Mom and Dad, thanks for instilling in me my work ethic and the value of education. To Miranda, thanks for taking the time to check in with me and make sure my sanity was still intact and Courtney, thanks for always being available for coffee to catch up and vent about any weekly woes. To Jen and Rufus, thank you for making home my happy place and tolerating my misdirected work frustrations. All the walks, conversations, and down time with you two made this marathon all that more enjoyable!

Table of Contents

Abstract ..... *ii*

Preface ..... *iv*

Acknowledgements ..... *vi*

List of Tables ..... *x*

List of Figures ..... *xi*

List of Abbreviations and Symbols ..... *xvi*

Chapter 1: Introduction to ^{17}O NMR Spectroscopy in Biological Systems *1*

Overview **1**

1.1 Biomolecular NMR Spectroscopy **1**

1.2 ^{17}O NMR Spectroscopy of Biological Systems **4**

1.2.1 ^{17}O Enrichment Methodologies and Other Sensitivity Enhancement Techniques 4

1.2.2 Techniques for Enhancing Resolution in ^{17}O ssNMR Studies 7

1.3 Recent Advances in ^{17}O NMR Spectroscopy **8**

1.4 Thesis Outline **9**

Chapter 2: Introduction to NMR Spectroscopy *11*

Overview **11**

2.1 NMR Basics for Quadrupolar Nuclei **11**

2.2 Anisotropic Nuclear Spin Interactions **15**

2.2.1 Chemical Shielding Interaction 16

2.2.2 Quadrupolar Interaction 18

2.3 NMR Experiments for Quadrupolar Nuclei **22**

2.3.1 Traditional Solid-State NMR Techniques 22

2.4 Quantum Chemical Calculations and Simulations of NMR Parameters **24**

2.4.1 Simulation of Quadrupolar NMR Spectra 24

2.4.2 Computation of NMR Parameters 24

2.4.3 Visualizing Euler Angles 25

Chapter 3: Solid-State NMR Spectroscopy and Quantum Calculations of ^{17}O-enriched Fmoc-Amino Acids *27*

Overview **27**

3.1 Methods **27**

3.1.1 ^{17}O Enrichment of Fmoc-Amino Acids 27

3.1.2 Solid-State NMR Spectroscopy 28

3.1.3 Quantum Chemical Computations 29

3.2 Results and Discussion **31**

3.2.1 Percent Enrichment of Fmoc-Amino Acids 31
3.2.2 Experimental ^{17}O NMR Spectra 33
3.2.3 Quantum Chemical Computations of ^{17}O Fmoc-Amino Acids 42
3.3 Summary of Results 51
Chapter 4: Concluding Remarks and Future Work 52
4.1 Conclusions 52
4.2 Future Directions 52
References 54

List of Tables

Table 1. Selection of basis sets for computing NMR parameters using density functional theory on crystal structure of FMOC-L-tyrosine, monohydrate. 29

Table 2. Comparison of the computed ^{17}O NMR parameters for Fmoc-L-tyrosine and -isoleucine obtained using their reported crystal structures with those obtained using different geometry-optimized structures. 30

Table 3. Density functional theory computed NMR parameters on geometry-optimized structures. 31

Table 4. Experimental and Computed ^{17}O NMR Parameters of Fmoc-Amino Acids. 35

Table 5. Average deviations of the computed vs. experimental ^{17}O NMR parameters plotted in Figures 3.8 & 3.9 for the C**O** and C**O**H sites in the Fmoc-amino acids. 43

List of Figures

Figure 1.1 Comparison of the ^{1}H NMR spectra of Fmoc-tyrosine acquired in solution and as a powder (inset). The ^{1}H NMR spectrum of Fmoc-tyrosine acquired in acetonitrile-d_3 (asterisk) on a 500 MHz spectrum (bottom) and the ssNMR spectrum of Fmoc-tyrosine obtained on a 300 MHz spectrometer with 13 kHz MAS (inset). 2

Figure 1.2 Mechanism of multiple-turnover reaction for ^{17}O enrichment of a Fmoc-protected amino acid.[45,46] Under $N_{2\,(g)}$, a Fmoc-amino acid is added to round bottom flask with a molar excess of pyridine hydrobromide and a carbodiimide in N,N-dimethylformamide (20 equivalents and 10 equivalents, respectively). The pyridine initially activates the carbodiimide by acting as a dry proton source, lowering the pH of the solution. It also helps prevent racemization of the O-acylisourea intermediate. An excess of 40% $H_2{}^{17}O$ is then added to hydrolyze the reaction intermediates and produce a protected amino acid with a single ^{17}O site. Additional carbodiimide is added to the reaction mixture to drive more cycles which subsequently leads to a second ^{17}O site being labelled. 6

Figure 1.3 Timeline of significant contributions relating to the study of biological systems using ^{17}O NMR spectroscopy. The figure was reproduced from an article published by Munjyppan, S., et. al. (2021).[82] 8

Figure 2.1 Depiction of nuclear spins in the absence and presence of an external magnetic field, B_0 (a) and the corresponding effect of B_0 on the energy levels for a spin ½ nucleus (b). Nuclear spins are randomly oriented in the absence of B_0 (a, left panel) but in the presence of B_0, the bulk of the nuclear spins will align in the direction of the magnetic field to generate a net magnetization along the z-axis (a, right panel). When no B_0 is present, the two energy levels for $I = ½$ are degenerate and all nuclear spins have the same energy. When subjected to a B_0, these energy levels no longer are degenerate and a small population difference is created. The energy difference between spin state scales linearly with B_0 and is dependent on the nucleus being investigated (b). 13

Figure 2.2 Schematic of a Bloch pulse used for acquiring a 1D NMR experiment. A calibrated 90º radiofrequency pulse is used to place the bulk magnetization generated from the precession of nuclear spins in B_0 into the x-y plane. The acquisition of the FID occurs over a given time and records the relaxation of the system back to equilibrium and is Fourier transformed to yield a spectrum in the frequency domain. 15

Figure 2.3 Deviation of the nuclear charge distribution.[113] A spherical charge distribution is present for spin ½ nuclei as they do not have an intrinsic quadrupolar moment (Q = 0) or in highly symmetric systems. The non-spherical distortion of the nuclear charge can adopt either a prolate or oblate geometry which interacts with the EFG and results in an non-zero C_Q. ……. 19

Figure 2.4 Energy splitting diagram for a I = 5/2 nucleus and the respective perturbations due to $\mathcal{H}_Q^{(1)}$ and $\mathcal{H}_Q^{(2)}$ on the Zeeman splitting of the central transition (½ ↔ -½, yellow) and satellite transitions (purple). When B_0 = 0 (red circle), only the pairs of spin states will be degenerate in energy (b). When $B_0 > 0$, the Zeeman interaction, $\mathcal{H}_Z$, usually dominates and cause each spin state to be spaced by the Larmor frequency, ν_L. $\mathcal{H}_Q^{(1)}$ will impact the transition frequencies of the satellite transitions (purple) but will not change the central transition. Incorporating the effects of $\mathcal{H}_Q^{(2)}$ on the energy splitting diagram, the central transition is now impacted and will no longer be spaced by ν_L (c). …….. 21

Figure 2.5 Schematic of a Hahn-echo pulse sequence and the impacts of the sequence on the bulk magnetization (red arrow) created by placing NMR active nuclei in B_0 (blue arrow).[124] After being placed in B_0 for a sufficiently long time, the bulk magnetization will be aligned along the z-axis (a). After the system has reached this equilibrium state, a $\frac{\pi}{2}$ pulse is used to place the magnetization into the transverse plane (b) which with start to dephase over the first time delay, t_1 (c). A π is then used to flip the dephased magnetization (d) and the magnetization will now refocus along the -y axis over the second time delay, t_2 (e). This allows for the acquisition of an echo and this pulse sequence can be repeated once the system has relaxed back to equilibrium (a) . …….. 22

Figure 2.6 Relative orientation of the EFG and CSA tensor components computed for the carbonyl oxygen in Fmoc-L-isoleucine using EFGshield.[139] Initially the tensor components are coincident with each other. The above is a depiction of what occurs when the PAS of the CSA tensor is rotated away from the EFG PAS. The first counterclockwise rotation which is about the δ_{33} component is described by the angle α. Next, a rotation about the newly orientated δ_{22} component by angle, β= 90º places the δ_{33} component nearly parallel to the V_{yy} tensor. A third counterclockwise rotation about the δ_{33} component by γ = 51º leads to the final orientation of tensor components characterized by the Euler angles, α, β and γ. …….. 26

Figure 3.1 Mass spectrum of Fmoc-L-isoleucine after precipitation in acetonitrile and water. The expected MW for Fmoc-L-isoleucine is 353.41 Da and the $[M+H]^+$ series shown in the spectrum have an

additional +23 Da due to the presence of Na^+. The α-COOH can have a mixture of contributions from $^{16}O/^{16}O$ at 376.3 m/z, $^{16}O/^{17}O$ or $^{17}O/^{16}O$ at 377.3 m/z, $^{17}O/^{17}O$ or $^{16}O/^{18}O$ or $^{18}O/^{16}O$ at 378.2 m/z, $^{18}O/^{17}O$ or $^{17}O/^{18}O$ at 379.2 and $^{18}O/^{18}O$ at 380.1 m/z …….. 32

Figure 3.2 Experimental (black) and simulated (blue) oxygen-17 NMR spectra of 40% labelled Fmoc-L-isoleucine acquired at 21.1 and 14.1 T of MAS (a) and non-spinning (b) samples. The structure of Fmoc-L-isoleucine is shown above the MAS spectra and the peaks are assigned to the hydroxyl (purple) and carbonyl site (green) of the carboxylic acid moiety. The MAS NMR spectra were obtained using spinning frequencies of 22 or 23.5 kHz, respectively and the spinning sidebands are indicated with asterisks. The simulations of the ^{17}O sites in the non-spinning spectra (b) are shown for the individual CO (green) and COH (purple) sites and overlaid with the entire simulated spectrum (blue). The MAS and stationary spectra were calculated with WSOLIDs and the NMR parameters are reported in Table 4. …..… 34

Figure 3.3 ^{17}O NMR spectra of Fmoc-L-tryptophan acquired at 21.1 and 14.1 T. The experimental (black) and simulated (blue) MAS spectra with an inset of the structure of Fmoc-L-tryptophan are shown in (a). The two labelled oxygen sites of the protected amino acid are indicated with a purple (hydroxyl) and green (carbonyl) circle in both the structure and above the spectrum. The spinning side bands are indicated with asterisks and the signal due to residual water is denoted with a red triangle at 0 ppm. The stationary spectra of Fmoc-L-tryptophan are shown in (b) and the individual CO (green) and COH (purple) sites are overlaid with the entire simulated spectrum (blue). The NMR parameters used for simulating these spectra are reported in Table 4. …….. 37

Figure 3.4 Experimental (black) and simulated (blue) ^{17}O NMR spectra of Fmoc-L-proline. Spectra for both the MAS (a) and stationary (b) samples were acquired at 21.1 and 14.1 T. The structure of Fmoc-L-proline (inset on a) shows the two isotopically enriched sites of the protected amino acid and the peaks attributed to the hydroxyl (purple circle) and carbonyl (green circle) oxygens are shown above the MAS spectra. The spinning side bands (asterisks) are visible in the experimental MAS spectra, along with a broad peak (yellow circle) likely corresponding to the carboxylate ion. The simulations of the ^{17}O sites in the non-spinning spectra (b) are shown for the individual CO (green) and COH (purple) sites and are overlaid with the entire simulated spectrum (blue) at both magnetic field strengths. …….. 38

Figure 3.5 Experimental (black) and simulated (blue) ^{17}O NMR spectra of Fmoc-L-tyrosine (a,b) and Fmoc-L-threonine (c,d) at 21.1 T. The structure of each amino acid is inset above the corresponding MAS spectrum (a,c) and the hydroxyl (purple circle) and carbonyl (green

circle) peaks are indicated along with the spinning sidebands (asterisks). The experimental MAS spectrum in (a) shows an additional peak at ~ 240 ppm (yellow circle) whereas a ZrO_2 peak is visible (orange diamond) in (c). The stationary spectra at 21.1 T are shown in (b) and (d) with the simulation of the CO (green) and COH (purple) sites overlaid with the entire simulated spectrum (blue). All parameters used to simulate the spectra are included in Table 4. …….. 40

Figure 3.6 Experimental (black) and computed (blue) MAS NMR spectra of lyophilized (a) and recrystallized Fmoc-L-threonine (b) acquired at 21.1 T. The CO (green circle) and COH (purple circle) ^{17}O NMR parameters are as follows: δ_{iso} = 343 and 174 ppm, C_Q = 8.5 and 7.4 MHz and η = 0.50 and 0.40, respectively, for the lyophilized sample (a) and δ_{iso} = 311 and 192 ppm, C_Q = 8.1 and 7.2 MHz and η = 0.05 and 0.08, respectively, for the recrystallized sample (b). The orange diamond in (b) indicates ^{17}O signal from the ZrO_2 from the NMR rotor and the coloured asterisks indicate spinning sidebands. …….. 41

Figure 3.7 Simulation of non-spinning NMR spectra at 17.6 T for Fmoc-L-leucine (a) and Fmoc-L-valine (b) using the ^{17}O NMR parameters reported from Keeler *et al.* (2017). Spans (Ω) for the C**O** site were amended to 530 and 540 ppm, respectively. All other NMR parameters are identical to what are reported in Table 4. …….. 42

Figure 3.8 Comparison of the computed and experimental ^{17}O CSA tensor components (a, b) and the predicted EFG and CSA tensor orientations (c, d) for Fmoc-amino acids. The tensor components for Fmoc-L-isoleucine, tryptophan, proline, tyrosine and threonine from this study and the experimental data for Fmoc-L-serine, alanine, valine and leucine from previously published results were used to construct these plots.[46,143] The amended span values for the C**O** site of Fmoc-L-leucine and Fmoc-L-valine[46] were used to extract the experimental CSA tensor components. All computed and experimental ^{17}O NMR parameters are summarized in Table 4. The relative orientations of the EFG (blue) and CSA (red) tensors for the five geometry-optimized structures at either the C**O** (c) or C**O**H site (d) are shown. There are three similar orientations for each site corresponding to one of the Fmoc-amino acids, which is denoted below the figure. The V_{yy} tensor component is oriented out of the page and in (c) the δ_{33} are coincident with V_{yy} in all structures and in (d) the δ_{22} component overlaps with the V_{yy}. …….. 44

Figure 3.9 Comparison of the computed and experimental ^{17}O NMR parameters for the isotropic chemical shift (a), span (b) and skew (c) along with the C_Q (d) and EFG tensor components for the CO (e) and COH site

(f) for the FMOC amino acids listed in Table 4. The average deviations of the computed values compared to the experimental NMR parameters are listed in Table 5. The light green markers in (b) indicate published span parameters for the CO site of Fmoc-L-leucine and -valine[45] with error bars to re-evaluated span values (Fig. 3.7). In (e) and (f) the trend lines have a slope of 1 and the q_{ii} components were extracted from the C_Q (eqn. 2.18) and η (eqn. 2.19) values. …….. 45

Figure 3.10 Correlation of the intramolecular hydrogen bond distance between the NH and C=O group from X-ray structures with the experimental CSA tensor components for the carbonyl oxygen site. X-ray structure of Fmoc-L serine (CIF-4514078), -tyrosine (CIF-7220755), -isoleucine (CIF-2219071) and -leucine (CIF-2218405) were used to measure the distance between the C=O and H-N groups in each molecule. The linear correlations are as follows : δ_{11} ($y = 56.5x + 376.6$, $R^2 = 0.99$), δ_{22} ($y = -45.0x + 543.2$, $R^2 = 0.71$), δ_{iso} ($y = 7.3x + 311.4$, $R^2 = 0.93$) and δ_{33} ($y = 10.4x + 14.5$, $R^2 = 0.24$). …….. 49

Figure 3.11 Simulated MAS NMR spectra of deprotonated (red) and protonated (black) Fmoc-L-tyrosine (a) and Fmoc-L-isoleucine (b) at 14.1 T. Deprotonated spectra were simulated using new computed NMR parameters for δ_{iso} and C_Q after a proton was removed from the original geometry-optimized structures. The asymmetry values (η) were held constant between both species and the δ_{iso} and C_Q for the CO (green circle) and COH (purple circle) sites in the protonated FMOC-amino acids are reported in Table 4. …….. 50

List of Abbreviations and Symbols

B'	Local magnetic field
k_B	Boltzmann constant, 1.3805×10^{-23} J/K
γ	Magnetogyric ratio
η	Nuclear quadrupole asymmetry parameter
κ	Skew of chemical shift tensor
α,β,γ	Euler angles defining the relative orientations between tensors
δ_{ii}	Principal components of chemical shift tensor, where ii = 11, 22, 33
σ_{ii}	Principal components of the chemical shielding tensor, where ii = 11, 22, 33
δ_{iso}	Isotropic chemical shift
σ_{iso}	Isotropic magnetic shielding
ν_L	Larmor frequency
ν_r	Rotor spinning frequency
^{17}O	Oxygen-17, (NA=0.038%, Q = –2.558 fm^2)
ADF	Amsterdam Density Functional
B_0	Static magnetic field
C_Q	Quadrupole coupling constant
CSA	Chemical shift anisotropy
CT	Central transition
DFT	Density functional theory
DNP	Dynamic nuclear polarization
EDC-HCl	N-(3-Dimethylaminopropyl)-N'-ethylcarbodiimide hydrochloride
EFG	Electric field gradient

FID	Free induction decay
Fmoc	N-α-fluoren-9-yl-methoxycarbonyl-O-t-butyl
h	Planck's constant, 6.6260×10^{-34} m^2kg/s
$\hbar$	Reduced Planck's constant, equivalent to $h/2\pi$
I	Nuclear spin quantum number
MAS	Magic angle spinning, $\theta = 54.74°$
m_I	Magnetic spin quantum number
NMR	Nuclear magnetic resonance
SOQB	Second-order quadrupolar broadening
ssNMR	Solid-state nuclear magnetic resonance
ST	Satellite transition
TPPM	Two-pulse phase modulated
TZ2P	Triple-zeta doubly-polarized
V_{ii}	Principal components of the electric field gradient tensor, where ii = xx, yy, zz
V_{zz}	Largest component of the EFG tensor
Z	Atomic number
ZORA	Zeroth-order regular approximation
μ	Magnetic moment

Chapter 1: Introduction to ^{17}O NMR Spectroscopy in Biological Systems

Overview

Nuclear magnetic resonance (NMR) spectroscopy has proved to be a powerful tool for the study of structure and dynamics in biological entities. It has allowed for the examination of molecular-level interactions and has propelled our understanding of how these systems function. However, conventional biomolecular NMR studies have focused predominantly on nuclei with a nuclear spin (I) of ½ which have a high natural abundance (^{1}H, ^{31}P and ^{19}F) or can be easily introduced into recombinant or synthetic biomolecules (^{13}C,^{15}N). This chapter will briefly discuss why studying biomolecular systems using NMR is important, the difficulties encountered trying to introduce oxygen-17 (^{17}O) solid-state NMR spectroscopy into biological studies, as well as some techniques adopted to resolve these issues. Finally, the chapter will conclude by highlighting some of the recent findings that have occurred using ^{17}O NMR spectroscopy, reinforcing why development in this area is integral to the future of biological studies.

1.1 Biomolecular NMR Spectroscopy

Nuclear magnetic resonance spectroscopy is a robust analytical spectroscopic method that has been paramount in unveiling how biomolecular systems function through the study of their unique molecular structure and dynamics. Early studies initially focused on 1D ^{1}H NMR spectra of small biomolecules in solution.[1,2] These spectra were often complicated by the numerous overlapping peaks and strong solvent signals. Milestones in biomolecular NMR studies were reached as multi-dimensional NMR, solvent suppression and isotopic enrichment techniques were developed.[3–11] These techniques helped to revolutionize the field as they allowed researchers to obtain high-resolution NMR spectra. Peaks that were once obscured could now be resolved from the overwhelmingly large solvent signals and correlated with other neighbouring residues within the system. These experiments could also now be performed in a timely manner as the number of NMR-active nuclei could be increased using labelling protocols. This quickly gave way to the determination of structures entirely by NMR spectroscopy and to date, there exists ~13,600 biological structures (Protein Data Bank (PDB); http://www.rcsb.org/pdb/; accessed Jan. 4 2022) that have been elucidated using this technique.

Solution NMR spectroscopy has the advantage of allowing the determination of the structure for systems that are in a close approximation of their native environment and can provide information on their response to external stimuli like ion concentration, pH and the introduction of small molecules and other proteins. However, not all biological systems are amenable to study in solution. For instance, the study of high molecular weight and insoluble systems such as membrane proteins,[12] fibrils[13,14] and biopolymers[15] are often studied using solid-state NMR (ssNMR) spectroscopy. When studying a biomolecular solid using NMR techniques, anisotropic interactions have to be considered.[16] These additional interactions, which are often attenuated in solution, result in peaks in the NMR spectrum that are broadened in comparison. A consequence of this additional broadening is reduced resolution of individual peaks in the ssNMR spectrum. This is most pronounced when comparing the ^{1}H NMR spectra obtained for molecules in solution

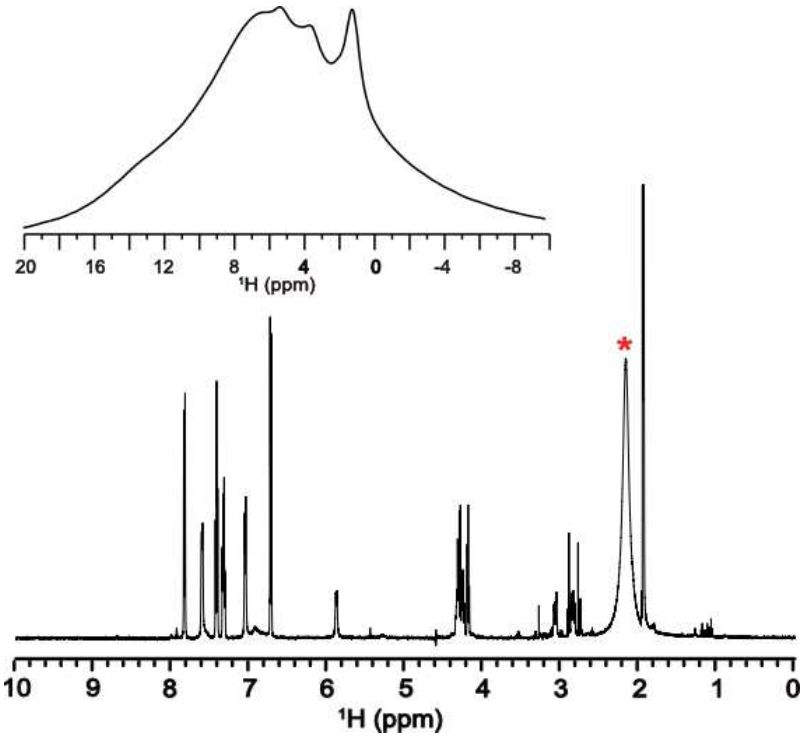

Figure 1.1. Comparison of the ^{1}H NMR spectra of Fmoc-tyrosine acquired in solution and as a powder (inset). The ^{1}H NMR spectrum of Fmoc-tyrosine acquired in acetonitrile-d_3 (asterisk) on a 500 MHz spectrometer (bottom) and the ssNMR spectrum of Fmoc-tyrosine obtained on a 300 MHz spectrometer with 13 kHz MAS (inset).

and as a powder. Figure 1.1 shows the difference between the ^{1}H NMR spectra for Fmoc-tyrosine obtained in solution and as a powder. ^{1}H ssNMR spectra are usually impacted by strong ^{1}H-^{1}H dipolar couplings which hinders the resolution of these peaks and can impede structure determination. Nevertheless, advancements to ^{1}H-detection in solids have been made in the last decade and include major developments in fast magic-angle spinning (MAS) probe hardware, higher magnetic fields (≥ 1 GHz), pulse sequence designs and deuteration strategies.[17–19]

Even with the added challenges involved with exploring biological systems using ssNMR spectroscopy, significant insights have been unveiled from these studies which have contributed to our understanding of how structure can be linked with function. One such example is the study of the motion of aromatic rings.[20–23] The sidechains of some amino acids are composed of aromatic rings and can be highly dynamic. The motion of these functional groups is difficult to detect in solution due to the overall tumbling of the molecule and can require site specific labelling.[24–26] However, ssNMR studies can mitigate these issues and have been used to propose a mechanism for the modulation of the protons within the M2 protein of the influenza virus.[21,22] The regulation of the proton concentration in this protein has been linked with the pH dependent ring reorientations of histidine, which helps to shuttle protons into the virus.[21,22] This mechanism has important ties with the virus' ability to replicate and as such the underpinnings of these small structural changes can have enormous implications in the development of new therapeutics.

As mentioned above, NMR spectroscopy is at the forefront of the techniques used for resolving the structures of biomolecules. One advantage when comparing structures that have been determined by ssNMR spectroscopy to structures determined using other techniques, like X-ray diffraction, is the system being studied does not have to be crystalline. A non-crystalline sample can be used for ssNMR studies and smaller components of the system can be evaluated in solution, permitting solubility. NMR structures also have the benefit of being able to ascertain the positions of proton, nitrogen and carbon nuclei. In contrast, X-ray diffraction cannot accurately determine the position of protons due to the low electron density of this atom but can be used to clearly identify the position of oxygen atoms. A synergy between these two techniques exists, where identical structures or fragments of a larger system are superimposed over a pre-existing NMR or X-ray structure and used to validate results and identify potential differences.[27–29] However, if NMR spectroscopy could reliably establish the position of oxygen atoms, a single technique could

be used to provide a comprehensive framework for biological systems and potentially yield new insights into their function by correlating the oxygen atoms to other nuclei and solvent molecules within the system.

1.2 ^{17}O NMR Spectroscopy of Biological Systems

Although there has been tremendous success in examining the interactions between carbon, nitrogen and hydrogen atoms within biomolecules, oxygen, a critical element in these systems, has struggled to be incorporated into NMR studies due to its inherent low sensitivity and resolution. The low sensitivity of oxygen is a result of the only stable, NMR-active isotope, oxygen-17 (I=5/2), having a very low natural abundance (0.037%), a moderate quadrupole moment (Q, -2.558 fm^2) and a small magnetogyric ratio (γ = -5.774 MHz T^{-1}). This makes ^{17}O NMR spectroscopy nearly a million times less sensitive than ^{1}H NMR spectroscopy. Additionally, the quadrupolar nature of this nucleus diminishes the resolution when multiple sites are present due to the complex line shapes associated with second-order quadrupolar broadening (SOQB). Nevertheless, if these challenges are mitigated, ^{17}O NMR spectroscopy can provide a wealth of structural and dynamic information about intra- and intermolecular interactions and chemical bonding that are difficult to discern from other conventional techniques such as diffraction.

1.2.1 ^{17}O Enrichment Methodologies and Other Sensitivity Enhancement Techniques

Provided that NMR spectroscopy requires a large number of spins to create a sizable population difference to detect a signal, it is considered an insensitive technique compared to other spectroscopic methods. This insensitivity is accentuated when working with low gamma, low natural abundance nuclei like ^{17}O. One way to tackle this sensitivity issue is through isotopic enrichment. Conventional biomolecular NMR studies have extensively developed methods to introduce I = 1/2 nuclei like ^{13}C and ^{15}N into recombinant or synthetic biomolecules.[5–7] However, the introduction of ^{17}O into these types of systems is much less routine. This is due to the small selection of commercially available starting materials that contain ^{17}O and the high cost associated with purchasing these precursors ($100's-1000's/mL for $H_2{}^{17}O$).[30] The first attempts to introduce an oxygen isotope into biomolecules occurred in the late 1950's and was followed by ^{18}O enrichment of proteins in the 1960's.[31,32] This undoubtedly demonstrates the early interest researchers had in studying the changes to oxygen environments that are integral in biological

systems. Yet, the development of a scalable and selective method for ^{17}O enrichment of the α-COOH site in protected amino acids did not occur for another 20 years.[33]

The first mechanism widely adopted for ^{17}O-labelling of the α-COOH site in amino acids used an acid-catalyzed approach.[33] This approach requires the amino acids to be heated and subjected to HCl(g) for an extended period of time. This method has successfully been utilized for ^{17}O enrichment of not only amino acids[34] but other small molecules as well.[35–37] This protocol is still widely used today to incorporate ^{17}O into larger biological systems,[38,39] but the stringent experimental conditions prevents enrichment of some protected amino acids. In response to these rather harsh experimental conditions, an alternative synthetic protocol was developed to label protected amino acids by hydrolysis of their ester derivatives.[40] Although, this reaction proceeds under milder conditions, only one equivalent of $H_2{}^{17}O$ reacts with a single oxygen site of the carbonyl group, making it less cost effective than the acid catalyzed protocol. To try and minimize the amount of ^{17}O precursor required, procedures using mechanochemistry have recently emerged.[41–44] This route for enriching biomolecules with ^{17}O easily uses the least amount of labelling precursor but falters by comparison in the percent of ^{17}O that is incorporated into the final product.[41–44]

A final technique for ^{17}O-enrichement that has been optimized for labelling the carboxylic acid group in protected amino acids is the multiple-turnover reaction.[45–49] Using this type of reaction, a Fmoc- or Boc-protected amino acid can be labelled using a "one-pot" synthesis approach. This reaction proceeds at room temperature and takes only 24 hours to obtain high labelling efficiency. Figure 1.2 shows the mechanism for this reaction after one round. In this reaction, the carbodiimide will react with the carboxylic acid group to form an O-acylisourea intermediate that can be hydrolyzed by the ^{17}O enriched water. Since this reaction occurs numerous times, oxygens at both sites will eventually be exchanged and generate products that are doubly labelled (α-$C^{17}O^{17}OH$). This requires there to be an excess of $H_2{}^{17}O$ precursor over all other reagents and for the reaction to be conducted under $N_{2(g)}$. Despite these two drawbacks, the return of ^{17}O-enriched products that have nearly the same percent ^{17}O as the precursor makes this a superior approach for introducing ^{17}O into protected amino acids.

Although coupling isotopic enrichment with a variety of population transfer techniques[46,50–54] has been utilized in the past to assist with the issue of low ^{17}O sensitivity, notable advancements for enhancing ^{17}O sensitivity in ssNMR studies has been achieved using dynamic nuclear polarization (DNP). DNP is a technique that transfers polarization from unpaired electrons to other nuclei, resulting in sensitivity gains that can drastically reduce NMR experiment times.[55,56] To date, both direct and indirect DNP have been used to explore the ^{17}O environments within inorganic[57–63] and biological systems.[64–66] A DNP study of a series of biologically relevant small molecules measured ^{17}O enhancements > 100, which corresponds to significant NMR time savings (> 10 000 -fold).[65] As DNP techniques develop and instruments become more accessible,[67] it will undoubtedly help in addressing the sensitivity issues that currently pose a major challenge in ^{17}O ssNMR studies.

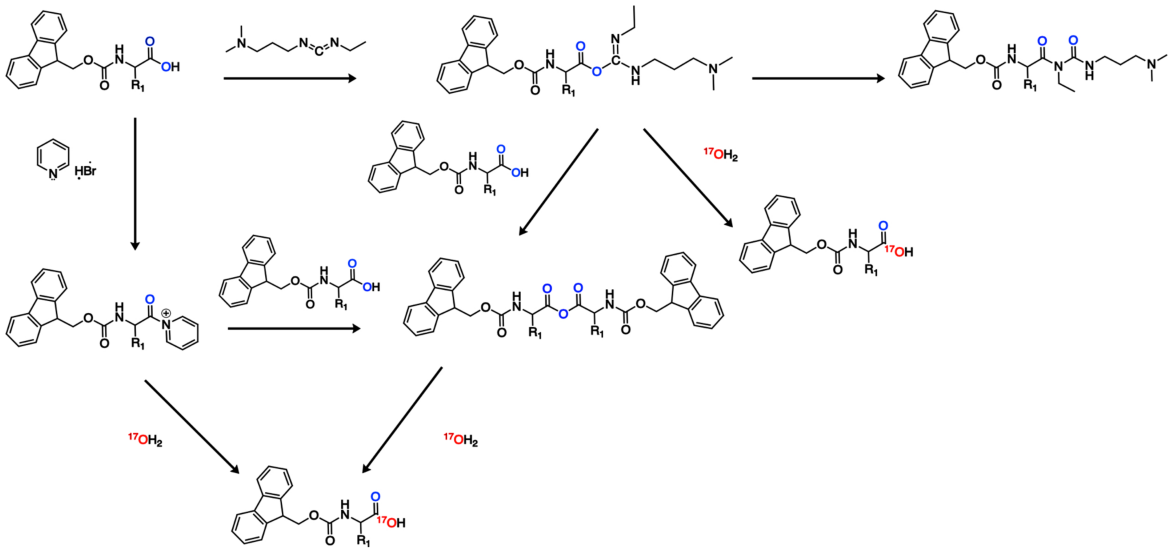

Figure 1.2. Mechanism of multiple-turnover reaction for ^{17}O enrichment of a Fmoc-protected amino acid.[45,46] Under $N_{2(g)}$, a Fmoc-amino acid is added to round bottom flask with a molar excess of pyridine hydrobromide and a carbodiimide in N,N-dimethylformamide (20 equivalents and 10 equivalents, respectively). The pyridine initially activates the carbodiimide by acting as a dry proton source, lowering the pH of the solution. It also helps prevent racemization of the O-acylisourea intermediate. An excess of 40% $H_2{}^{17}O$ is then added to hydrolyze the reaction intermediates and produce a protected amino acid with a single ^{17}O site. Additional carbodiimide is added to the reaction mixture to drive more cycles which subsequently leads to a second ^{17}O site being labelled.

1.2.2 Techniques for Enhancing Resolution in ^{17}O ssNMR Studies

A benefit to ^{17}O NMR studies is the large chemical shift range that is observed for this nucleus in different chemical environments. It is ~4× larger than ^{13}C, spanning ~1000 ppm, and can provide sufficient resolution of common biological functional groups like carbonyls (270 to 350 ppm, -C**O**), carboxylic acids (160 to 260 ppm, -CO**O**H), alcohols (50 to 110 ppm, -**O**H) and water molecules (35 to -5 ppm, H_2**O**).[68] This yields clearly resolved peaks when only a single ^{17}O nucleus is present in each environment. With the objective to investigate ^{17}O within biological systems, one would expect a more complicated spectrum if several ^{17}O nuclei were introduced to these samples. Having several ^{17}O nuclei present would yield an NMR spectrum with overlapping peaks as most of the oxygens are in similar chemical environments. This spectral crowding is further accentuated by the second-order quadrupolar broadening which cannot be averaged with magic angle spinning (MAS). One of the simplest solutions used to improve resolution in any NMR experiment is to perform the experiment at higher magnetic field strengths (B_0).[69–71] Access to higher B_0 has become more feasible for users through the development and commercialization of ultrahigh field superconducting NMR magnets (800 to 1200 MHz). Further discussion on the benefits of going to a higher B_0 for ^{17}O ssNMR studies is presented throughout this dissertation.

In the past, accessing larger a B_0 was challenging and as a result other techniques to improve resolution for quadrupolar nuclei were developed. For instance, variations to MAS techniques such as double-rotation (DOR) and dynamic angle spinning (DAS) were created and have been used successfully to resolve multiple ^{17}O sites in amino acids[34] and small molecules.[35,72] DOR was introduced in 1988 to assist in averaging out the higher order spatial terms present in anisotropic interactions.[73] The preface of this techniques was to have simultaneous spinning of the sample at the magic angle (54.74º) and 30.56º or 70.12º. This technique requires a specialized probe which has prevented it from becoming more commonplace for enhancing resolution. Alternatively, techniques like multiple quantum MAS (MQMAS)[74] and satellite transition MAS (STMAS)[75] have yielded well-resolved isotropic ^{17}O peaks in amino acids, dipeptides and structural water.[46,50–53] These experiments were introduced in the mid-1990's and early 2000's, respectively and yield 2D NMR spectra with a projection of the isotropic peak along one dimension. Unfortunately, both MQMAS and STMAS perform less efficiently as the quadrupole coupling constant (C_Q) increases past 5 MHz.[76,77] This poses a problem when studying

biomolecules as the C_Q typically ranges between 7 and 12 MHz for the different oxygen sites found in these systems.[34,71]

1.3 Recent Advances in ^{17}O NMR Spectroscopy

The continual development of resolution and sensitivity enhancing measures have helped balance the expense and long experimental times related with detecting ^{17}O nuclei and have been extensively reviewed in literature.[69–71,78–81] Using a combination of these measures has allowed ^{17}O NMR studies to flourish and Figure 1.3 depicts a timeline of some notable milestones achieved relating to biomolecular studies.[82] Perhaps one of the most anticipated applications in ^{17}O NMR spectroscopy was to study the ^{17}O environments within a protein. This was successfully done for the first time in 2020, where specific ^{17}O-labelled amino acids were introduced into recombinant yeast ubiquitin to yield both ^{17}O backbone and side chain NMR signals.[38] Lin *et al.* (2020)[38] combined their labelling approach with an ultrahigh magnetic field (1.5 GHz) to sufficiently resolve the ^{17}O NMR signals within their recombinant protein and showed how the large chemical shift range associated with ^{17}O can be useful in measuring the pKa at these sites.

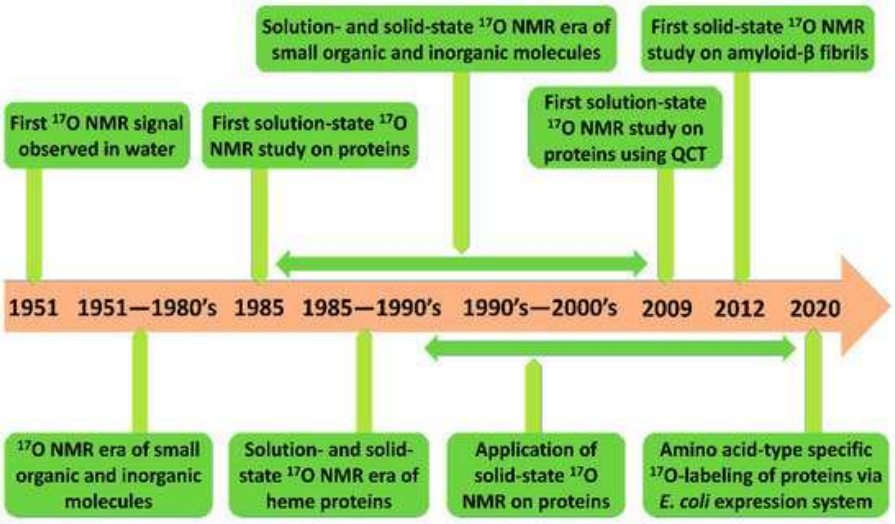

Figure 1.3. Timeline of significant contributions relating to the study of biological systems using ^{17}O NMR spectroscopy. The figure was reproduced from an article published by Muniyappan, S., *et al.* (2021).[82]

Our understanding of hydrogen bonding interactions in biological systems has also significantly been improved by using ^{17}O ssNMR spectroscopy as an investigative tool.[44,46,68,83–85]

One such study by Paulino and co-workers combined ultrahigh magnetic field strengths (1.5 GHz, ^{1}H) with the sensitivity of ^{17}O as a probe to reveal the dynamics of hydrogen bonds formed between water wires within the membrane protein, gramicidin A.[39] Applying correlation experiments to ^{17}O ssNMR studies to extract structural parameters has also been an area that has seen momentous development. These experiments have been beneficial in elucidating ^{15}N-^{17}O, ^{13}C-^{17}O bond lengths, ^{1}H-^{17}O dipolar couplings and ^{1}H-^{17}O, ^{13}C-^{17}O,^{15}N-^{17}O scalar couplings.[46,49,86–90] Recently, modifications to 2- and 3-dimensional correlation experiments have shown improved resolution can be achieved for different ^{17}O sites in co-crystals of biomolecules.[91] However, typically only a single site/residue is tagged with an ^{17}O label and multiple sites are investigated by sequentially labelling residues. Keeler *et al.* (2017) were the first to label multiple sites within a dipeptide[46] and the logical next step would be to increase the number of ^{17}O nuclei introduced into a sample. This will require the use of strategic labelling protocols to maintain a high percent of incorporation of the ^{17}O label and to have sufficient resolution of each site. With the current advances in ^{17}O NMR spectroscopy, addressing these requirements is well within reach and has ideally positioned this area of NMR spectroscopy to be the next to revolutionize our understanding of complex biological systems.

1.4 Thesis Outline

NMR spectroscopy has been a pivotal technique used by chemists and biochemists to unravel the structure and dynamics for a multitude of biological systems. Both solution and solid-state NMR spectroscopy have helped play a role in characterizing small molecules, peptides, proteins, fibrils and biomaterials. All the current developments in isotopic enrichment protocols, as well as in sensitivity and resolution enhancing techniques have shown the drive to mainstream ^{17}O NMR spectroscopy for biological studies. The remainder of this dissertation focuses on my work extending the multiple turnover reaction as an efficient ^{17}O labelling technique for Fmoc-amino acids and their characterization using ^{17}O ssNMR spectroscopy and quantum chemical calculations. Chapter 2 delves into some of the basics of NMR spectroscopy and the anisotropic interactions that are of importance in ^{17}O ssNMR spectroscopy. This is followed by Chapter 3 which details the experimental NMR results obtained from combining isotopic enrichment and multiple magnetic field strengths to study a selection of Fmoc-amino acids and compares these findings with the computed ^{17}O NMR parameters achieved from quantum chemical calculations

performed on a single molecule. Finally, Chapter 4 provides a summary of this work and how it can be used to contribute to future ^{17}O studies.

Chapter 2: Introduction to NMR Spectroscopy

Overview

Spectroscopy is the study of how electromagnetic radiation interacts with matter. NMR spectroscopy investigates how atomic nuclei behave when placed in a static magnetic field (B_0) and can be perturbed by radiofrequency pulses. After this perturbation, the spin system will relax back to equilibrium over time. This can be detected and converted into a spectrum that yields unique information on the structure and dynamics of a particular molecular system. Aspects of the resulting spectrum from the perturbed nuclear spins including the linewidth, position, intensity and shape of the peaks can be analyzed to paint an intricate picture of the various chemical environments and physical changes that occur at the molecular level. Using this molecular level information continually improves our understanding of how small, local changes can impact the overall system and has guided advancements in a range of scientific disciplines.

This chapter provides background on NMR spectroscopy and the interactions that will dominate the 1D spectrum of a quadrupolar nucleus like ^{17}O. It will continue by outlining the nuances of the NMR experiments used herein. The chapter concludes with a brief section on the essential role of different software and the quantum chemical computations that are used to extract or predict NMR parameters.

2.1 NMR Basics for Quadrupolar Nuclei

NMR spectroscopy is one of the most robust analytical tools available that allows for the study of almost all elements across the periodic table. For an element to be studied via NMR spectroscopy, it must have an isotope with a non-zero spin quantum number (I). Nuclear spin is an intrinsic property imparted on atoms by the subatomic particles that compose the nucleus. The nucleus is comprised of particles called protons and neutrons. Each element is defined by its atomic number (Z), which is simply the number of protons found in its nucleus. However, the atomic mass of an element is the sum of the protons and neutrons and the number of neutrons can vary. This variation in the number of neutrons for a given element results in different isotopes. Therefore each isotope will have a unique I. The value of I for a given nucleus can be evaluated from the

mass number of an isotope.[92] If the number of protons and neutrons comprising the nucleus are both even, the isotope will have $I = 0$. If the number of protons and neutrons are both odd, resulting in a total mass number that is even, the isotope will have a non-zero, integer value for I (^{2}H, ^{14}N). When the total mass number is odd, I will be a half-integer number. For example, oxygen has three stable isotopes (^{16}O, ^{17}O and ^{18}O), with each nucleus containing 8 protons. Oxygen-16 has the highest natural abundance (99.75%) and it contains an even number of protons and neutrons resulting in $I = 0$, which is also the case for oxygen-18. Oxygen-17 however has 9 neutrons yielding an odd mass number and will therefore have a half-integer spin quantum number ($I = 5/2$) .

When $I > 0$, the nucleus is deemed NMR active as it has a magnetic moment, μ. The magnetic moment arises due to I interacting with another inherent nuclear property known as the magnetogyric ratio, γ and the reduced Planck's constant, $\hbar$.

$$\mu = \gamma \hbar I \tag{2.1}$$

Outside of a static magnetic field, each nuclear spin is randomly orientated and occupies spin states that have the same energy (Fig. 2.1a). However, when an NMR-active nucleus is placed into an external magnetic field, B_0, some of the nuclear spins will align themselves with B_0 (arbitrarily defined along the z-axis) to create a bulk magnetization that will start to precess about the z-axis with a distinctive frequency known as the Larmor frequency, ν_L. This frequency is typically on the order of MHz, which corresponds to the radiofrequency range of the electromagnetic spectrum and is unique to each NMR-active nucleus.

$$\nu_L = \gamma B_o / 2\pi \tag{2.2}$$

In addition to the nuclei precessing about B_0 when subjected to an external magnetic field, the degeneracy of the energy levels is also broken. These energy levels are now denoted by their magnetic spin quantum numbers, m_I. The number of spin states a nucleus can be found in depends on I and follows the $2I + 1$ rule. For the simplest case, where I =1/2, there will be two different energy levels that can be occupied with m_I of -½ or ½. When subjected to a sufficiently strong B_0 and in the absence of other interactions, each state will be equally spaced by the transition energy, ΔE.

$$\Delta E = \hbar \nu_L = \gamma \hbar B_o \tag{2.3}$$

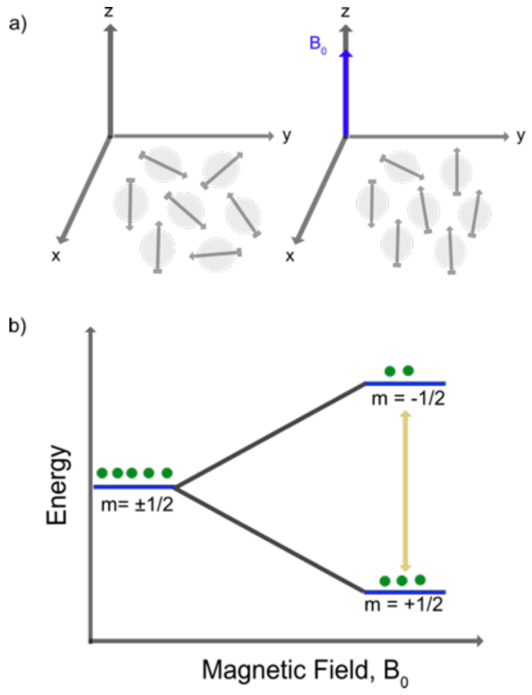

Figure 2.1 Depiction of nuclear spins in the absence and presence of an external magnetic field, B_0 (a) and the corresponding effect of B_0 on the energy levels for a spin ½ nucleus (b). Nuclear spins are randomly oriented in the absence of B_0 (a, left panel) but in the presence of B_0, some of the nuclear spins will align in the direction of the magnetic field to generate a net magnetization along the z-axis (a, right panel). When no B_0 is present, the two energy levels for I = ½ are degenerate and all nuclear spins have the same energy. When subjected to a B_0, these energy levels no longer are degenerate and a small population difference is created. The energy difference between spin states scales linearly with B_0 and is dependent on the nucleus being investigated (b).

This splitting of spin states in a magnetic field is known as the Zeeman effect and scales linearly with the magnetic field (Fig. 2.1b). The splitting of energy levels also drives a population distribution of the nuclear spins between each state and will result in lower energy states having a slightly larger population. At equilibrium, this population difference is described by the Boltzmann's distribution:

$$\frac{N_{-1/2}}{N_{1/2}} = exp\left(\frac{-\Delta E}{k_B T}\right) \tag{2.4}$$

In equation 2.4, k_B is the Boltzmann constant and T is the temperature in Kelvin. Provided the value of $k_B T$ is much larger compared to the numerator in this equation under conventional NMR experimental conditions, the population of each magnetic spin state is approximately the same ($N_{1/2} \cong N_{-1/2}$). This is known as the high-temperature approximation[93] and yields a new equation expressing the population difference between energy levels, ΔN, as:

$$\Delta N = \frac{(N\Delta E)}{(2k_B T)} \tag{2.5}$$

Here, N describes the total number of spins in the NMR sample and the population difference (ΔN) can be increased by going to lower temperatures, as utilized with DNP [56,94] or by using a larger B_0. The population difference is also impacted by what nucleus is being investigated as the value of the γ changes. Modifications to either the temperature or B_0 will translate into gains or losses in sensitivity which impacts NMR experimental time.

The premise of NMR spectroscopy is to disrupt this equilibrium population difference with a radiofrequency pulse that has the same frequency as ν_L to perturb the spins. Once the sample is no longer being irradiated, the spin system will relax to its equilibrium state. The relaxation process of nuclei over time follows an exponential decay and is termed a free induction decay (FID). This FID is detected and is translated into the frequency domain using a Fourier Transform which generates a spectrum (Fig. 2.2).[95]

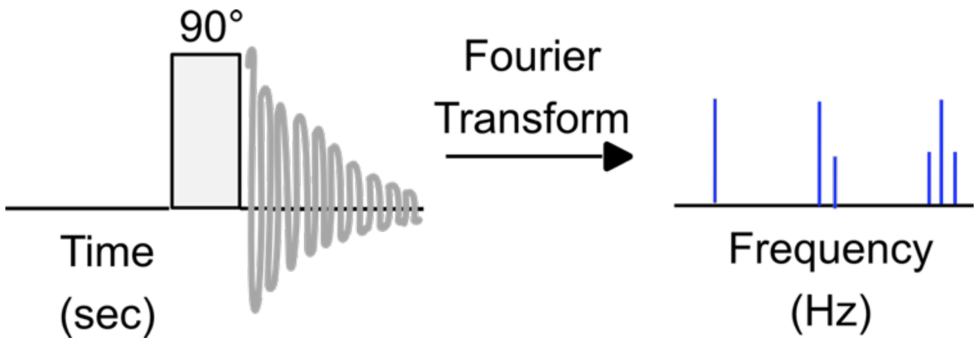

Figure 2.2. Schematic of a Bloch pulse used for acquiring a 1D NMR spectrum. A calibrated 90º radiofrequency pulse is used to place the bulk magnetization generated from the precession of nuclear spins in B_0 into the x-y plane. The acquisition of the FID occurs over a given time and records the relaxation of the system back to equilibrium and is Fourier transformed to yield a spectrum in the frequency domain.

2.2 Anisotropic Nuclear Spin Interactions

Many factors can impact the appearance of the signals observed in an NMR spectrum. In addition to the initial Zeeman splitting of the energy levels when placed in a magnetic field, other, usually smaller, interactions between nuclei and the surrounding electronic environment can perturb the energy of the spin states. To gauge these additional changes on a spin system, average Hamiltonian theory is employed.[96–98] The total Hamiltonian, $\mathcal{H}$, needs to be considered and is described by the sum of each individual nuclear spin interaction:

$$\mathcal{H} = \mathcal{H}_Z + \mathcal{H}_Q + \mathcal{H}_{CS} + \mathcal{H}_D + \mathcal{H}_J \tag{2.6}$$

The individual spin interactions are the Zeeman interaction ($\mathcal{H}_Z$), the quadrupolar interaction ($\mathcal{H}_Q$), the chemical shielding interaction ($\mathcal{H}_{CS}$), the dipole interaction ($\mathcal{H}_D$) and J-coupling ($\mathcal{H}_J$). For quadrupolar nuclei ($I > ½$), $\mathcal{H}_Q$ becomes increasingly important and is often the dominant interaction following $\mathcal{H}_Z$. In solid-state NMR, $\mathcal{H}_{CS}$ impacts the non-spinning spectrum for all nuclei but can be attenuated with magic-angle spinning. Acquiring ssNMR spectra under MAS conditions essentially mimics the isotropic molecular tumbling that is characteristic for solution NMR and has allowed for high-resolution NMR spectra to be collected for solids.[99–101] The $\mathcal{H}_D$ can be impacted by both homonuclear and heteronuclear spin coupling through space and largely depends on the spatial proximity and γ of the nuclear spins being considered.[98] This interaction can also be attenuated in solids using either MAS, decoupling techniques or a combination of

both.[102–104] However, dipolar recoupling experiments have been developed to selectively reintroduce these interactions to extract out important structural information.[105–107] Finally, $\mathcal{H}_J$ are through bond interactions between spins and are typically on the order of Hz. For solid-state NMR spectroscopy of quadrupolar nuclei, the J-coupling contributes a negligible amount to the overall signal breadth and is usually disregarded.

Given the work in this thesis focuses exclusively on the 1D acquisition of ssNMR spectra for molecules enriched with a quadrupolar nucleus, $\mathcal{H}_D$ and $\mathcal{H}_J$ will not be discussed further. However, experiments measuring these smaller interactions for ^{17}O have been explored elsewhere.[46,49,58,64,71,85–87,108] Both of these interactions have been measured for the COH site of Fmoc-alanine and are on the order of 13.5 kHz and 58 Hz, respectively.[49] This provides an idea of the magnitude for these two interactions in this subset of molecules and demonstrates why the duration of this section will focus on the dominant $\mathcal{H}_{CS}$ and $\mathcal{H}_Q$ interactions which measure in the 10's of kHz to MHz range.

2.2.1 Chemical Shielding Interaction

In the above section, which provided an initial introduction into how a NMR spectrum is obtained, it could be interpreted that all the same nuclei in a sample would appear at the exact same position (eqn. 2.2). This would be rather uninformative and thankfully is not the case. Each NMR-active nucleus is extremely sensitive to its electronic surroundings. The movement of electrons near a nucleus can create its own small, localized magnetic field, B', which influences the total magnetization perturbing the nucleus resulting in a new effective magnetic field, B_{eff}:

$$\begin{aligned} B' &= \sigma B_0 \\ B_{eff} &= B_0 - B' \\ B_{eff} &= (1-\sigma)B_0 \end{aligned} \tag{2.6}$$

Here, σ is the magnetic shielding term and B_{eff} can be substituted into equation 2.2 to obtain the new transition frequency, ν, for a given site.

$$\nu = (1-\sigma)\left[\frac{B_0\gamma}{2\pi}\right] \tag{2.7}$$

Since the electron environment at any given nucleus is quite distinctive, the new transition frequencies and thus peak positions provide a means of characterizing the different chemical environments in the sample.[109]

In practice, the magnetic shielding values are converted to chemical shifts, δ, using an absolute chemical shielding value, σ_{abs} , from a reference sample:

$$\delta_{sample} = \sigma_{abs} - \sigma_{sample} \tag{2.8}$$

The terms shielded and deshielded thus correspond to a decrease and increase in chemical shift, respectively.

Also, an NMR spectrum is typically plotted in arbitrary units of parts per million (ppm), as the frequencies of the peaks will be influenced by B_0, requiring all samples to be referenced against an internal or external standard with a known chemical shift:[110]

$$\delta_{sample} = \left[\frac{\nu_{sample} - \nu_{ref}}{\nu_{ref}}\right] \cdot 10^6 \tag{2.9}$$

The $\mathcal{H}_{CS}$ considers the local electron density of the spin system and its effect on a given nucleus and is defined below:

$$\mathcal{H}_{CS} = \gamma_I h I \cdot \sigma \cdot B_0 \tag{2.10}$$

Using the above equation as a guide, it can be seen that this interaction will scale linearly with the applied magnetic field and as such, acquiring NMR spectra at lower magnetic fields can be beneficial when working with a nucleus that has a large chemical shielding interaction like ^{19}F.[24]

The movement of electrons and their interaction with atoms in a magnetic field occurs in 3-dimensional space and a 3×3 matrix can be used to describe σ around a nucleus.

$$\sigma = \begin{bmatrix} \sigma_{11} & \sigma_{12} & \sigma_{13} \\ \sigma_{21} & \sigma_{22} & \sigma_{23} \\ \sigma_{31} & \sigma_{32} & \sigma_{33} \end{bmatrix} \tag{2.11}$$

This matrix can be diagonalized if we work in the principal axis system (PAS) and the chemical shielding tensor can then be characterized by three individual components, $\sigma_{11} \leq \sigma_{22} \leq \sigma_{33}$:

$$\sigma = \begin{bmatrix} \sigma_{11} & 0 & 0 \\ 0 & \sigma_{22} & 0 \\ 0 & 0 & \sigma_{33} \end{bmatrix}^{PAS} \quad (2.12)$$

Provided there is a known conversion between σ and δ (eqn. 2.8), this matrix can be rewritten in terms of the chemical shift:

$$\delta = \begin{bmatrix} \delta_{11} & 0 & 0 \\ 0 & \delta_{22} & 0 \\ 0 & 0 & \delta_{33} \end{bmatrix}^{PAS} \quad (2.13)$$

The three principal components of the chemical shift (CS) tensor are ordered as $\delta_{11} \geq \delta_{22} \geq \delta_{33}$ and from the average of these eigenvalues, the isotropic chemical shift (δ_{iso}) can be determined.

$$\delta_{iso} = \frac{(\delta_{11} + \delta_{22} + \delta_{33})}{3} \quad (2.14)$$

In the absence of other interactions, these eigenvalues can also be useful in describing the overall breadth (span, Ω) and the shape (skew, κ) of the anisotropic interaction observed in a non-spinning NMR spectrum. Using the Herzfeld-Berger convention,[111,112] the Ω and κ are defined as follows:

$$\Omega = \delta_{11} - \delta_{33} \quad (2.15)$$

$$\kappa = \frac{3(\delta_{22} - \delta_{iso})}{\Omega} \quad (2.16)$$

2.2.2 Quadrupolar Interaction

The quadrupolar interaction is present in nuclei that have $I > ½$, which covers the majority of NMR-active isotopes in the periodic table. These nuclei have a non-spherical distribution of the positively charged particles composing their nucleus (Fig. 2.3).[113] The quadrupolar interaction results when the electric quadrupole moment (Q), an intrinsic property of the nucleus, interacts with the electric field gradient (EFG). The EFG is created by the atoms in the surrounding environment of the quadrupolar nucleus and results in changes to the Zeeman energy levels. Like the CS tensor, the EFG tensor can be described using a 3×3 matrix which can be diagonalized by considering it in the PAS.

$$V = \begin{bmatrix} V_{xx} & 0 & 0 \\ 0 & V_{yy} & 0 \\ 0 & 0 & V_{zz} \end{bmatrix}^{PAS} \quad (2.17)$$

Unlike the CS tensor, the EFG tensor is a traceless second rank tensor with eigenvalues, V_{ii}. The individual tensor components are distinguished by their magnitude such that $|V_{zz}| \geq |V_{yy}| \geq |V_{xx}|$. The largest tensor component, V_{zz}, contributes to the quadrupole coupling constant, C_Q, which describes the magnitude of this interaction.

$$C_Q = -2.3496Q(fm^2)q_{zz}(a.u.) = \frac{eV_{zz}Q}{h} \quad (2.18)$$

C_Q is reported in frequency units and can be determined using either equivalent equation in 2.18. In the first case, the -2.3496 is a conversion factor that is used to convert between V_{zz} (MHz) and q_{zz} which is the largest EFG tensor component but expressed in atomic units (a.u.)[37] For ^{17}O, Q is equal to –2.558 fm^2 and for most biologically relevant molecules, the C_Q measured for ^{17}O sites typically falls between 6-9 MHz.[71,114]

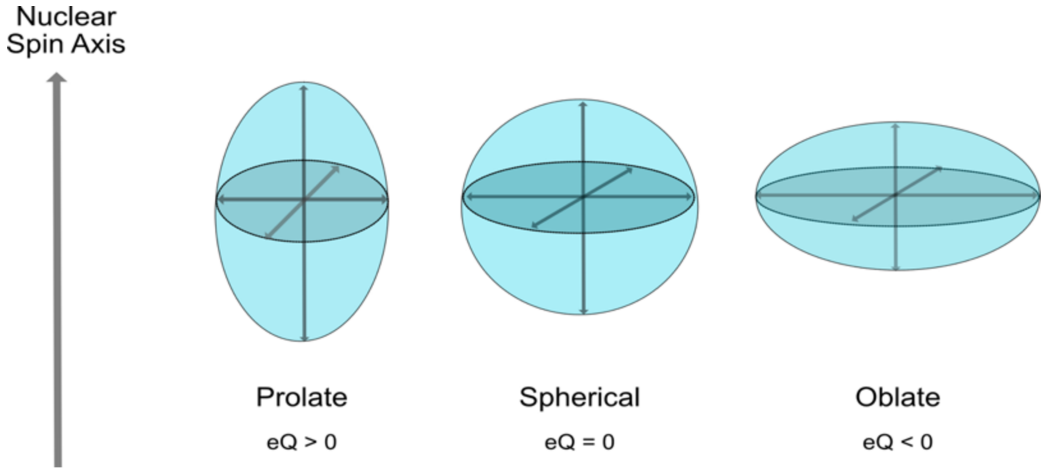

Figure 2.3. Deviation of the nuclear charge distribution.[113] A spherical charge distribution is present for spin-½ nuclei as they do not have an intrinsic quadrupolar moment ($Q = 0$). The non-spherical distortion of the nuclear charge can adopt either a prolate or oblate geometry which interacts with the EFG and results in an non-zero C_Q.

The EFG tensor components are also important in defining the asymmetry parameter, η. The η describes the shape of the quadrupolar interaction and can be determined using the following equation:

$$\eta = \frac{(V_{xx} - V_{yy})}{V_{zz}} \quad (2.19)$$

The $\mathcal{H}_Q$ is usually described by two terms, the first-order quadrupolar interaction, $\mathcal{H}_Q^{(1)}$, and the second-order quadrupolar interaction, $\mathcal{H}_Q^{(2)}$.[115] Both of these interactions will cause additional perturbations to the splitting of the spin quantum levels in a magnetic field (Fig. 2.4). For a nucleus with $I = 5/2$, there will be six different spin states. Unlike for a nucleus with a $I = ½$, when a quadrupolar nucleus with a half-integer I is outside of an B_0 (Fig. 2.4a, red circle), the spin states are not all degenerate with one another. Rather, each pair of spin states ($m_I \pm 1/2$, 3/2 and 5/2) will have the same energy and $m_I \pm ½$ will have the lowest energy.[116] The difference between the subsequent states is given by the quadrupolar frequency, ν_Q and $2\nu_Q$, in Hz (Fig. 2.4b).

$$\nu_Q = \frac{3C_Q}{2I(2I-1)} \tag{2.20}$$

The value of ν_Q can be reliably determined using nuclear quadrupole resonance (NQR)[117] but typical NMR experiments are performed in the regime where $B_0 >> 0$ and the Zeeman effect is the dominant interaction. Initially if other interactions are neglected, $\mathcal{H}_Z$ will contribute to the largest energy splitting of the spin states in a quadrupolar nucleus and will scale with B_0 in much the same way as it does for a spin-1/2 nucleus (Fig 2.4a). When $\mathcal{H}_Q^{(1)}$ is considered, the largest impact will be on the energy differences between the satellite transitions (ST) (Fig. 2.4c, purple). The difference between the -½ ↔ ½ (Fig. 2.4, yellow) is not perturbed by $\mathcal{H}_Q^{(1)}$ and will still have a transition frequency corresponding to ν_L. The transition between -½ ↔ ½ is known as the central transition (CT).

Fortunately, the $\mathcal{H}_Q^{(1)}$ only impacts the ST which are typically not observed in the NMR spectrum and in principle, could be averaged using fast MAS.[115] However, $\mathcal{H}_Q^{(2)}$, which does impact the CT (Fig 2.4c), can not be averaged out with MAS and will manifest in a broadening of the CT.[118,119] This broadening is known as the second-order quadrupolar broadening and scales inversely with B_0.[115,116]

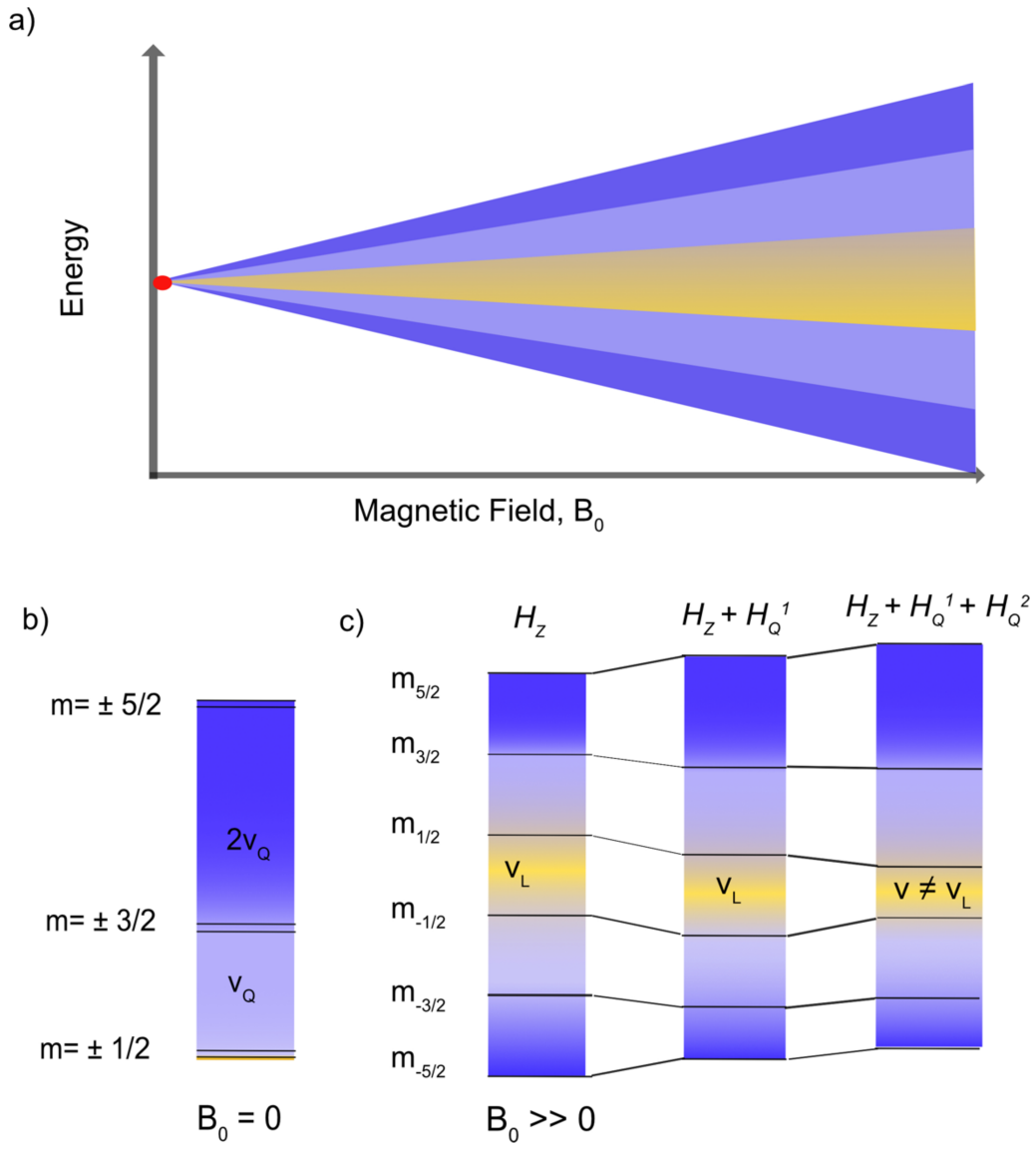

Figure 2.4. Energy splitting diagram for an I = 5/2 nucleus and the respective perturbations due to $\mathcal{H}_Q^{(1)}$ and $\mathcal{H}_Q^{(2)}$ on the Zeeman splitting of the central transition (½ ↔ -½, yellow) and satellite transitions (purple). When $B_0 = 0$ (red circle), only the pairs of spin states will be degenerate in energy (b). When $B_0 > 0$, the Zeeman interaction, $\mathcal{H}_Z$, usually dominates and cause each spin state to be spaced by the Larmor frequency, ν_L. $\mathcal{H}_Q^{(1)}$ will impact the transition frequencies of the satellite transitions (purple) but will not change the central transition. Incorporating the effects of $\mathcal{H}_Q^{(2)}$ on the energy splitting diagram, the central transition is now impacted and will no longer be spaced by ν_L (c).

2.3 NMR Experiments for Quadrupolar Nuclei

2.3.1 Traditional Solid-State NMR Techniques

Often when performing a ssNMR study, the ability to resolve multiple sites becomes challenging. This is even more pronounced when trying to observe multiple sites for a quadrupolar nucleus. However, dramatic improvements in the resolution of ^{17}O ssNMR spectra have been obtained by utilizing MAS and/or higher magnetic fields.[38,39,49] MAS was first introduced to ssNMR spectroscopy in the late 1950's and is a technique that helps mitigate some of the anisotropic interactions that broaden the peaks in an NMR spectrum of a solid.[99,100,120,121] MAS works by rotating a solid sample at a fixed angle of 54.74º with respect to B_0. This rapid rotation allows for all the anisotropic interactions containing the spatial term, $3\cos^2\theta - 1$, to be either partially or completely attenuated. This technique essentially mimics the molecular tumbling that occurs in solutions and will result in peaks that are more isotropic in nature. For MAS to yield an isotropic peak, the rate of rotation must be greater than that of the largest anisotropic interaction at that site. When lower spinning rates are used, the interactions manifest into a series of peaks known as spinning side-bands. The position of the spinning sidebands are frequency dependent which can help to distinguish the isotropic peak from the sidebands. To date, spinning frequencies up to 110 kHz can be routinely achieved.[122,123]

For quadrupolar nuclei like ^{17}O, the $\mathcal{H}_Q{}^{(1)}$ can be attenuated with MAS but the CT will still have SOQB as the $\mathcal{H}_Q{}^{(2)}$ term contains more than one spatial dependence term, hence will only be partially (~2/3rd) reduced.[118,119] Fortunately, $\mathcal{H}_Q{}^{(2)}$can be reduced by going to higher B_0 (>18 T) and has allowed for higher resolution ^{17}O NMR spectra to be obtained.[69–71] Over the past decade, this has become more feasible for users through the development and commercialization of ultrahigh field superconducting NMR magnets with magnetic field strengths of 1.0 to 1.5 GHz but comes with a substantial price tag. However, at higher B_0, the CSA interaction becomes more prevalent which necessitates the use of higher MAS frequencies to resolve multiple sites from the spinning side-band manifold. Thus, balancing the benefits of both fast MAS and higher B_0 requires careful consideration by the user to understand their equipment's limitations as well as the interactions at play within a given sample.

In addition to balancing the benefits of fast MAS and ultrahigh field spectrometers, an appropriate NMR pulse sequence must also be selected. One of the simplest experiments performed in NMR spectroscopy is the Hahn-echo experiment. This experiment was developed in 1950 by Erwin Hahn [124] and is characterized by using a $\frac{\pi}{2}$ pulse to place the magnetization in the transverse plane. The magnetization will dephase over the first time delay, t_1, due to the relaxation mechanisms present in the spin system. After the initial delay, a subsequent π pulse is used to refocus the magnetization and the FID is acquired after a second delay with time, t_2. Figure 2.5 shows a typical schematic of the echo pulse sequence ($90_x°$-τ-$180_y°$-τ) and depicts the effect of the radio-frequency pulses and time delays on the bulk magnetization generated by the nuclei when in B_0 (Fig. 2.5 a-e).

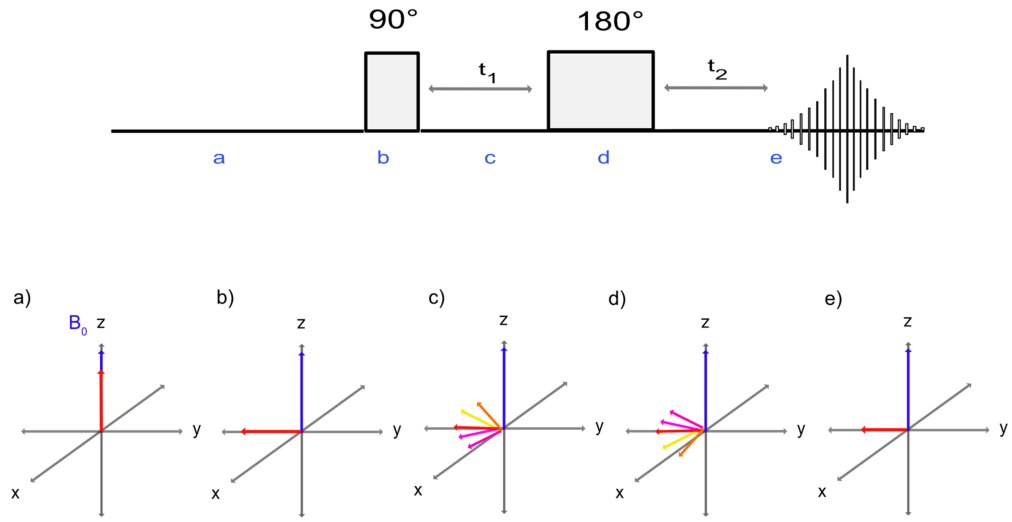

Figure 2.5. Schematic of a Hahn-echo pulse sequence and the impacts of the sequence on the bulk magnetization (red arrow) created by placing NMR active nuclei in B_0 (blue arrow).[124] After being placed in B_0 for a sufficiently long time, the bulk magnetization will be aligned along the z-axis (a). After the system has reached this equilibrium state, a $\frac{\pi}{2}$ pulse is used to place the magnetization into the transverse plane (b) which start to dephase over the first time delay, t_1 (c). A π is then used to flip the dephased magnetization (d) and the magnetization will now refocus along the -y axis over the second time delay, t_2 (e). This allows for the acquisition of an echo and this pulse sequence can be repeated once the system has relaxed back to equilibrium (a).

For quadrupolar nuclei, the echo sequence is sometimes modified to incorporate a second $\frac{\pi}{2}$ pulse in place of the π pulse. This modified sequence ($90_x°$-τ-$90_y°$-τ) is known as a solid or quadrupolar echo and is used to ensure broader excitation and to reduce any distortions in the line shape of the peaks.[125]

Each of these NMR experiments can be acquired with or without MAS to extract out the relevant NMR parameters for the central transition of quadrupolar nuclei. Under MAS conditions, C_Q, η and δ_{iso} can be identified for each site by performing either echo experiment at multiple magnetic field strengths. When investigating an amorphous sample under non-spinning conditions, all anisotropic interactions for each distinct site will be present, resulting in a very broad and complex spectrum.[118] It is important to note that both the MAS and non-spinning experiments are acquired with ^{1}H decoupling to effectively remove the heteronuclear dipolar and scalar couplings from the powdered sample.[102] This leaves the CSA and quadrupolar interactions intact in the non-spinning sample, but with the help of the MAS spectra to refine the EFG parameters and δ_{iso}, the remaining CSA parameters, Ω and κ, along with the Euler angles, can be determined for each unique site, in most cases.[118]

2.4 Quantum Chemical Calculations and Simulations of NMR Parameters

2.4.1 Simulation of Quadrupolar NMR Spectra

Extracting the relevant NMR parameters from an experimental ssNMR spectrum requires the assistance of simulation software. WSolids1 is one such computer program that allows the users to determine NMR interactions from 1D NMR spectra using an iterative process.[126] This Windows® program was written in C++ and uses the Multiple Document Interface specification to operate multiple screens. This program is versatile enough to analyze data acquired on either a Bruker or Agilent spectrometer and can interconvert between the different conventions used to describe the CSA tensors. This program was developed by Dr. Klaus Eichele while at Dalhousie University.

2.4.2 Computation of NMR Parameters

To determine relevant information about NMR parameters that cannot be obtained experimentally (in most cases), such as the sign of C_Q, or to predict NMR parameters prior to costly isotopic enrichment protocols, quantum chemical calculations can be employed. One such

method for performing these types of calculations is based on density functional theory (DFT).[127] DFT methods can be used to calculate the CSA and EFG tensor components[128–130] through the Amsterdam Density Functional (ADF) package.[131–133] The ADF program uses basis sets that are based on Slater-type orbitals as they can describe the nucleus of different atoms in a molecule quite reliably. The calculations undertaken in this work for determining the ^{17}O NMR parameters in Fmoc-amino acids used the Vosko-Wilk-Nusiar (VWN) local density approximation[134] with Becke-Perdew generalized gradient approximation (GGA)[135–137] for the exchange-correlation functional. Zeroth order regular approximation (ZORA) type basis sets were typically adopted for these calculations as they include both scalar and spin-orbital relativistic effects[138] which are suitable for calculating NMR parameters.

2.4.3 Visualizing Euler Angles

Euler angles define the relative orientations of two orthogonal coordinate systems that have the same origin. In the case of this work, the Euler angles are used to describe the orientation of the EFG and CSA tensors in their PASs with respect to one another (Fig. 2.6). The program EFGshield uses information from the quantum chemical calculations performed to determine the x,y,z coordinates for the individual EFG and CSA tensor components so the user can easily visualize these components within the molecular framework centred about the selected nucleus.[139] EFGshield's graphic user interface also summarizes the relevant NMR parameters and Euler angles for the selected atom and appends a list of all the analogous Euler angles between the PAS to a modified output file.[139] This open-source program was created in Prof. David Bryce's laboratory at the University of Ottawa and is written in C and runs on Windows operating systems.[139] It has the utility to use information generated within the output files from a variety of computational programs that are typically used to calculate NMR parameters, including the ADF program. Figure 2.6 depicts the Euler angles, α, β and γ, that were determined by EFGshield for the ^{17}O nucleus of the C=O site on Fmoc-L-isoleucine. The origin of this system is the ^{17}O nucleus and the EFG PAS is used as the reference axis system in this figure. All rotations of the CSA PAS are counterclockwise and follow the right hand rule. The relative orientation of the tensors to each other can impact the line shape that is observed in the non-spinning NMR spectra and as such the Euler angles determined from the computed NMR parameters can be a useful guide when simulating the experimental spectra in programs like WSolids1.

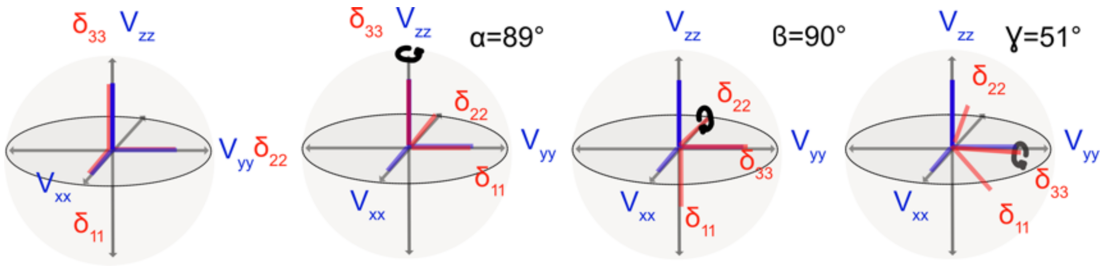

Figure 2.6. Relative orientation of the EFG and CSA tensor components computed for the carbonyl oxygen in Fmoc-L-isoleucine using EFGshield.[139] Initially the tensor components are coincident with each other. The above is a depiction of what occurs when the PAS of the CSA tensor is rotated away from the EFG PAS. The first counterclockwise rotation which is about the δ_{33} component is described by the angle α. Next, a rotation about the newly orientated δ_{22} component by angle, β= 90° places the δ_{33} component nearly parallel to the V_{yy} tensor. A third counterclockwise rotation about the δ_{33} component by γ = 51° leads to the final orientation of tensor components characterized by the Euler angles, α, β and γ.

Chapter 3: Solid-State NMR Spectroscopy and Quantum Calculations of ^{17}O-enriched Fmoc-Amino Acids

Overview

Protected- amino acids are an important subset of biomolecules as they can be directly used to construct peptides via solid-state peptide synthesis. Enriching these molecules with ^{17}O is an advantageous pathway to obtaining peptides that can be tailored in length, composition and number of ^{17}O nuclei. This chapter will detail the protocol used to isotopically enrich a selection of Fmoc-protected amino acids with ^{17}O, specify the relevant experimental parameters used to acquire ^{17}O ssNMR spectra as well as describe the methodology used for undertaking quantum chemical calculations on a single molecule. The remainder of the chapter will discuss the results obtained from the ^{17}O NMR experiments and DFT calculations and the conclusions that can be drawn. Together, this work provides previously unreported ^{17}O NMR parameters for five protected amino acids, doubling the available ^{17}O NMR data for this class of biologically relevant molecules which sets a stronger precedence for their use in future studies.

3.1 Methods

3.1.1 ^{17}O Enrichment of Fmoc-Amino Acids

All reagents were sourced commercially and used without further purification. Oxygen-17 isotopic enrichments of the Fmoc-protected amino acids were performed following the multiple-turnover reaction described previously.[45,46] Approximately 200 mg of the Fmoc-amino acid were dissolved in dimethylformide and purged under N_2 (g). Twenty equivalents (w/w) of pyridine hydrobromide were added to the stirring solution as a dry proton source to activate the carbodiimide and prevent racemization of the O-acylisourea intermediate.[45] Thirty-five equivalents (w/w) of 39.3% $H_2{}^{17}O$ (CortecNET) were added to the stirring solution followed by 10 equivalents of 1-(3-dimethylaminopropyl)-3-ethylcarboiimide hydrochloride (EDC•HCl). The reaction was stirred for 2 hrs at room temperature and another 10 equivalents of EDC•HCl were added. The addition of EDC•HCl was repeated to obtain a total of 30 equivalents in solution, which was allowed to stir overnight.

The reaction mixture was diluted with ~25 mL of ethyl acetate and dried over $MgSO_4$. The solution was filtered, and the organic layer was isolated via a liquid-liquid extraction with 3 × 10

mL portions of each 0.1 M citric acid and 0.1 M citric acid in brine solution. The organic solvents were removed using a rotary evaporator. A yellow oil product was obtained. Fmoc-L-tyrosine, Fmoc-L-tryptophan and Fmoc-L-isoleucine were recrystallized with a DCM/H_2O/ether or acetonitrile/H_2O mixture. High-performance-liquid-chromatography (HPLC) was used to isolate Fmoc-L-proline and Fmoc-L-threonine and powdered products were obtained via lyophilization. The purity and % ^{17}O enrichment for each Fmoc-protected ^{17}O-labelled amino acid was assessed using mass spectrometry (MS).

3.1.2 Solid-State NMR Spectroscopy

The ^{17}O ssNMR spectra were acquired at 14.1 and 21.1 T, which corresponds to ^{17}O Larmor frequencies of 81.38 and 122.02 MHz, respectively. Spectra were referenced relative to the ^{17}O peak of liquid H_2O at 0 ppm. NMR experiments were performed at 21.1 T using a Bruker Avance II spectrometer, equipped with a 3.2 mm H/X MAS Bruker probe, at the National Ultrahigh-field NMR Facility for Solids (Ottawa, Canada). NMR experiments at 14.1 T were performed on a Bruker wide-bore 600 Ascend DNP NMR spectrometer using a triple resonance 3.2 mm Bruker MAS probe. The sample quality was also monitored using ^{13}C cross-polarization (CP)-MAS[140] and ^{1}H MAS experiments. One-dimensional ^{17}O MAS NMR spectra were acquired using a rotor synchronized Hahn-echo ($\pi/2$-τ- π -τ) pulse sequence and spinning frequencies of 22 (21.1 T) or 23.5 (14.1 T) kHz were used. Recycle delays were checked for each sample using a quadrupolar-CPMG experiment and set between 0.5-5 s. Pulse lengths (solution(^{17}O) $\gamma B_1/2\pi$ = 42-55 kHz) were set between 1.5-2 ($\pi/2$) and 3-4 μs (π) depending on spectrometer. All MAS spectra were left-shifted by 40 points at 14.1 T and 18 points at 21.1 T. The number of scans collected for each spectrum ranged from 12,288 to 81,920 scans.

Non-spinning ^{17}O NMR spectra were acquired at 14.1 T using similar experimental conditions as described above, but the number of scans increased to 300 k and 100 kHz of TPPM ^{1}H decoupling[102] was used. Non-spinning ^{17}O NMR spectra at 21.1 T were collected using a homebuilt 5 mm H/X solenoid probe; samples were packed in 5 mm (o.d.) PTFE tubes to minimize the ^{17}O background signal. A modified quadrupolar echo ($\pi/2$-τ- $\pi/2$-τ) pulse sequence was used for broader excitation and to reduce any distortions in the line shape.[125] This experiment used $\pi/2$ pulse lengths of 1.5 μs, recycle delays of 2-10 s, and continuous wave ^{1}H decoupling ($\gamma B_1/2\pi$ = 75 kHz) were used. Between 5,000 and 33,000 co-added transients were collected for each spectrum.

All spectra were processed in TopSpin (Bruker, Biospin Ltd.) using between 100 and 500 Hz of line broadening and non-spinning spectra were left shifted by 60 points at 14.1 T and 40 points at 21.1 T. Spectral simulations were performed using the WSolids1 NMR simulation package.[126]

3.1.3 Quantum Chemical Computations

Density functional theory was used to calculate NMR parameters and perform geometry optimizations for the Fmoc-amino acids using the Amsterdam Density Functional (ADF) 2017 modeling suite.[131–133] The crystal structures of Fmoc-L-isoleucine[141] and Fmoc-L-tyrosine, monohydrate[142] were used to evaluate the convergence to identify the optimal basis set for computing NMR parameters and to explore how geometry optimizations prior to computing NMR parameters influenced the values (Tables 1 and 2). The geometry optimizations on a single molecule of each Fmoc-amino acid was performed implementing the zeroth order regular approximation (ZORA) method along with the double-zeta polarized (ZORA/DZP) basis set. After geometry optimizations were completed, the NMR parameters were calculated from these molecular models to include relativistic effects utilizing a triple-zeta with two-polarization functions basis (ZORA/TZ2P). The calculated NMR parameters for the Fmoc-amino acids studied are summarized in Table 3. All computations were performed using the BP86 functional[135,136] with the generalized gradient approximation.

Table 1. Selection of basis sets for computing NMR parameters using density functional theory on crystal structure of FMOC-L-tyrosine, monohydrate.

Basis set	^{17}O site	σ_{iso} (ppm)	σ_{33} (ppm)	σ_{22} (ppm)	σ_{11} (ppm)	C_Q (MHz)	η
DZP	CO	-41.571	281.028	-131.463	-274.278	7.88961	0.12270
	COH	155.200	256.063	177.473	32.065	-7.94763	0.37483
ZORA/DZP	CO	-39.327	281.867	-128.663	-271.184	7.89293	0.11949
	COH	156.896	243.562	179.435	33.372	-7.54985	0.37714
TZ2P	CO	-88.756	269.898	-188.846	-347.315	8.85450	0.13684
	COH	132.856	243.562	164.261	-9.255	-9.07486	0.36192
ZORA/TZ2P	CO	-86.815	270.438	-186.307	-344.576	8.85790	0.13550
	COH	134.330	245.223	166.099	-8.331	-9.07075	0.35039

QZ4P	CO	-96.012	269.361	-197.114	-360.283	8.91513	0.13757
	COH	125.903	237.160	155.206	-14.656	-9.24279	0.34899
ZORA/QZ4P	CO	-94.454	269.623	-194.977	-358.008	8.92528	0.13409
	COH	127.208	238.691	156.840	-13.907	-9.25906	0.36450

Table 2. Comparison of the computed ^{17}O NMR parameters[1] for Fmoc-L-tyrosine and -isoleucine obtained using their reported crystal structures with those obtained using different geometry-optimized structures.

Sample	Structure Coordinates	^{17}O site	σ_{iso} (ppm)	σ_{33} (ppm)	σ_{22} (ppm)	σ_{11} (ppm)	C_Q (MHz)	η
Fmoc-L-tyrosine	X-ray	CO	-86.815	270.438	-186.307	-344.576	8.85790	0.13550
		COH	134.330	245.223	166.099	-8.331	-9.07075	0.35039
	ZORA/DZP	CO	-93.091	269.163	-206.649	-341.787	8.68533	0.13762
		COH	108.232	241.788	136.433	-53.524	-8.64595	0.57711
	ZORA/TZ2P	CO	-93.091	260.277	-220.836	-318.558	8.85298	0.19300
		COH	112.222	243.997	142.508	-49.840	-8.70477	0.55091
	ZORA/QZ4P	CO	-84.404	264.308	-219.903	-297.617	8.66492	0.15265
		COH	108.858	233.659	148.15	-55.234	-8.69706	0.50636
Fmoc-L-isoleucine	X-ray	CO	-85.878	281.835	-190.302	-349.168	8.93670	0.1735
		COH	151.609	263.304	207.206	-15.684	-8.38861	0.3534
	ZORA/DZP	CO	-77.928	266.204	-212.547	-287.441	8.55007	0.12112
		COH	93.889	227.876	121.964	-68.172	-8.54004	0.53998
	ZORA/TZ2P	CO	-78.05	268.236	-215.276	-287.106	8.59598	0.13323
		COH	96.387	229.723	125.097	-65.660	-8.59363	0.50872
	ZORA/QZ4P	CO	-75.628	266.393	-211.022	-282.000	8.55424	0.12526
		COH	99.299	230.27	127.273	-59.645	-8.62249	0.49025

[1] All NMR parameters were computed using the ZORA/TZ2P basis set. The NMR parameters for the X-ray structure were obtained from a single molecule crystal structure and did not undergo geometry optimization.

Table 3. Density functional theory computed NMR parameters[2] on geometry-optimized structures.

Sample	^{17}O site	σ_{iso} (ppm)	σ_{33} (ppm)	σ_{22} (ppm)	σ_{11} (ppm)	C_Q (MHz)	η
Fmoc-L-tyrosine	CO	-93.091	269.163	-206.649	-341.787	8.68533	0.13762
	COH	108.232	241.788	136.433	-53.524	-8.64595	0.57711
Fmoc-L-proline	CO	-88.920	262.934	-214.866	-314.829	8.77591	0.14672
	COH	104.576	240.112	130.684	-57.068	-8.57213	0.56200
Fmoc-L-threonine	CO	-82.932	253.228	-228.309	-273.716	8.44669	0.10659
	COH	91.851	213.172	136.461	-74.080	-8.50001	0.55040
Fmoc-L-tryptophan	CO	-93.386	253.942	-213.848	-320.252	8.79774	0.14495
	COH	101.394	238.317	136.519	-70.654	-8.66472	0.56482
Fmoc-L-isoleucine	CO	-77.928	266.204	-212.547	-287.441	8.55007	0.12112
	COH	93.889	227.876	121.964	-68.172	-8.54004	0.53998

3.2 Results and Discussion

3.2.1 Percent Enrichment of Fmoc-Amino Acids

To overcome the low natural abundance of ^{17}O (0.037%), the five Fmoc-amino acids studied were enriched with 39.3% ^{17}O-labelled H_2O using the multiple-turnover labelling scheme described by Seyfried *et al*.[45] This reaction pathway allows for ^{17}O incorporation into the protected amino acids to proceed at room temperature under slightly acidic conditions. The purity and amount of ^{17}O incorporation into the Fmoc-amino acids were measured using HPLC-MS. The mass spectrum of Fmoc-L-isoleucine is shown in Fig. 3.1 (expected MW= 353.4 Da). The mass spectrum is consistent with what is expected for the isolated pure product and shows a series of peaks with m/z having an additional +23 Da, attributed to the presence of a Na^+ ion. The series of peaks observed have m/z of 376.3, 377.3, 378.2, 379.2, and 380.1 Da, which corresponds to M^+,

[2] NMR parameters were calculated using zero-order regular approximation; triple-zeta basis set (ZORA/TZ2P) after geometry optimization on each structure was implemented using the ZORA, double-zeta basis set (ZORA/DZP).

$(M+1)^+$, $(M+2)^+$, $(M+3)^+$, and $(M+4)^+$ respectively. The peak intensities were corrected for the expected ion distribution of the non-labelled Fmoc-L-isoleucine and the ion distribution expected for the addition of one and two ^{17}O sites. The ratio of the corrected peak intensities at 376.3, 377.3 and 378.2 Da were then used to determine the percent of ^{17}O enrichment. This process was extended to assess the purity and ^{17}O enrichment of the other Fmoc-amino acids and the % enrichment was found to be 40 ± 5% for Fmoc-L-isoleucine and was 35 ± 5% for the other amino acids. The labelling efficiency of the multiple-turnover reaction was in line with what was reported previously for the Fmoc-amino acids enriched using this method,[46] underscoring the effectiveness of this labelling approach.

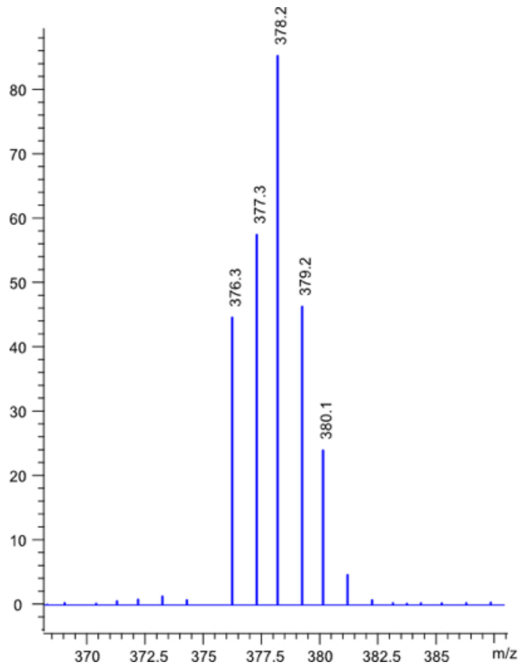

Figure 3.1. Mass spectrum of Fmoc-L-isoleucine after precipitation in acetonitrile and water. The expected MW for Fmoc-L-isoleucine is 353.41 Da and the $[M+H]^+$ series shown in the spectrum have an additional +23 Da due to the presence of Na^+. The α-COOH can have a mixture of contributions from $^{16}O/^{16}O$ at 376.3 m/z, $^{16}O/^{17}O$ or $^{17}O/^{16}O$ at 377.3 m/z, $^{17}O/^{17}O$ or $^{16}O/^{18}O$ or $^{18}O/^{16}O$ at 378.2 m/z, $^{18}O/^{17}O$ or $^{17}O/^{18}O$ at 379.2 and $^{18}O/^{18}O$ at 380.1 m/z

3.2.2 Experimental ^{17}O NMR Spectra

To further build upon the existing small biomolecule ^{17}O NMR database, a series of MAS and non-spinning ^{17}O ssNMR experiments were conducted for five Fmoc-amino acids (Figs. 3.2-3.5), all reported here for the first time. The line shapes of the central transition (CT) for each ^{17}O site in the NMR spectra were analyzed to determine the EFG and chemical shift tensor parameters as described above and are summarized in Table 4. Figure 3.2 shows the experimental and simulated MAS and non-spinning ^{17}O NMR spectra for Fmoc-L-isoleucine at 21.1 and 14.1 T. The carbonyl (C**O**) and hydroxyl (C**O**H) sites are clearly resolved from each other at both magnetic field strengths and have δ_{iso} of 330 ± 1 and 165 ± 1 ppm, respectively. However, the edges of the first spinning sidebands (*) overlap with the central transition peaks in the experimental spectrum acquired 21.1 T (Figure 3.2a, ν_{MAS} = 22 kHz). At 14.1 T, the MAS frequency was increased to 23.5 kHz and the spinning sidebands no longer interfere with the central transition peaks. This allows for a more accurate determination of the EFG tensor parameters for the Fmoc-amino acids at the lower magnetic field with moderate spinning frequencies, as the intensity and shape of the peaks are no longer perturbed. At the same time, the two peaks in the MAS spectra acquired at 14.1 T have linewidths that are ~ 2 times broader (in ppm) than those at 21.1 T (Figures. 3.2-3.5a). This shows how advantageous ultrahigh field NMR is at reducing the second-order quadrupolar broadening, as it scales inversely with magnetic field strength and can be utilized to obtain higher resolution ^{17}O NMR spectra.[38,39,69–71] However, as demonstrated above with the increase in magnetic field strength, faster MAS is advantageous to combat the overlapping spinning sidebands when multiple NMR sites are present. This emphasizes the dichotomy faced by users when going to higher magnetic fields; with greater magnetic field strength, faster MAS is needed to avoid the spinning sidebands overlapping with isotropic peaks which in turn requires smaller rotors. These smaller rotors hold less sample, a benefit in reducing the need for large volumes of labelled material, but also making it integral to have high and effective labelling to maximize sensitivity. A more detailed description of the impact magnetic field strength has on the MAS and stationary line shapes of quadrupolar nuclei and how it pertains to ^{17}O NMR of amino acids has been presented elsewhere.[69,118]

The EFG tensor parameters, C_Q and η, were determined for the carbonyl (C**O**) oxygen to be 8.5 ± 0.2 MHz and 0.02 ± 0.05, respectively, and 7.4 ± 0.2 MHz and 0.30 ± 0.05 for the hydroxyl (C**O**H) oxygen of Fmoc-L-isoleucine. The remaining chemical shift tensor parameters, Ω and κ,

were found from simulating the non-spinning spectra (Figure 3.2b). The span and skew correspond to 490 ± 75 ppm and 0.6 ± 0.25 for the C**O** site and 300 ± 75 ppm and -0.8 ± 0.25 for the C**O**H site. These ^{17}O NMR parameters are in agreement with the values reported for other Fmoc-amino acids.[34,46,143]

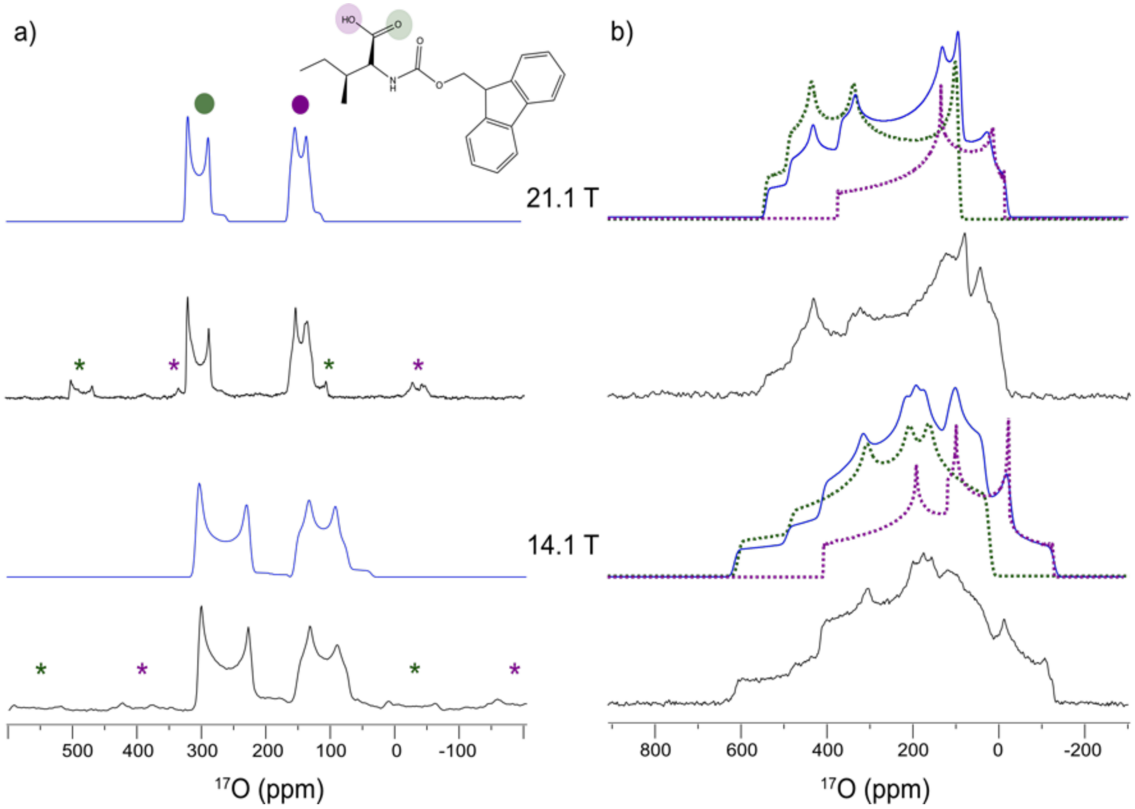

Figure 3.2. Experimental (black) and simulated (blue) oxygen-17 NMR spectra of 40% labelled Fmoc-L-isoleucine acquired at 21.1 and 14.1 T of MAS (a) and non-spinning (b) samples. The structure of Fmoc-L- isoleucine is shown above the MAS spectra and the peaks are assigned to the hydroxyl (purple) and carbonyl site (green) of the carboxylic acid moiety. The MAS NMR spectra were obtained using spinning frequencies of 22 or 23.5 kHz, respectively, and the spinning sidebands are indicated with asterisks. The simulations of the ^{17}O sites in the non-spinning spectra (b) are shown for the individual CO (green) and COH (purple) sites and overlaid with the entire simulated spectrum (blue). The MAS and stationary spectra were calculated with WSOLIDs and the NMR parameters are reported in Table 4.

Table 4. Experimental and Computed ^{17}O NMR Parameters of Fmoc-Amino Acids.

Sample	^{17}O site	δ_{iso} (ppm, ±1)	C_Q* (MHz, ±0.2)	η (±0.05)	Ω (±75)	κ (±0.25)	α (±20°)	β (±20°)	γ (±20°)
Fmoc-L-Isoleucine	Expt. CO	330	8.5	0.02	490	0.60	5	90	45
	DFT. CO	365	+8.6	0.12	554	0.73	89	90	51
	Expt. COH	165	7.4	0.30	300	-0.80	50	20	15
	DFT. COH	194	-8.5	0.54	296	-0.28	359	30	359
Fmoc-L-Tryptophan	Expt. CO	346	8.6	0.06	540	0.70	85	90	50
	DFT. CO	381	+8.8	0.14	574	0.63	89	89	302
	Expt. COH	167	7.5	0.25	240	-0.80	30	0.5	0
	DFT. COH	186	-8.7	0.56	309	-0.34	177	31	186
Fmoc-L-Proline	Expt. CO	346	8.6	0.15	510	0.65	80	90	45
	DFT. CO	376	+8.8	0.15	578	0.65	90	90	236
	Expt. COH	167	7.7	0.30	200	-0.95	10	20	15
	DFT. COH	183	-8.5	0.56	297	-0.26	356	31	2
Fmoc-L-Tyrosine**	Expt. CO	328	8.4	0.18	460	0.65	15	90	45
	DFT. CO	381	+8.7	0.14	610	0.56	88	90	302
	Expt. COH	176	7.4	0.22	210	-1.00	10	25	15
	DFT. COH	179	-8.6	0.58	295	-0.29	177	32	186
Fmoc-L-Threonine**	Expt. CO	311	8.1	0.05	530	0.48	30	90	20
	DFT. CO	370	+8.4	0.11	527	0.83	80	89	301
	Expt. COH	192	7.2	0.08	255	-0.75	40	65	70
	DFT. COH	196	-8.5	0.55	287	-0.47	172	30	4
Fmoc-L-Alanine[3]	Expt. CO	305	7.90	0.18	450	0.69	14	90	134
	DFT. CO	375	+8.6	0.13	547	0.74	90	90	123
	Expt. COH	180	7.05	0.15	218	-0.99	10	12	-16
	DFT. COH	188	-8.5	0.52	292	-0.41	180	32	1
Fmoc-L-Serine[3]	Expt. CO	337	8.35	0.04	521	0.49	0	90	128
	DFT. CO	381	+8.8	0.19	579	0.64	272	90	54
	Expt. COH	168	7.60	0.35	236	-0.97	8	-25	0
	DFT. COH	179	-8.6	0.58	300	-0.30	180	31	181
Fmoc-L-Leucine[4]	Expt. CO	338	8.3	0.00	385	0.10	30	90	0
	DFT. CO	381	+8.9	0.19	571	0.73	267	90	295
	Expt. COH	161	7.3	0.20	320	-0.80	20	65	70
	DFT. COH	187	-8.6	0.58	295	-0.17	358	32	356
Fmoc-L-Valine[4]	Expt. CO	337	8.5	0.00	340	0.20	45	90	0
	DFT. CO	376	+8.7	0.17	550	0.76	271	90	302
	Expt. COH	169	7.3	0.15	320	-0.7	20	65	70
	DFT. COH	195	-8.5	0.55	301	-0.18	178	30	179

* All experimental C_Q values are reported as absolute values whereas computed C_Q values have a determined + or - sign

**Only experimental data for non-spinning spectra acquired at 21.1 T were used for simulations; EFG parameters reported for Fmoc-L-threonine from the recrystalized sample; larger associated errors in CSA parameters (± 100, Ω; ± 0.5, κ) are indicated below.

[3]Experimental data from K.Yamada *et al.* (2008). The sidechain of Fmoc-L-Serine was protected with t-butyl in this study.

[4]Experimental data from Keeler *et al.* (2017); amended experimental spans for CO sites are 530 and 540 ppm for Fmoc-L- leucine and -valine, respectively.

Euler angles evaluated using EFGshield[139] based on DFT results

The ^{17}O NMR spectra for Fmoc-L-tryptophan are shown in Figure 3.3 and the chemical shift parameters were determined to be δ_{iso} = 346 ± 1 and 167 ± 1 ppm, Ω = 540 ± 75 and 240 ± 75 ppm, and κ = 0.7 ± 0.25 and -0.8 ± 0.25 for the C**O** and C**O**H sites, respectively. The C_Q's are 8.6 ± 0.2 and 7.5 ± 0.2 MHz and the η's are 0.06 ± 0.05 and 0.25 ± 0.05. The sharp peak at 0 ppm (Figure 3.3, red triangle) is attributed to the presence of residual water in the sample.[68,144] Analysis of the ^{17}O NMR spectra for Fmoc-L-proline (Figure 3.4) yielded the following NMR parameters for the C**O** and C**O**H groups: δ_{iso} = 346 ± 1 and 167 ± 1 ppm, Ω = 510 ± 75 and 200 ± 75 ppm, κ = 0.65 ± 0.25 and -0.90 ± 0.25, C_Q = 8.6 ± 0.2 and 7.7 ± 0.2 MHz and η = 0.15 ± 0.05 and 0.30 ± 0.05, respectively. In addition to minor spinning sidebands (*) overlapping with the central transition in the MAS NMR spectrum obtained at 21.1 T (Figure 3.4a), a broad peak centred between the C**O** and C**O**H peak is evident (yellow circle). At 14.1 T, this broad peak now interferes with the ability to clearly resolve the baseline of the two CT peaks. Since the HPLC-MS spectrum (data not shown) indicates no other contaminants are present, the most likely culprit is that there is a mixture of the carboxylate ion and carboxylic acid of the Fmoc-amino acid. The pKa of the α-COOH in unprotected amino acids is typically around 2, however the reported pKa of the terminal α-COOH in Fmoc-dipeptides is elevated in comparison.[145] The higher pKa of this functional group is consistent with the pH used in our experimental conditions and supports having a mixture of the protonated and deprotonated forms in the sample.[145] The determination of the pKa's for these samples is a non-trivial matter as they are not readily soluble in aqueous media and the influence of solvent effects on the measured pH of the solution would need to be considered.[146]

The sensitivity of ^{17}O NMR parameters and one's ability to distinguish between unprotected amino acids in their zwitterionic form and the corresponding salts have been extensively discussed.[21,52,63] In these studies, the general trend found for the α-COOH group coordinated with HCl is that the δ_{iso} for C**O** sites tends to higher chemical shifts and the δ_{iso} for C**O**H site is found at lower chemical shifts compared to those for their charged forms. When amino acids are in their zwitterionic form (NH_3^+ and COO^-), the δ_{iso} corresponding to the C**O** and C**O**H sites are shifted to lower and higher chemical shifts, respectively. This can result in two sites having overlapping CT ^{17}O peaks, creating further challenges in extracting the ^{17}O NMR parameters without accessing higher magnetic fields or two-dimensional approaches.

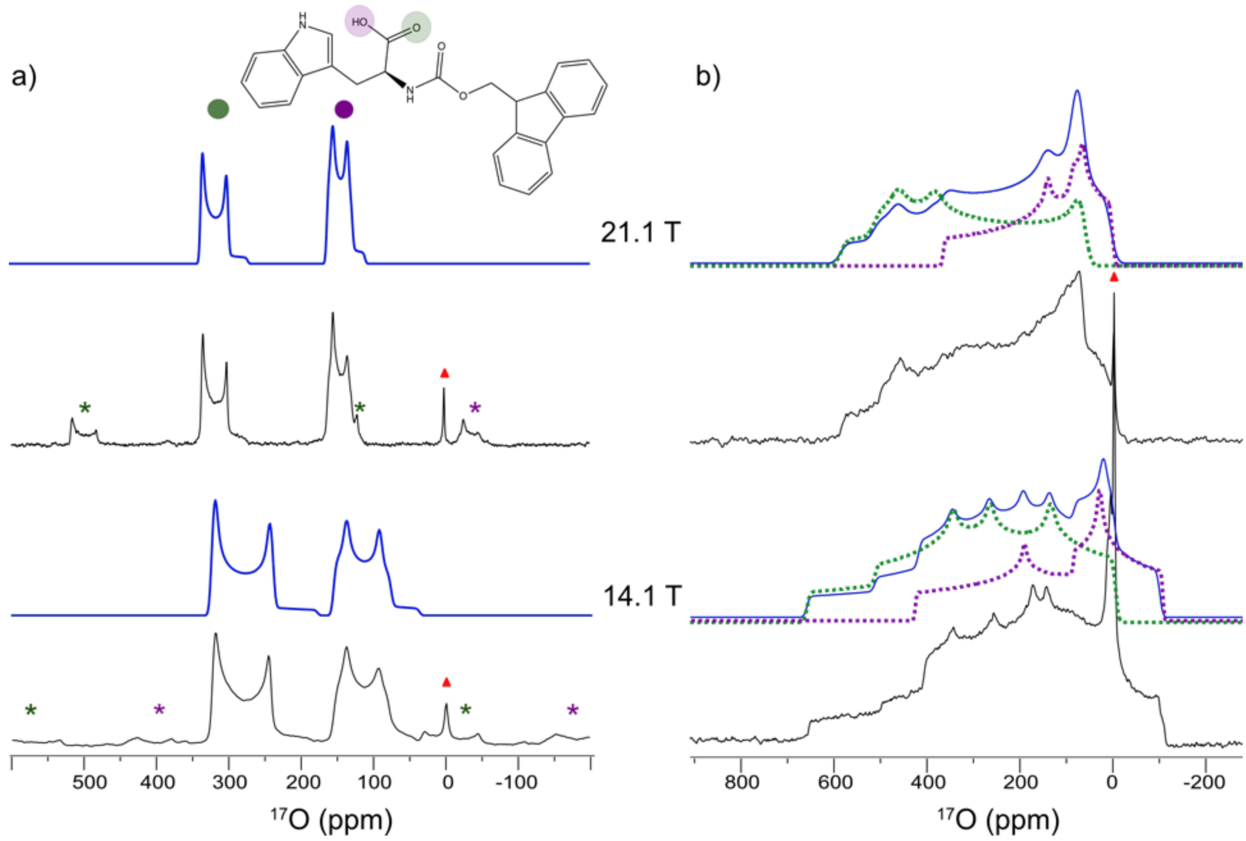

Figure 3.3. ^{17}O NMR spectra of Fmoc-L-tryptophan acquired at 21.1 and 14.1 T. The experimental (black) and simulated (blue) MAS spectra with an inset of the structure of Fmoc-L-tryptophan are shown in (a). The two labelled oxygen sites of the protected amino acid are indicated with a purple (hydroxyl) and green (carbonyl) circle in both the structure and above the spectrum. The spinning side bands are indicated with asterisks and the signal due to residual water is denoted with a red triangle at 0 ppm. The stationary spectra of Fmoc-L-tryptophan are shown in (b) and the individual C**O** (green) and C**O**H (purple) sites are overlaid with the entire simulated spectrum (blue). The NMR parameters used for simulating these spectra are reported in Table 4.

These spectral changes have been attributed to the sensitivity of the ^{17}O NMR parameters, particularly δ_{iso} and C_Q, to changes in the hydrogen-bonding environment. Both these parameters have been observed to decrease when stronger hydrogen bonds are formed.[36,37,149,150] Comparing the δ_{iso} trends observed in unprotected amino acids, the broad peak we observe in Figure 3.4 (yellow circle) is consistent with the presence of a small amount of deprotonated (α-COO$^-$) Fmoc-

amino acid in our sample, *vide infra*. For example, solution ^{17}O NMR has recently emerged as an excellent tool for determining the pKa of different functional groups within proteins given the ^{17}O chemical shifts are highly responsive to changes in ionization states.[38] For instance, the pKa of a C**O**H group from a ^{17}O-labelled glycine residue within ubiquitin was determined to be 2.32 and the chemical shift range was 16 ppm between the fully protonated and deprotonated forms.[38] This nearly covers the entire ^{1}H chemical shift range! Coupled with the wider chemical shift range, an ^{17}O NMR spectrum is much less crowded compared to that for conventional spin-½ nuclei where uniform enrichment is often used, making the determination of the pKa for biologically relevant systems via ^{17}O NMR very enticing. For a more extensive discussion on the impact ionization has on ^{17}O NMR parameters of the α-COOH and side chain groups in amino acids and the insights that can be gained from these parameters on hydrogen bonding in biological molecules, the reader is directed elsewhere.[71,151–153]

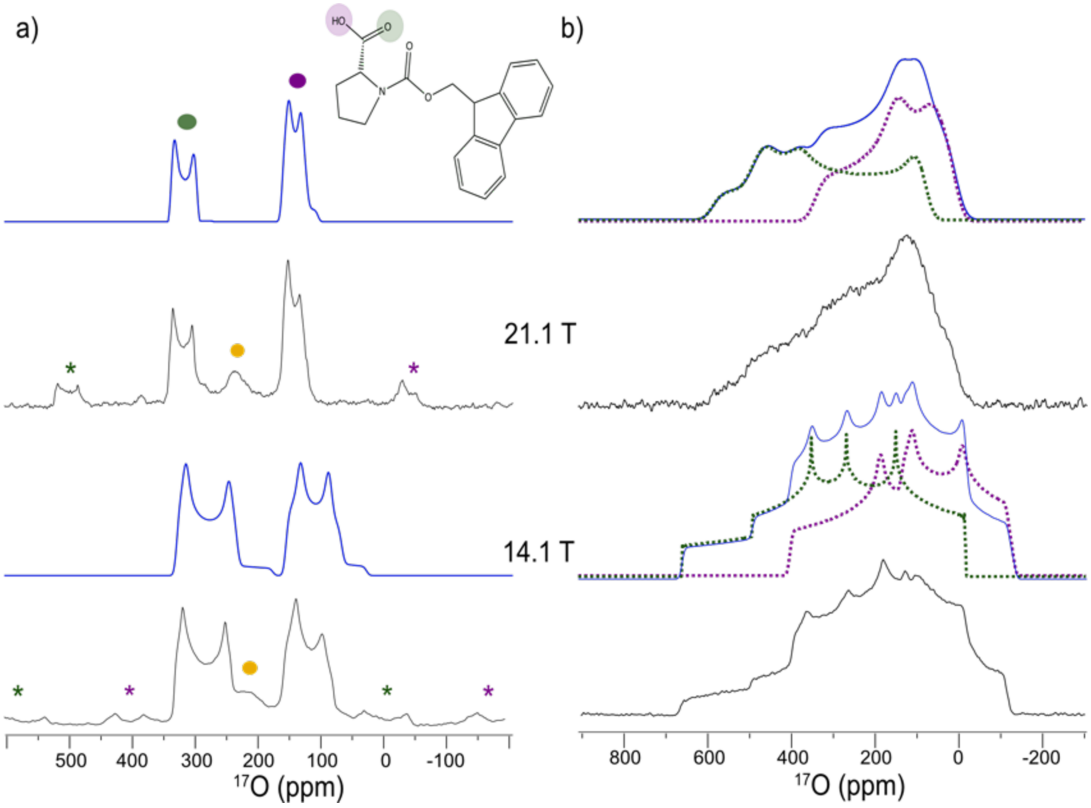

Figure 3.4. Experimental (black) and simulated (blue) ^{17}O NMR spectra of Fmoc-L-proline. Spectra for both the MAS (a) and stationary (b) samples were acquired at 21.1 and 14.1 T. The structure of Fmoc-L-proline (inset on a) shows the two isotopically enriched sites of the

protected amino acid and the peaks attributed to the hydroxyl (purple circle) and carbonyl (green circle) oxygens are shown above the MAS spectra. The spinning side bands (asterisks) are visible in the experimental MAS spectra, along with a broad peak (yellow circle) likely corresponding to the carboxylate ion. The simulations of the ^{17}O sites in the non-spinning spectra (b) are shown for the individual C**O** (green) and C**O**H (purple) sites and are overlaid with the entire simulated spectrum (blue) at both magnetic field strengths.

The ^{17}O MAS NMR spectrum for Fmoc-L-tyrosine (Figure 3.5a) at 21.1 T also has the broad peak (yellow circle) we associate with the presence of deprotonated α-COO^-. The MS spectra again support this assumption, as no other species were detected. The MAS NMR spectrum shown for Fmoc-L-threonine at 21.1 T (Figure 3.5c) was obtained after the sample had been partially recrystallized. The conditions used for recrystallization reduced the % enrichment to ~ 15 ± 5% which also explains the relatively more intense ^{17}O peak from the ZrO_2 rotor (orange diamond). The experimental spectrum (Figure 3.5c, black) of Fmoc-L-threonine also has a broadened baseline. The broadening is attributed to the partial recrystallization of the sample, as the underlying resonances align with those obtained from the lyophilized sample (Figure 3.6). However, in the lyophilized sample, (Figure 3.6a) the broad peak at ~270 ppm (yellow circle) is present, indicating the deprotonated form is found in this sample as well. The unresolved splitting of the central transition peaks in the lyophilized powder sample is indicative of a high degree of molecular conformations and local disorder. When studying the amorphous lyophilized forms of biological samples via ssNMR spectroscopy, numerous concerns have arisen,[154] surrounding how accurately physical properties, like bioavailability and stability, are reflected. Also, with more structural inhomogeneity, high-resolution ssNMR spectra are not easily obtained without some amount of rehydration and/or selective isotopic enrichment.[105,155,156] This can be observed in Figure 3.6, as the ^{17}O NMR parameters determined from the lyophilized and recrystallized sample differ, showing the importance of crystallinity and pKa in extracting representative and accurate NMR parameters. Provided an iterative process was employed using WSolids1 to determine the NMR parameters that offered the best unique fit to the experimental NMR spectra at both magnetic field strengths, the errors associated with the ^{17}O parameters reported in Table 1 reflect a range for a given parameter where either no change or a small change in the simulated spectra was observed.

Further refinements to the NMR parameters may be required to account for the presence of both the deprotonated species and low crystallinity observed in the Fmoc-L-proline, -tyrosine and -threonine samples, especially for the CSA parameters extracted from the non-spinning spectra, when a phase-pure sample can be obtained.

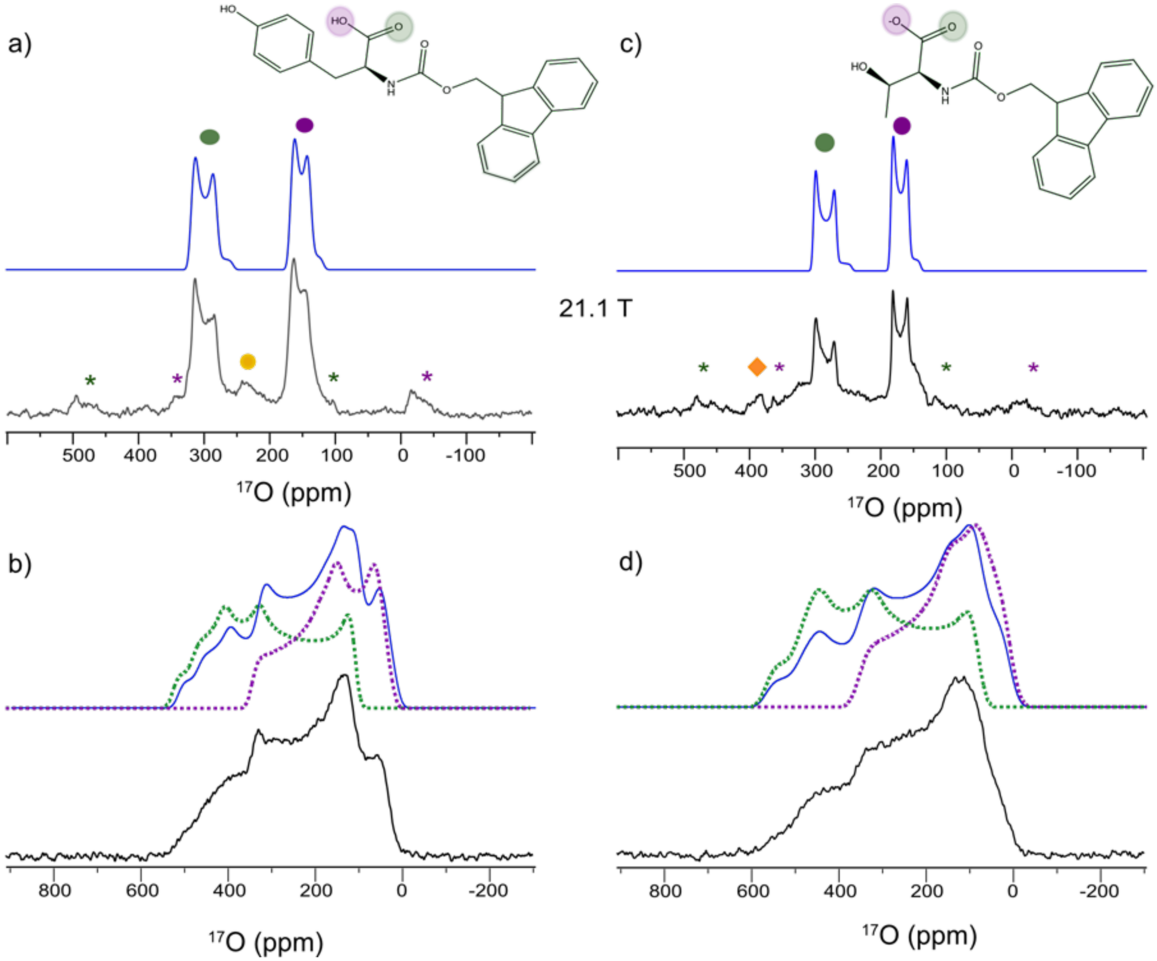

Figure 3.5. Experimental (black) and simulated (blue) ^{17}O NMR spectra of Fmoc-L-tyrosine (a,b) and Fmoc-L-threonine (c,d) at 21.1 T. The structure of each amino acid is inset above the corresponding MAS spectrum (a,c) and the hydroxyl (purple circle) and carbonyl (green circle) peaks are indicated along with the spinning sidebands (asterisks). The experimental MAS spectrum in (a) shows an additional peak at ~ 240 ppm (yellow circle) whereas a ZrO_2 peak is visible (orange diamond) in (c). The stationary spectra at 21.1 T are shown in (b) and (d) with the simulation of the C**O** (green) and C**O**H (purple) sites overlaid with the entire simulated spectrum (blue). All parameters used to simulate the spectra are included in Table 4.

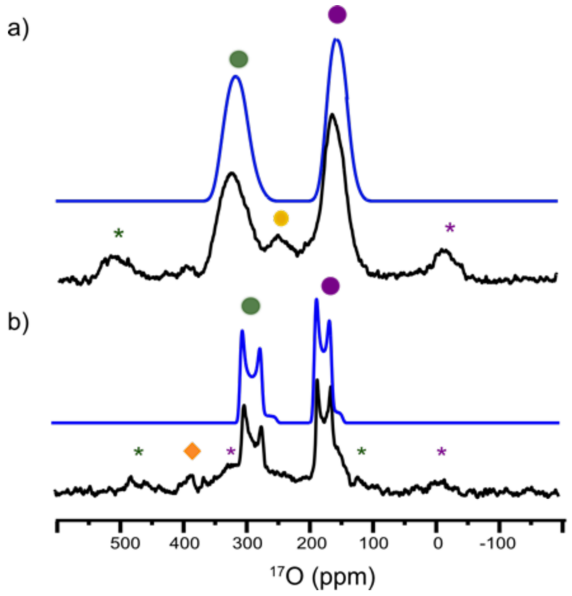

Figure 3.6. Experimental (black) and computed (blue) MAS NMR spectra of lyophilized (a) and recrystallized Fmoc-L-threonine (b) acquired at 21.1 T. The CO (green circle) and COH (purple circle) ^{17}O NMR parameters are as follows: δ_{iso} = 343 and 174 ppm, C_Q = 8.5 and 7.4 MHz and η = 0.50 and 0.40, respectively, for the lyophilized sample (a) and δ_{iso} = 311 and 192 ppm, C_Q = 8.1 and 7.2 MHz and η = 0.05 and 0.08, respectively, for the recrystallized sample (b). The orange diamond in (b) indicates ^{17}O signal from the ZrO_2 from the NMR rotor and the coloured asterisks indicate spinning sidebands.

Both the Fmoc-L-tyrosine and Fmoc-L-threonine samples have less defined spectral features (Figure 3.5) compared to those for the other three Fmoc-amino acids studied; as such the ^{17}O parameters reported have slightly larger errors associated with them (Table 4). Nevertheless, the simulated spectra (blue) provide a good reference of their unique ^{17}O NMR parameters. The ^{17}O NMR parameters for the C**O** and C**O**H groups in Fmoc-L-tyrosine (Figures 3.5a and 3.5b) are as follows: δ_{iso} = 328 ± 1 and 176 ± 1 ppm, Ω = 460 ± 100 and 210 ± 100 ppm, κ = 0.65 ± 0.50 and -1.00 ± 0.50, C_Q = 8.4 ± 0.2 and 7.4 ± 0.2 MHz and η = 0.18 ± 0.05 and 0.22 ± 0.05 respectively. The ^{17}O NMR parameters for the C**O** and C**O**H groups in Fmoc-L-threonine (Figures 3.5c and 3.5d) are as follows: δ_{iso} = 311 ± 1 and 192 ± 1 ppm, Ω = 530 ± 100 and 255 ± 100 ppm, κ = 0.48

± 0.50 and -0.75 ± 0.50, C_Q = 8.1 ± 0.2 and 7.2 ± 0.2 MHz and η = 0.05 ± 0.05 and 0.08 ± 0.05 respectively.

3.2.3 Quantum Chemical Computations of ^{17}O Fmoc-Amino Acids

In addition to experimental ^{17}O NMR data for these five Fmoc-amino acids, a series of DFT computations were performed to evaluate and compare *in silico* ^{17}O NMR parameters with the experimental results (Table 4). To convert the magnetic shielding to chemical shift values, an absolute ^{17}O magnetic shielding value of 287.5 ppm for water at 300 K was used (eq. 2.8).[157] All computed NMR parameters reported in Table 4 are those obtained from structures after a single-molecule geometry optimization to evaluate how well this molecular model performed at predicting ^{17}O NMR parameters and tensor orientations. The program, EFGshield (version 4.5),[139] was used to evaluate the Euler angles from the ADF output files. We have included the experimental ^{17}O NMR data from previously published studies of Fmoc-L-alanine, -serine, -leucine and -valine[46,143] to expand the number of molecules being compared with the computed parameters (Table 4). We note an error in the reported span for the C**O** sites in Fmoc-L-leucine and -valine by Keeler *et al.* (2017)[46] and have re-simulated their non-spinning NMR spectra at 17.6 T using spans of 530 and 540 ppm, respectively (Figure 3.7). All other NMR parameters were consistent with what is reported in Table 4.

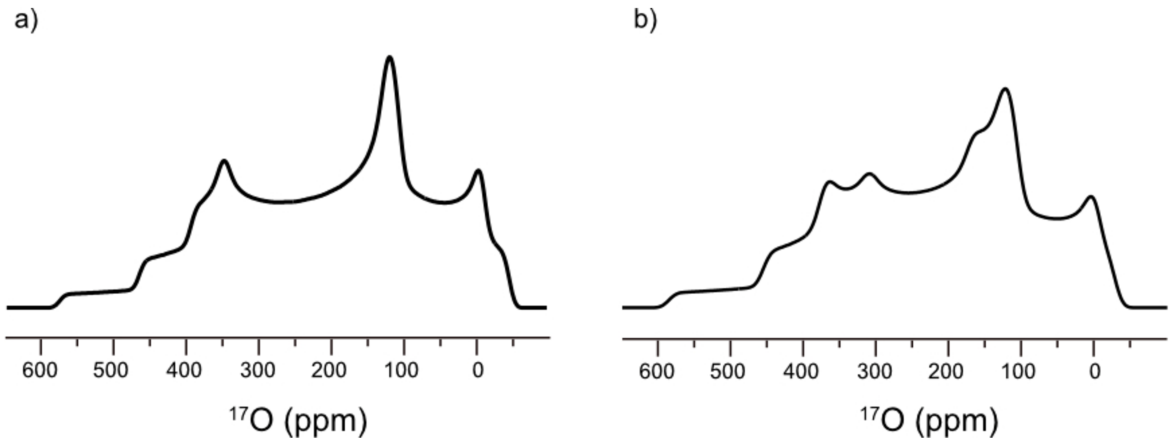

Figure 3.7. Simulation of non-spinning NMR spectra at 17.6 T for Fmoc-L-leucine (a) and Fmoc-L-valine (b) using the ^{17}O NMR parameters reported from Keeler *et al.* (2017). Spans (Ω) for the C**O** site were amended to 530 and 540 ppm, respectively. All other NMR parameters are identical to what are reported in Table 4.

A statistical comparison of the computed CSA parameters with the experimental values is shown in Table 5 and provides an average deviation of the computed NMR parameters from our results. Overall, the calculated CSA parameters agree well with the experimental ^{17}O NMR parameters, especially for the δ_{xx} tensor components (Fig. 3.8a and b). The computed CSA tensor components for the C**O** site (Fig. 3.8a) have average deviations of 64 (δ_{11}), 97 (δ_{22}) and 20 (δ_{33}) ppm from experimental values. For the C**O**H site (Fig. 3.8b), the average deviations are smaller for the δ_{11} and δ_{22} components (28 and 63 ppm, respectively) compared to the C**O** site but are larger for the δ_{33} (35 ppm). There is also a consistent overestimation of the δ_{22} and underestimation of the δ_{33} components for the C**O**H site. When fit to a linear equation (Figs. 3.8a and 3.8b) with a set intercept of 0, the CSA tensor components for the C**O** and C**O**H sites have R^2 values of 0.97 and 0.88, respectively and yield slopes of ~ 1.1. This demonstrates that the computed CSA tensors agree well with our experimental results. Figure 3.9 shows the overall correlations between the δ_{iso} (Fig. 3.9a), Ω (Fig. 3.9b) and κ (Fig. 3.9c), where the computed CSA parameters have average deviations from the experimental results of 47 ppm, 77 ppm and 0.32, respectively, for the C**O** site and 18 ppm, 55 ppm and 0.56 for the C**O**H site (Table 5).

Table 5. Average deviations of the computed vs. experimental ^{17}O NMR parameters plotted in Figures 3.8 & 3.9 for the C**O** and C**O**H sites in the Fmoc-amino acids.

^{17}O Site	δ_{iso} (ppm)	Cq (MHz)	η	q_{zz} (a.u.)	q_{yy} (a.u.)	q_{xx} (a.u.)	Ω[5] (ppm)	κ	δ_{11} (ppm)	δ_{22} (ppm)	δ_{33} (ppm)
C**O**	47	0.4	0.11	0.07	0.10	0.07	77	0.32	64	97	20
C**O**H	18	1.2	0.33	0.20	0.35	0.16	55	0.56	28	63	35

[5] The deviations were calculated using the re-evaluated experimental span values for the C**O** sites in Fmoc-L-valine and -leucine, which in turn were used to extract the CSA tensor components. All correlations were calculated using the equation: $[(\Sigma(\text{calc.} - \text{expt.})^2)/(n)]^{1/2}$.

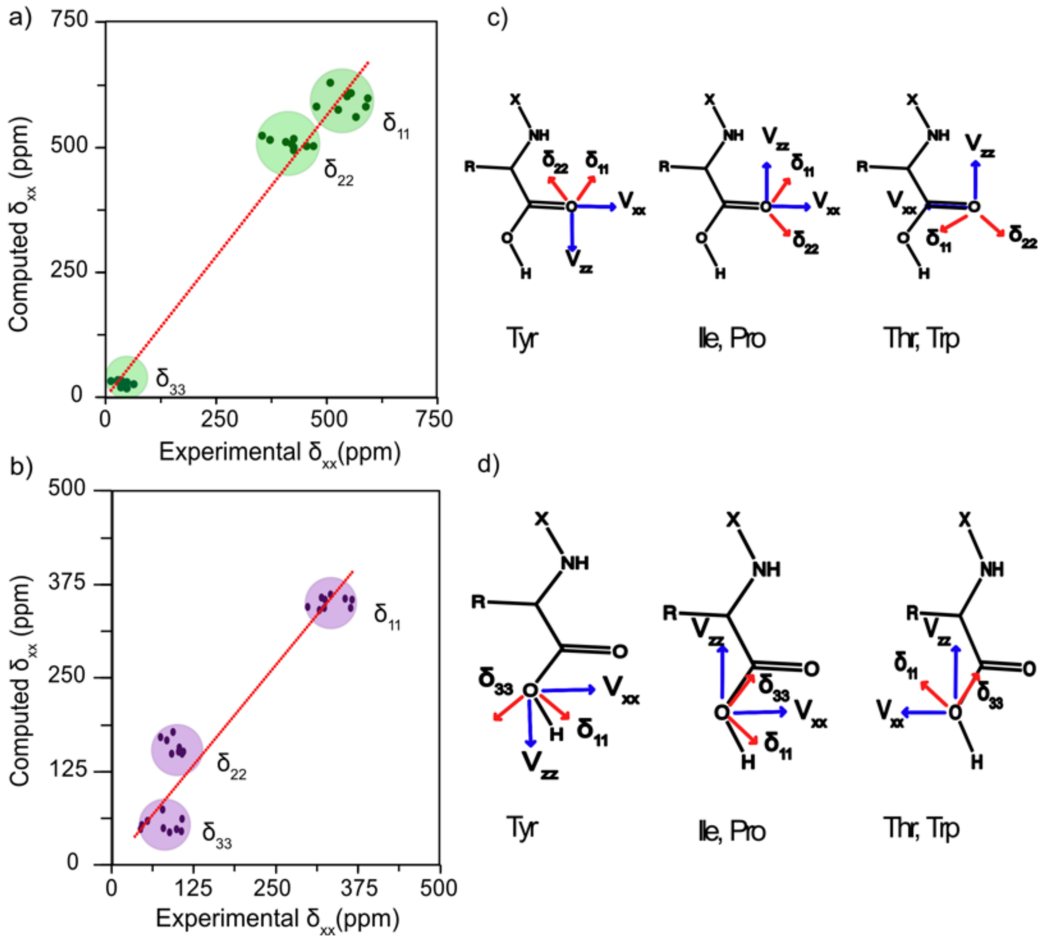

Figure 3.8. Comparison of the computed and experimental ^{17}O CSA tensor components (a, b) and the predicted EFG and CSA tensor orientations (c, d) for Fmoc-amino acids. The tensor components for Fmoc-L-isoleucine, tryptophan, proline, tyrosine and threonine from this study and the experimental data for Fmoc-L-serine, alanine, valine and leucine from previously published results were used to construct these plots.[46,143] The amended span values for the C**O** site of Fmoc-L-leucine and Fmoc-L-valine[46] were used to extract the experimental CSA tensor components. All computed and experimental ^{17}O NMR parameters are summarized in Table 4. The relative orientations of the EFG (blue) and CSA (red) tensors for the five geometry-optimized structures at either the C**O** (c) or C**O**H site (d) are shown. There are three similar orientations for each site corresponding to one of the Fmoc-amino acids, which is denoted below the figure. The V_{yy} tensor component is oriented out of the page and in (c) the δ_{33} are coincident with V_{yy} in all structures and in (d) the δ_{22} component overlaps with the V_{yy}.

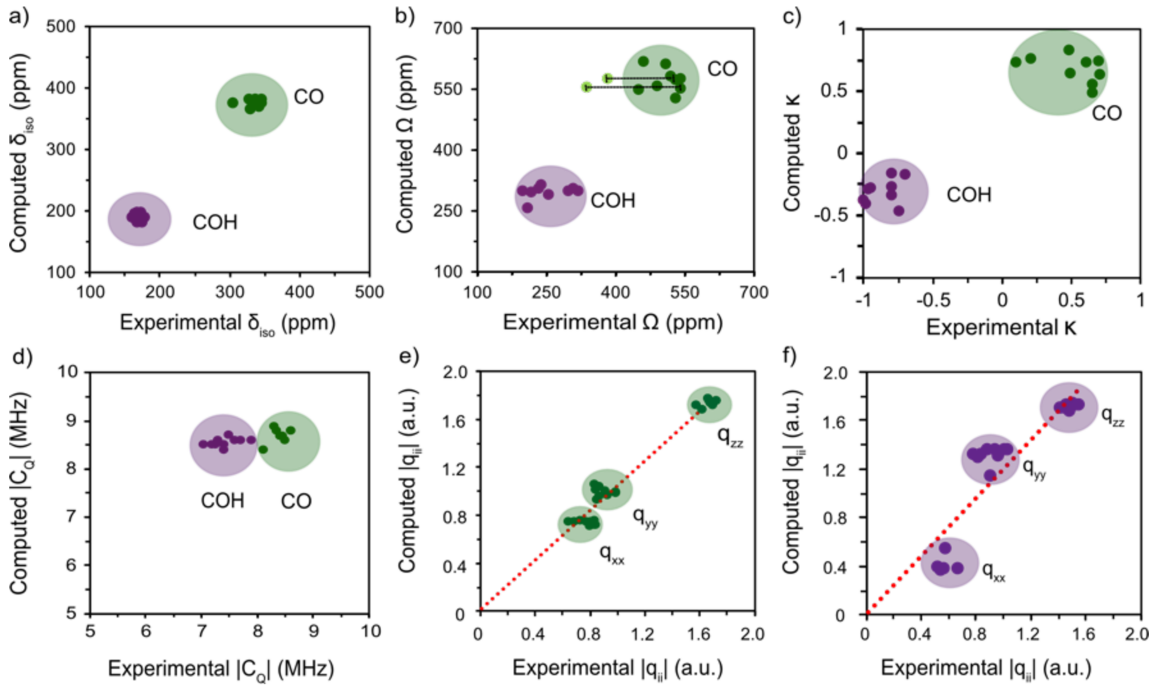

Figure 3.9. Comparison of the computed and experimental ^{17}O NMR parameters for the isotropic chemical shift (a), span (b) and skew (c) along with the C_Q (d) and EFG tensor components for the C**O** (e) and C**O**H site (f) for the FMOC amino acids listed in Table 4. The average deviations of the computed values compared to the experimental NMR parameters are listed in Table 5. The light green markers in (b) indicate published span parameters for the C**O** site of Fmoc-L-leucine and -valine[45] with error bars to re-evaluated span values (Fig. 3.7). In (e) and (f) the trend lines have a intercept of 0 and the q_{ii} components were extracted from the C_Q (eqn. 2.18) and η (eqn. 2.19) values.

Extending this statistical comparison to the EFG tensor components, we found the average deviations in the computed and experimental values for the C**O** site were 0.07 (q_{zz}), 0.10 (q_{yy}) and 0.07 (q_{xx}) a.u. (Table 5). The computed values for the EFG components at this site agree very well with experimental results and when plotted together can be fit to a linear trend line with a slope of 1.0 and a R^2 value of 0.96 (Figure 3.9e). Comparatively larger average deviations were observed for the computed EFG tensors at the C**O**H site from our experimental results. The largest deviation

was found for the q_{yy} component (0.35 a.u.) and when plotted together with the other EFG tensors at this site, a reasonably good fit between the calculated vs. experimental values was obtained (Figure 3.9f). When equating the data to a linear line and setting the intercept to 0, we obtained a slope of 1.2 and an R^2 value of 0.81. The divergence from linearity can easily be reconciled as there is a consistent overestimation in the computed values of q_{yy} and underestimation of the computed q_{xx} values.

Since each of these EFG tensors are tied to the C_Q (eqn. 2.18) and η values (eqn. 2.19), it is important to relate them to the experimental values reported in Table 4. First, the experimental C_Q values reported are the absolute values as the sign for each oxygen site cannot be determined from these experimental results, whereas the computed values contain the predicted sign. The DFT computations predict a positive C_Q for the C**O** site and a negative C_Q for the C**O**H site, consistent with past computational results for Fmoc-amino acids.[143] Given the C_Q is linked directly to the V_{zz} component for each site, the sign and magnitude of the C_Q is determined from this EFG tensor component. For the C_Q of the C**O**H site, an average deviation of 1.2 MHz was calculated compared to the typical 7.4 MHz obtained from the experimental results. The range of computed values for the C**O**H sites present a statistically significant variation from the experimental C_Q values. Yet, the deviation for the calculated C_Q values for the C**O** site was much smaller (0.4 MHz). This observation is similar to that reported by Yamada and co-workers for the C**O** sites of the two Fmoc-amino acids they modelled.[143] However, in the former study, the difference between computational and experimental C_Q values was reduced to ~0.3 MHz for the C**O**H sites.[143] This refinement may be attributed to the additional hydrogen bonding interactions between the target compound and other Fmoc and water molecules that their cluster model included.

Although improvements are observed in the calculated C_Q values for the C**O**H site using this more complex cluster model, the improvements do not extend to their computed η values for the C**O**H site. This study still reports computed η values for C**O**H sites that are approximately two times larger than their experimental η[143] and is consistent with the overestimation of the computed η values using our molecular model. This can be linked to larger average deviations in the EFG tensor components for this site, which includes the underestimation of the q_{xx} and overestimation of the q_{yy} components in all cases (Figure 3.9f). This finding insinuates that the inclusion of hydrogen bonding interactions is not solely responsible for the variations observed between

computational models and could be attributed to the freedom (i.e., dynamics) of the terminal hydroxyl group that would likely be more susceptible to the crystal arrangement and associated impacts of the intermolecular structure (e.g., hydrogen bonding, dynamics, water coordination, etc.) due to the sensitivity of the electric field gradient about its medium range structure.[85]

Given the fair accuracy between our computed ^{17}O CSA and EFG tensor components with the experimental results, we have evaluated how the computed EFG and CSA tensors are oriented with respect to each other. The predicted orientations of the CSA tensors with respect to the EFG tensors are shown for both the C**O** (Figure 3.8c) and C**O**H (Figure 3.8d) sites for the geometry optimized structures of the Fmoc-amino acids evaluated in this study. There are three similar arrangements that were obtained, where molecules with the Fmoc moiety positioned in relatively the same proximity to the carboxylic acid groups had comparable orientations. For example, the geometry optimized structures of Fmoc-L-proline and -isoleucine have the C**O** group positioned 3.5 Å away from the second carbon on one of the benzene rings of the Fmoc moiety (C8 using the same structure numbering as Yamada *et al.*[143]). In the other three protected amino acids, the C**O** groups are positioned further away from this site (> 5 Å) and are in closer proximity to the their respective sidechain groups. It is likely that the proximity of the Fmoc group to the COOH group in the optimized structures influences the EFG and CSA tensor orientations and leads to the slightly different orientations observed. However, in all cases the δ_{33} component for the C**O** site is predicted to be perpendicular to the backbone of the protected amino acids and is always coincident with the V_{yy} component of the EFG tensor. In contrast, for the C**O**H sites, the V_{yy} and δ_{22} components now overlap and are perpendicular to the backbone and are shown directed out of the plane of the page in Figure 3.8d. The δ_{33} component for the C**O**H site typically lies along the C**O** bond (Figure 3.8d) and the relative orientations of the EFG tensors vary by structure. However, the projected directions of the V_{xx} and V_{zz} components for the C**O** site are notable, as the orientations we obtained are identical to what is predicted for the C**O** site in other carboxylic acids.[69,148] The V_{xx} component is always placed parallel to the C**O** double bond and the V_{zz} tensor component is perpendicular to the double bond in all cases (Figure 3.8c), consistent with the near axial symmetry identified by the experimental η values. Since there is reasonable agreement between the computed and experimental ^{17}O CSA and EFG parameters, we are confident that the predicted orientations of the computed tensors can be extended in the molecular framework for each site.

To evaluate if any relationships exist between the local structure of the molecule for the Fmoc-amino acids with their experimental ^{17}O NMR parameters, we first considered the most common reported structural parameters like the C**O** bond length. An inverse relationship between the δ_{iso}, δ_{22}, and C_Q for the C**O** sites in amino acids and amides has been well established with the C=O bond length.[52,147,150] Unfortunately, there was not a strong correlation between the experimental ^{17}O NMR parameters and the C=O bond lengths measured from the geometry optimized structures. All C=O bond lengths fell into a very narrow range (1.211- 1.217 Å) which are close to the standard 1.22 Å value.[158] The relationship between hydrogen bond distance of the C**O** site and H-N in different amino acid[148] and amide molecules[150] has been reported and influences each of the CSA tenor components. For δ_{11}, δ_{22}, and δ_{iso} a linear relationship is observed, where an increase is seen for these parameters with increasing hydrogen bond length. Conversely, for the δ_{33} tensor component a linear relationship is still observed but this parameter decreases with increasing hydrogen bond distance. We used the available X-ray diffraction structures for Fmoc-L-serine,[159] -isoleucine,[141] -leucine[160] and -tyrosine[142] to further examine the influence of this interaction on the ^{17}O NMR parameters. Figure 3.10 shows the relationship between each of the experimental CSA tensor components as well as δ_{iso} for the C**O** site in these protected amino acids and the intramolecular bond distance between this site and the N-H group. This intramolecular C=O- - H-N bond distance is well correlated with the δ_{iso} and δ_{11} tensor component and maintains the same linear relationship as discussed above and have R^2 values of 0.93 and 0.99, respectively. The trends for the δ_{22} and δ_{33} components and this bond distance are not as strongly connected (Fig. 3.10) and do not show the expected relationship for this type of functional group.[148,150] One possible explanation for this is it is difficult to observe proton positions using X-ray structures due to the mobility and the low electron density of hydrogen (i.e., a single electron). Gervais *et al*. (2005) noted an improvement in the computed CSA values when using the neutron structure over the X-ray structures for L-alanine, suggesting that these tensor components are very sensitive to the proton position.[148] Due to the limited diffraction data available for the Fmoc-amino acids, ^{17}O solid-state NMR spectroscopy could provide further insight into the C=O---H-N interaction, complementing future neutron diffraction studies.

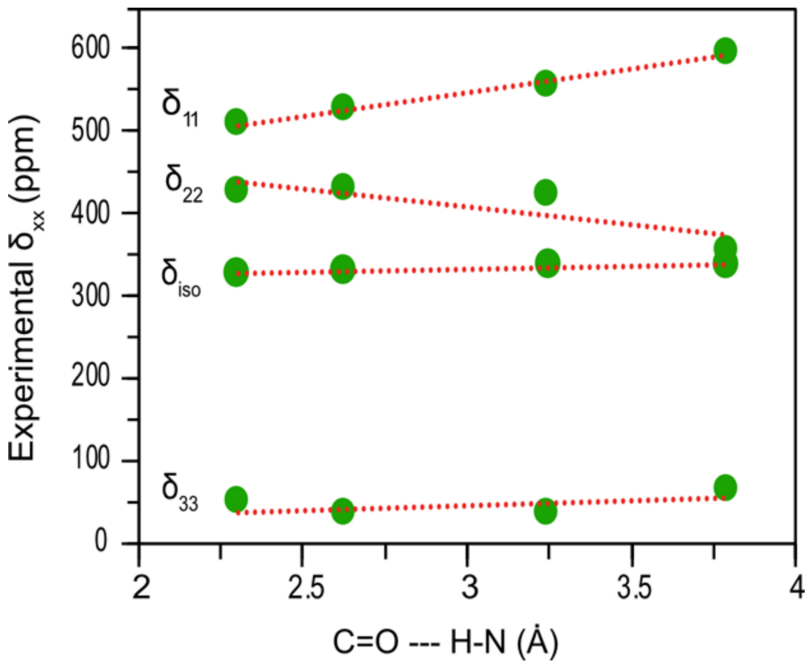

Figure 3.10. Correlation of the intramolecular hydrogen bond distance between the NH and C=O group from X-ray structures with the experimental CSA tensor components for the carbonyl oxygen site. X-ray structures of Fmoc-L serine (CIF-4514078), -tyrosine (CIF-7220755), -isoleucine (CIF-2219071) and -leucine (CIF-2218405) were used to measure the distance between the C=O and H-N groups in each molecule. The linear correlations are as follows : δ_{11} ($y = 56.5x + 376.6$, $R^2 = 0.99$), δ_{22} ($y = -45.0x + 543.2$, $R^2 = 0.71$), δ_{iso} ($y = 7.3x + 311.4$, $R^2 = 0.93$) and δ_{33} ($y = 10.4x + 14.5$, $R^2 = 0.24$).

Refinements to computed ^{17}O NMR parameters have been observed when both neutron structures and a cluster model approach have been utilized.[37] Dong et. al (2000) studied the hydrogen bonding effects in urea by building a molecular cluster using 1-7 molecules and continued to see sequential improvements to the computed CSA tensor components through to the final cluster. However, the computational time to conduct the chemical shielding calculations for the 7-molecule cluster was 5 days[37] and would take substantially longer as the molecule size increased. In fact, the computed clusters used to evaluate the ^{17}O NMR parameters for Fmoc-L-serine and -alanine modified the surrounding molecules with methyl groups in place of the larger aromatic fragments to reduce computational time.[143] As discussed above, the errors in the computed ^{17}O NMR parameters from this cluster model study were comparable to the errors

obtained via the molecular model used in this study. This supports that a basic molecular model can provide an adequate estimation for users seeking to simulate ^{17}O NMR parameters.

To further evaluate whether our computational method could correctly predict the changes between the deprotonated and protonated Fmoc-amino acids that we observe experimentally (*vide supra*), we computed models of both species. In Fig. 3.11, we show simulated MAS NMR spectra for the deprotonated and protonated forms of two Fmoc-amino acids and show how the computed C_Q and δ_{iso} parameters for each species impact the appearance of the central transition peaks at 14.1 T. These computed parameters show the expected trend of the C**O** site having C_Q and δ_{iso} values that decrease from the protonated to deprotonated forms, whereas the C_Q and δ_{iso} for the C**O**H site both increase with the changes in ionization state. When the NMR spectra of the deprotonated amino acids are simulated, the two ^{17}O peaks in Fmoc-L-tyrosine (Figure 3.11a) and Fmoc-L-isoleucine (Figure 3.11b) are predicted to overlap with one another. These DFT results further support our assignments of the peak at ~270 ppm in Fig. 3.4 and 3.5 to a small amount of deprotonated α-COO^- in the protected amino acids. In general, the computational approach we have outlined for calculating the ^{17}O EFG and CSA parameters show comparable trends to computations that implemented more complex structural models[143] and provides users with a valuable method to estimate ^{17}O NMR parameters prior to costly isotopic enrichment that can be carried out within minutes rather than days using this *in silico* screening approach.

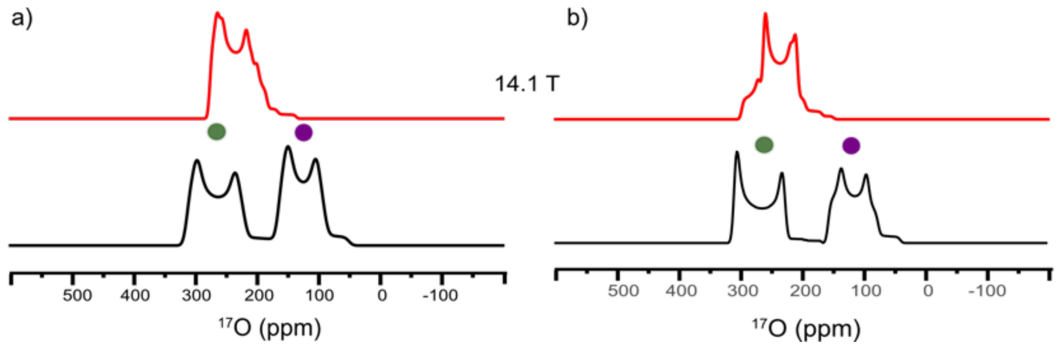

Figure 3.11. Simulated MAS NMR spectra of deprotonated (red) and protonated (black) Fmoc-L-tyrosine (a) and Fmoc-L-isoleucine (b) at 14.1 T. Deprotonated spectra were simulated using new computed NMR parameters for δ_{iso} and C_Q after a proton was removed from the original geometry-optimized structures. The asymmetry values (η) were held constant between both

species and the δ_{iso} and C_Q for the C**O** (green circle) and C**O**H (purple circle) sites in the protonated FMOC-amino acids are reported in Table 4.

3.3 Summary of Results

By utilizing a more efficient ^{17}O-enrichment technique and combining the NMR data with a robust computational approach, we have successfully shown that ^{17}O ssNMR spectroscopy can be incorporated more readily into research than ever before. Using two magnetic field strengths (14.1 and 21.1 T), as well as MAS and non-spinning experiments, ^{17}O NMR parameters were determined for five previously uncharacterized Fmoc-amino acids. This expands the available ^{17}O literature on these important building blocks in biomolecular research. Our results are in line with previously reported ^{17}O NMR parameters for Fmoc-amino acids[46,143] and further demonstrate the sensitivity of ^{17}O EFG and CSA parameters to their molecular structure. Furthermore, DFT computations were used as an approach to distinguish between deprotonated and protonated forms of the α-COOH in Fmoc-amino acids. The adoption of this method will further enhance the application of solid-state NMR experiments for biomolecular studies. In most cases, the sensitivity provided by high labelling produced publishable ^{17}O NMR spectra within an hour, while the agreement between the DFT and experimental results allow one to screen modelling constraints for biomolecules.

Chapter 4: Concluding Remarks and Future Work

4.1 Conclusions

This thesis has provided an overview of why NMR spectroscopy is a powerful tool used to investigate the structure and dynamics of biological systems. It has showcased some of the most recent and exciting advances taking place in ^{17}O NMR spectroscopy and how this area is continuously addressing the issues associated with introducing this challenging quadrupolar nuclei into biological studies. The primary work described here focused on extending the multiple-turnover reaction to isotopically enrich Fmoc-L-isoleucine, -tryptophan, -proline, -tyrosine and -threonine with ^{17}O at the α-COOH sites for the first time. These ^{17}O-protected amino acids were then characterized using 1D ^{17}O ssNMR experiments and the results were compared with ^{17}O NMR parameters computed from a single geometry-optimized molecule. By utilizing multiple magnetic field strengths and a labelling protocol that yields a high percent incorporation of ^{17}O, we were able to obtain experimental ^{17}O NMR parameters that were aligned with previous published results for this subset of molecules[46,143] and extended the available ^{17}O NMR data for protected amino acids. This work has also demonstrated how combining these two relatively simple measures could bolster the effectiveness for ^{17}O ssNMR studies in the future.

4.2 Future Directions

The natural continuation of this work would be to exploit the ^{17}O-labelled Fmoc-amino acids for their intended purpose as building blocks for a synthetic peptide. One such peptide that could be of interest to study by ^{17}O ssNMR spectroscopy is the heptapeptide, GNNQQNY. This peptide is a small fragment from the N-terminal region of the *Saccharomyces cerevisiae* protein, Sup35p, which has a propensity for forming amyloid fibrils.[161–163] Amyloid fibrils occur in normally soluble proteins and are characterized by the formation of fibrous aggregates that are resistant to degradation. The presence of such aggregates are linked to a wide range of neurodegenerative diseases like Alzheimer's, Parkinson's and Huntington's, and the mechanism for the onset of misfolding is still unknown. An indicator that a protein may form fibrils is in its primary sequence as they characteristically have highly repetitive segments. For instance, Sup35p is a protein composed of 685 residues and in the first 123 residues, 78% of the primary sequence is composed of only 4 amino acids (glutamine (Q), asparagine (N), tyrosine (Y) and glycine

(G)).[164] GNNQQNY was adopted as a model system for studying fibril formation as it is one of the shortest stand-alone peptides that could mimic the fibrils formed in its parent protein.[161,165–167]

GNNQQNY has been extensively studied using ssNMR spectroscopy.[164,168–171] The highly repetitive motif of this peptide made it difficult to distinguish alike residues from one another and was addressed by segmentally labelling the peptide to obtain unambiguous NMR assignments for each residue. This allowed investigators to characterize the different crystal and fibril structures that were adopted by this peptide.[164,169] There are two crystal structures[165,166,172] and three different fibril forms that have been reported for this peptide.[164,169] The monoclinic and orthorhombic structures associated with GNNQQNY can be obtained based on peptide concentration, whereas the fibril forms coexist at higher concentrations. There are notable differences between the ^{13}C and ^{15}N chemical shifts in the ssNMR spectra of the crystal structures and between each of the fibrils forms.[164] One remarkable distinction between the crystal structures is the mobility of the tyrosine residue.[164] In the monoclinic form, the ^{13}C signals associated with the aromatic ring are present, whereas in the orthorhombic form no ^{13}C signals were detected for this residue. This indicates that the tyrosine is more mobile in the orthorhombic structure. The flexibility associated with the tyrosine residue is extended to the fibril forms. Other differences have been identified between these structures and analyzing this peptide using ^{17}O as a probe may provide further insights into the structural differences described for GNNQQNY. By examining and establishing an ^{17}O ssNMR approach in this model peptide, a similar methodology could be extended to investigate the more complex fibril formation in proteins linked with human diseases.

References

(1) Jacobson, B.; Anderson, J. T.; Arnold, W. A. A Proton Magnetic Resonance Study of the Hydration of Deoxyribonucleic Acid. *Nature* **1954**, *173*, 772.

(2) Saunders, M.; Wishnia, A.; Kirkwood, J. G. The Nuclear Magnetic Resonance Spectrum of Ribonuclease. *J Am Chem Soc* **1957**, *79*, 3289.

(3) Sklenář, V.; Bax, A. Spin-Echo Water Suppression for the Generation of Pure-Phase Two-Dimensional NMR Spectra. *Journal of Magnetic Resonance* **1987**, *74*, 469–479.

(4) Hors, P. J. A New Method for Water Suppression in the Proton NMR Spectra of Aqueous Solutions. *Journal of Magnetic Resonance* **1983**, *54*, 539–542.

(5) Muchmore, D. C.; McIntosh, L. P.; Russell, C. B.; Anderson, D. E.; Dahlquist, F. W. Expression and Nitrogen-15 Labeling of Proteins for Proton and Nitrogen-15 Nuclear Magnetic Resonance. *Methods in Enzymology* **1989**, *177*, 44–73.

(6) Venters, R. A.; Calderone, T. L.; Spicer, L. D.; Fierke, C. A. Uniform ^{13}C Isotope Labeling of Proteins with Sodium Acetate for NMR Studies: Application to Human Carbonic Anhydrase II. *Biochemistry* **1991**, *30*, 4491–4494.

(7) Cai, M.; Huang, Y.; Sakaguchi, K.; Clore, G. M.; Gronenborn, A. M.; Craigie, R. An Efficient and Cost-Effective Isotope Labeling Protocol for Proteins Expressed in Escherichia Coli. *Journal of Biomolecular NMR* **1998**, *11*, 97–102.

(8) Furrer, J. A Comprehensive Discussion of HMBC Pulse Sequences, Part 1: The Classical HMBC. *Concepts in Magnetic Resonance Part A: Bridging Education and Research* **2012**, *40 A*, 101–127.

(9) Wüthrich, K. NMR with Proteins and Nucleic Acids. *Europhysics News* **1986**, *17*, 11–13.

(10) Bodenhausen, G.; Ruben, D. J. Natural Abundance Nitrogen-15 NMR by Enhanced Heteronuclear Spectroscopy. *Chemical Physics Letters* **1980**, *69*, 185–189.

(11) Pervushin, K.; Riek, R.; Wider, G.; Wüthrich, K. W. Attenuated T_2 Relaxation by Mutual Cancellation of Dipole-Dipole Coupling and Chemical Shift Anisotropy Indicates an

Avenue to NMR Structures of Very Large Biological Macromolecules in Solution. *Proceedings of the National Academy of Sciences* **1997**, *94*, 12366–12371.

(12) Opella, S. J.; Marassi, F. M. Applications of NMR to Membrane Proteins. *Archives of Biochemistry and Biophysics* **2017**, *628*, 92–101.

(13) Tycko, R. Biomolecular Solid State NMR: Advances in Structural Methodology and Applications to Peptide and Protein Fibrils. *Annual Review of Physical Chemistry* **2001**, *52*, 575–606.

(14) Tycko, R. Solid-State NMR Studies of Amyloid Fibril Structure. *Annual Review of Physical Chemistry* **2011**, *62*, 279–299.

(15) Palmer, A. G.; Williams, J.; McDermott, A. Nuclear Magnetic Resonance Studies of Biopolymer Dynamics. *Journal of Physical Chemistry* **1996**, *100*, 13293–13310.

(16) Reif, B.; Ashbrook, S. E.; Emsley, L.; Hong, M. Solid-State NMR Spectroscopy. *Nature Reviews Methods Primers* **2021**, *1*, 1–23.

(17) Reif, B.; Griffin, R. G. ^{1}H Detected ^{1}H,^{15}N Correlation Spectroscopy in Rotating Solids. *Journal of Magnetic Resonance* **2003**, *160*, 78–83.

(18) Barbet-Massin, E.; Pell, A. J.; Retel, J. S.; Andreas, L. B.; Jaudzems, K.; Franks, W. T.; Nieuwkoop, A. J.; Hiller, M.; Higman, V.; Guerry, P.; Bertarello, A.; Knight, M. J.; Felletti, M.; Le Marchand, T.; Kotelovica, S.; Akopjana, I.; Tars, K.; Stoppini, M.; Bellotti, V.; Bolognesi, M.; Ricagno, S.; Chou, J. J.; Griffin, R. G.; Oschkinat, H.; Lesage, A.; Emsley, L.; Herrmann, T.; Pintacuda, G. Rapid Proton-Detected NMR Assignment for Proteins with Fast Magic Angle Spinning. *Journal of the American Chemical Society* **2014**, *136*, 12489–12497.

(19) Bertini, I.; Emsley, L.; Lelli, M.; Luchinat, C.; Mao, J.; Pintacuda, G. Ultrafast MAS Solid-State NMR Permits Extensive ^{13}C and ^{1}H Detection in Paramagnetic Metalloproteins. *Journal of the American Chemical Society* **2010**, *132*, 5558–5559.

(20) Ellett, J. D.; Griffin, R. G.; Waugh, J. S.; Spiess, H. W.; Grosescu, R.; Haeberlen, U.; Alexander, S.; Baram, A.; Luz, Z.; Campbell, R. F.; Meirovitch, E.; Freed, J. H.; Huang,

T. H.; Skarjune, R. P.; Wittebort, R. J.; Old-Field, E.; Pschorn, O.; Wemmer, D. E.; Ruben, D. J.; Pines, A.; Stimson, E. R.; Meinwaid, Y. C.; Smith, G. D.; Griffin, J. F.; Davis, J. H.; Jeffrey, K. R.; Bloom, M.; Valic, . I; Higgs, T. P. Rotational Jumps of the Tyrosine Side Chain in Crystalline Enkephalin. ^{2}H NMR Line Shapes for Aromatic Ring Motion in Solids. *J. Am. Chem. Soc* **1981**, *103*, 390–394.

(21) Hu, F.; Luo, W.; Hong, M. Mechanisms of Proton Conduction and Gating in Influenza M2 Proton Channels from Solid-State NMR. *Science* **2010**, *330*, 505–508.

(22) Li, S.; Hong, M. Protonation, Tautomerization, and Rotameric Structure of Histidine: A Comprehensive Study by Magic-Angle-Spinning Solid-State NMR. *Journal of the American Chemical Society* **2011**, *133*, 1534–1544.

(23) Gauto, D. F.; Macek, P.; Barducci, A.; Fraga, H.; Hessel, A.; Terauchi, T.; Gajan, D.; Miyanoiri, Y.; Boisbouvier, J.; Lichtenecker, R.; Kainosho, M.; Schanda, P. Aromatic Ring Dynamics, Thermal Activation, and Transient Conformations of a 468 kDa Enzyme by Specific ^{1}H-^{13}C Labeling and Fast Magic-Angle Spinning NMR. *Journal of the American Chemical Society* **2019**, *141*, 11183–11195.

(24) Hull, W. E.; Sykes, B. D. Fluorotyrosine Alkaline Phosphatase: Internal Mobility of Individual Tyrosines and the Role of Chemical Shift Anisotropy as a ^{19}F Nuclear Spin Relaxation Mechanism in Proteins. *Journal of Molecular Biology* **1975**, *98*, 121–153.

(25) Hull, W. E.; Sykes, B. D. Fluorotyrosine Alkaline Phosphatase. ^{19}F Nuclear Magnetic Resonance Relaxation Times and Molecular Motion of the Individual Fluorotyrosines. *Biochemistry* **1974**, *13*, 3431–3437.

(26) Boeszoermenyi, A.; Chhabra, S.; Dubey, A.; Radeva, D. L.; Burdzhiev, N. T.; Chanev, C. D.; Petrov, O. I.; Gelev, V. M.; Zhang, M.; Anklin, C.; Kovacs, H.; Wagner, G.; Kuprov, I.; Takeuchi, K.; Arthanari, H. Aromatic ^{19}F- ^{13}C TROSY: A Background-Free Approach to Probe Biomolecular Structure, Function, and Dynamics. *Nature Methods* **2019**, *16*, 333–340.

(27) Yee, A. A.; Savchenko, A.; Ignachenko, A.; Lukin, J.; Xu, X.; Skarina, T.; Evdokimova, E.; Liu, C. S.; Semesi, A.; Guido, V.; Edwards, A. M.; Arrowsmith, C. H. NMR and X-

Ray Crystallography, Complementary Tools in Structural Proteomics of Small Proteins. *Journal of the American Chemical Society* **2005**, *127*, 16512–16517.

(28) Kallen, J.; Spitzfaden, C.; Zurini, M. G. M.; Wider, G.; Widmer, H.; Wüthrich, K.; Walkinshaw, M. D. Structure of Human Cyclophilin and Its Binding Site for Cyclosporin A Determined by X-Ray Crystallography and NMR Spectroscopy. *Nature 1991 353:6341* **1991**, *353*, 276–279.

(29) Schirò, A.; Carlon, A.; Parigi, G.; Murshudov, G.; Calderone, V.; Ravera, E.; Luchinat, C. On the Complementarity of X-Ray and NMR Data. *Journal of Structural Biology: X* **2020**, *4*, 1–9.

(30) Theodorou, V.; Skobridis, K.; Alivertis, D.; Gerothanassis, I. P. Synthetic Methodologies in Organic Chemistry Involving Incorporation of [^{17}O] and [^{18}O] Isotopes. *Journal of Labelled Compounds and Radiopharmaceuticals* **2014**, *57*, 481–508.

(31) Rittenberg, D.; Ponticorvo, L. A Method for the Determination of the ^{18}O Concentration of the Oxygen of Organic Compounds. *The International Journal of Applied Radiation and Isotopes* **1956**, *1*, 208–214.

(32) Rittenberg, D.; Ponticorvo, L.; Borek, E. Studies on the Sources of the Oxygen of Proteins. *The Journal of biological chemistry* **1961**, *236*, 1769–1772.

(33) Steinschneider, A.; Burgar, M. I.; Buku, A.; Fiat, D. Labeling of Amino Acids and Peptides With Isotopic Oxygen As Followed By ^{17}O-N.M.R. *International Journal of Peptide and Protein Research* **1981**, *18*, 324–333.

(34) Pike, K. J.; Lemaitre, V.; Kukol, A.; Anupõld, T.; Samoson, A.; Howes, A. P.; Watts, A.; Smith, M. E.; Dupree, R. Solid-State ^{17}O NMR of Amino Acids. *Journal of Physical Chemistry B* **2004**, *108*, 9256–9263.

(35) Wong, A.; Pike, K. J.; Jenkins, R.; Clarkson, G. J.; Anupõld, T.; Howes, A. P.; Crout, D. H. G.; Samoson, A.; Dupree, R.; Smith, M. E. Experimental and Theoretical ^{17}O NMR Study of the Influence of Hydrogen-Bonding on C=O and O-H Oxygens in Carboxylic Solids. *Journal of Physical Chemistry A* **2006**, *110*, 1824–1835.

(36) Wu, G.; Yamada, K.; Dong, S.; Grondey, H. Intermolecular Hydrogen-Bonding Effects on the Amide Oxygen Electric- Field-Gradient and Chemical Shielding Tensors of Benzamide . *Journal of the American Chemical Society* **2000**, *122*, 4215–4216.

(37) Dong, S.; Ida, R.; Wu, G. A Combined Experimental and Theoretical ^{17}O NMR Study of Crystalline Urea: An Example of Large Hydrogen-Bonding Effects. *Journal of Physical Chemistry A* **2000**, *104*, 11194–11202.

(38) Lin, B.; Hung, I.; Gan, Z.; Chien, P. H.; Spencer, H. L.; Smith, S. P.; Wu, G. ^{17}O NMR Studies of Yeast Ubiquitin in Aqueous Solution and in the Solid State. *ChemBioChem* **2020**, *21*, 1–5.

(39) Paulino, J.; Yi, M.; Hung, I.; Gan, Z.; Wang, X.; Chekmenev, E. Y.; Zhou, H. X.; Cross, T. A. Functional Stability of Water Wire-Carbonyl Interactions in an Ion Channel. *Proceedings of the National Academy of Sciences of the United States of America* **2020**, *117*, 11908-11915.

(40) Yamada, K.; Yamazaki, T.; Asanuma, M.; Hirota, H.; Yamamoto, N.; Kajihara, Y. Solid-State ^{17}O NMR in Biological Solids: Efficient ^{17}O Labeling of Amino Acids and Peptides. *Chemistry Letters* **2007**, *36*, 192–193.

(41) Špačková, J.; Fabra, C.; Mittelette, S.; Gaillard, E.; Chen, C. H.; Cazals, G.; Lebrun, A.; Sene, S.; Berthomieu, D.; Chen, K.; Gan, Z.; Gervais, C.; Métro, T. X.; Laurencin, D. Unveiling the Structure and Reactivity of Fatty-Acid Based (Nano)Materials Thanks to Efficient and Scalable ^{17}O and ^{18}O-Isotopic Labeling Schemes. *Journal of the American Chemical Society* **2020**, *142*, 21068–21081.

(42) Métro, T. X.; Gervais, C.; Martinez, A.; Bonhomme, C.; Laurencin, D. Unleashing the Potential of ^{17}O NMR Spectroscopy Using Mechanochemistry. *Angewandte Chemie - International Edition* **2017**, *56*, 6803–6807.

(43) Chen, C. H.; Gaillard, E.; Mentink-Vigier, F.; Chen, K.; Gan, Z.; Gaveau, P.; Rebière, B.; Berthelot, R.; Florian, P.; Bonhomme, C.; Smith, M. E.; Métro, T. X.; Alonso, B.; Laurencin, D. Direct ^{17}O Isotopic Labeling of Oxides Using Mechanochemistry. *Inorganic Chemistry* **2020**, *59*, 13050–13066.

(44) Chen, C. H.; Goldberga, I.; Gaveau, P.; Mittelette, S.; Špačková, J.; Mullen, C.; Petit, I.; Métro, T. X.; Alonso, B.; Gervais, C.; Laurencin, D. Looking into the Dynamics of Molecular Crystals of Ibuprofen and Terephthalic Acid Using ^{17}O and ^{2}H Nuclear Magnetic Resonance Analyses. *Magnetic Resonance in Chemistry* **2021**, 1–16.

(45) Seyfried, M. S.; Lauber, B. S.; Luedtke, N. W. Multiple-Turnover Isotopic Labeling of Fmoc- and Boc-Protected Amino Acids with Oxygen Isotopes. *Organic Letters* **2010**, *12*, 104–106.

(46) Keeler, E. G.; Michaelis, V. K.; Colvin, M. T.; Hung, I.; Gor'Kov, P. L.; Cross, T. A.; Gan, Z.; Griffin, R. G. ^{17}O MAS NMR Correlation Spectroscopy at High Magnetic Fields. *Journal of the American Chemical Society* **2017**, *139*, 17953–17963.

(47) Klein, B. A.; Tkachuk, D. G.; Terskikh, V. V.; Michaelis, V. K. Expanding the NMR Toolkit for Biological Solids: Oxygen-17 Enriched Fmoc-Amino Acids. *New Journal of Chemistry* **2021**, *45*, 12384–12398.

(48) Ha, M.; Nader, S.; Pawsey, S.; Struppe, J.; Monette, M.; Mansy, S. S.; Boekhoven, J.; Michaelis, V. K. Racing toward Fast and Effective ^{17}O Isotopic Labeling and Nuclear Magnetic Resonance Spectroscopy of N-Formyl-MLF-OH and Associated Building Blocks. *Journal of Physical Chemistry B* **2021**, *125*, 11916–11926.

(49) Carnahan, S. L.; Lampkin, B. J.; Naik, P.; Hanrahan, M. P.; Slowing, I. I.; Vanveller, B.; Wu, G.; Rossini, A. J. Probing O-H Bonding through Proton Detected ^{1}H- ^{17}O Double Resonance Solid-State NMR Spectroscopy. *Journal of the American Chemical Society* **2019**, *141*, 441–450.

(50) Prasad, S.; Clark, T. M.; Sharma, R.; Kwak, H.-T.; Grandinetti, P. J.; Zimmermann, H. A Combined ^{17}O RAPT and MQ-MAS NMR Study of L-Leucine. *Solid State Nuclear Magnetic Resonance* **2006**, *29*, 119–124.

(51) Yamada, K.; Shimizu, T.; Tansho, M.; Nemoto, T.; Asanuma, M.; Yoshida, M.; Yamazaki, T.; Hirota, H. Solid-State ^{17}O NMR Study of the Electric-Field-Gradient and Chemical Shielding Tensors in Polycrystalline Amino Acids. *Magnetic Resonance in Chemistry* **2007**, *45*, 547–556.

(52) Yamada, K.; Nemoto, T.; Asanuma, M.; Honda, H.; Yamazaki, T.; Hirota, H. Both Experimental and Theoretical Investigations of Solid-State ^{17}O NMR for l-Valine and l-Isoleucine. *Solid State Nuclear Magnetic Resonance* **2006**, *30*, 182–191.

(53) Keeler, E. G.; Michaelis, V. K.; Wilson, C. B.; Hung, I.; Wang, X.; Gan, Z.; Griffin, R. G. High-Resolution ^{17}O NMR Spectroscopy of Structural Water. *Journal of Physical Chemistry B* **2019**, *123*, 3061–3067.

(54) Jardón-Álvarez, D.; Bovee, M. O.; Baltisberger, J. H.; Grandinetti, P. J. Natural Abundance ^{17}O and ^{33}S Nuclear Magnetic Resonance Spectroscopy in Solids Achieved through Extended Coherence Lifetimes. *Physical Review B* **2019**, *100*, 140103.

(55) Carver, T. R.; Slichter, C. P. Polarization of Nuclear Spins in Metals. *Physical Review* **1953**, *92*, 212–213.

(56) Gerfen, G. J.; Becerra, L. R.; Hall, D. A.; Griffin, R. G.; Temkin, R. J.; Singel, D. J. High Frequency (140 GHz) Dynamic Nuclear Polarization: Polarization Transfer to a Solute in Frozen Aqueous Solution. *The Journal of Chemical Physics* **1995**, *102*, 9494–9497.

(57) Blanc, F.; Sperrin, L.; Jefferson, D. A.; Pawsey, S.; Rosay, M.; Grey, C. P. Dynamic Nuclear Polarization Enhanced Natural Abundance ^{17}O Spectroscopy. *Journal of the American Chemical Society* **2013**, *135*, 2975–2978.

(58) Perras, F. A.; Kobayashi, T.; Pruski, M. Natural Abundance ^{17}O DNP Two-Dimensional and Surface-Enhanced NMR Spectroscopy. *Journal of the American Chemical Society* **2015**, *137*, 8336–8339.

(59) Brownbill, N. J.; Gajan, D.; Lesage, A.; Emsley, L.; Blanc, F. Oxygen-17 Dynamic Nuclear Polarisation Enhanced Solid-State NMR Spectroscopy at 18.8 T. *Chemical Communications* **2017**, *53*, 2563–2566.

(60) Perras, F. A.; Boteju, K. C.; Slowing, I. I.; Sadow, A. D.; Pruski, M. Direct ^{17}O Dynamic Nuclear Polarization of Single-Site Heterogeneous Catalysts. *Chemical Communications* **2018**, *54*, 3472–3475.

(61) Wolf, T.; Kumar, S.; Singh, H.; Chakrabarty, T.; Aussenac, F.; Frenkel, A. I.; Major, D.

T.; Leskes, M. Endogenous Dynamic Nuclear Polarization for Natural Abundance ^{17}O and Lithium NMR in the Bulk of Inorganic Solids. *Journal of the American Chemical Society* **2019**, *141*, 451–462.

(62) Carnevale, D.; Mouchaham, G.; Wang, S.; Baudin, M.; Serre, C.; Bodenhausen, G.; Abergel, D. Natural Abundance Oxygen-17 Solid-State NMR of Metal Organic Frameworks Enhanced by Dynamic Nuclear Polarization. *Physical Chemistry Chemical Physics* **2021**, *23*, 2245–2251.

(63) Chen, J.; Wu, X. P.; Hope, M. A.; Qian, K.; Halat, D. M.; Liu, T.; Li, Y.; Shen, L.; Ke, X.; Wen, Y.; Du, J. H.; Magusin, P. C. M. M.; Paul, S.; Ding, W.; Gong, X. Q.; Grey, C. P.; Peng, L. Polar Surface Structure of Oxide Nanocrystals Revealed with Solid-State NMR Spectroscopy. *Nature Communications* **2019**, *10*.

(64) Michaelis, V. K.; Markhasin, E.; Daviso, E.; Herzfeld, J.; Griffin, R. G. Dynamic Nuclear Polarization of Oxygen-17. *Journal of Physical Chemistry Letters* **2012**, *3*, 2030–2034.

(65) Michaelis, V. K.; Corzilius, B.; Smith, A. A.; Griffin, R. G. Dynamic Nuclear Polarization of ^{17}O: Direct Polarization. *Journal of Physical Chemistry B* **2013**, *117*, 14894–14906.

(66) Nagashima, H.; Trébosc, J.; Kon, Y.; Lafon, O.; Amoureux, J.-P. Efficient Transfer of DNP-Enhanced ^{1}H Magnetization to Half-Integer Quadrupolar Nuclei in Solids at Moderate Spinning Rate. *Magnetic Resonance in Chemistry* **2021**, *59*, 920–939.

(67) Rosay, M.; Tometich, L.; Pawsey, S.; Bader, R.; Schauwecker, R.; Blank, M.; Borchard, P. M.; Cauffman, S. R.; Felch, K. L.; Weber, R. T.; Temkin, R. J.; Griffin, R. G.; Maas, W. E. Solid-State Dynamic Nuclear Polarization at 263 GHz: Spectrometer Design and Experimental Results. *Physical Chemistry Chemical Physics* **2010**, *12*, 5850–5860.

(68) Michaelis, V. K.; Keeler, E. G.; Ong, T. C.; Craigen, K. N.; Penzel, S.; Wren, J. E. C.; Kroeker, S.; Griffin, R. G. Structural Insights into Bound Water in Crystalline Amino Acids: Experimental and Theoretical ^{17}O NMR. *Journal of Physical Chemistry B* **2015**, *119*, 8024–8036.

(69) Yamada, K. *Recent Applications of Solid-State ^{17}O NMR*; Academic Press, 2010; Vol. 70.

(70) Wong, A.; Poli, F. *Solid-State ^{17}O NMR Studies of Biomolecules*, 1st ed.; Elsevier Ltd., 2014; Vol. 83.

(71) Wu, G. ^{17}O NMR Studies of Organic and Biological Molecules in Aqueous Solution and in the Solid State. *Progress in Nuclear Magnetic Resonance Spectroscopy* **2019**, *114–115*, 135–191.

(72) Wong, A.; Howes, A. P.; Pike, K. J.; Lemaître, V.; Watts, A.; Anupõld, T.; Past, J.; Samoson, A.; Dupree, R.; Smith, M. E. New Limits for Solid-State ^{17}O NMR Spectroscopy: Complete Resolution of Multiple Oxygen Sites in a Simple Biomolecule. *Journal of the American Chemical Society* **2006**, *128*, 7744–7745.

(73) Samoson, A.; Lippmaa, E.; Pines, A. High Resolution Solid-State N.M.R. Averaging of Second-Order Effects by Means of a Double-Rotor. *Molecular Physics* **1988**, *65*, 1013–1018.

(74) Frydman, L.; Harwood, J. S. Isotropic Spectra of Half-Integer Quadrupolar Spins from Bidimensional Magic-Angle Spinning NMR. *Am. Ceram. Soc. Bull* **1995**, *117*, 5367–5368.

(75) Gan, Z. Isotropic NMR Spectra of Half-Integer Quadrupolar Nuclei Using Satellite Transitions and Magic-Angle Spinning. *Journal of the American Chemical Society* **2000**, *122*, 3242–3243.

(76) Wu, G.; Rovnyak, D.; Huang, P. C.; Griffin, R. G. High-Resolution Oxygen-17 NMR Spectroscopy of Solids by Multiple-Quantum Magic-Angle-Spinning. *Chemical Physics Letters* **1997**, *277*, 79–83.

(77) Wu, G.; Rovnyak, D.; Griffin, R. G. Quantitative Multiple-Quantum Magic-Angle-Spinning NMR Spectroscopy of Quadrupolar Nuclei in Solids. *Journal of the American Chemical Society* **1996**, *118*, 9326–9332.

(78) Lemaître, V.; Smith, M. E.; Watts, A. A Review of Oxygen-17 Solid-State NMR of Organic Materials—towards Biological Applications. *Solid State Nuclear Magnetic Resonance* **2004**, *26*, 215–235.

(79) Gerothanassis, I. P. Oxygen-17 NMR Spectroscopy: Basic Principles and Applications (Part I). *Progress in Nuclear Magnetic Resonance Spectroscopy* **2010**, *56*, 95–197.

(80) Wu, G. Solid-State ^{17}O NMR Studies of Organic and Biological Molecules: Recent Advances and Future Directions. *Solid State Nuclear Magnetic Resonance*. Elsevier B.V. February 1, 2016, pp 1–14.

(81) Palmer, J.; Wu, G. Recent Developments in ^{17}O NMR Studies of Organic and Biological Molecules in the Solid State. In *Annual Reports on NMR Spectroscopy*; Academic Press, 2021; Vol. 103, pp 1–46.

(82) Muniyappan, S.; Lin, Y.; Lee, Y.-H.; Kim, J. H. ^{17}O NMR Spectroscopy: A Novel Probe for Characterizing Protein Structure and Folding. *Biology* **2021**, *10*, 453.

(83) Rowlands, L. J.; Marks, A.; Sanderson, J. M.; Law, R. V. ^{17}O NMR Spectroscopy as a Tool to Study Hydrogen Bonding of Cholesterol in Lipid Bilayers. *Chemical Communications* **2020**, *56*, 14499–14502.

(84) Lu, J.; Hung, I.; Brinkmann, A.; Gan, Z.; Kong, X.; Wu, G. Solid-State ^{17}O NMR Reveals Hydrogen-Bonding Energetics: Not All Low-Barrier Hydrogen Bonds Are Strong. *Angewandte Chemie - International Edition* **2017**, *56*, 6166–6170.

(85) Keeler, E. G.; Michaelis, V. K.; Griffin, R. G. ^{17}O NMR Investigation of Water Structure and Dynamics. *Journal of Physical Chemistry B* **2016**, *120*, 7851–7858.

(86) Rees, G. J.; Day, S. P.; Barnsley, K. E.; Iuga, D.; Yates, J. R.; Wallis, J. D.; Hanna, J. V. Measuring Multiple ^{17}O-^{13}C: J -Couplings in Naphthalaldehydic Acid: A Combined Solid State NMR and Density Functional Theory Approach. *Physical Chemistry Chemical Physics* **2020**, *22*, 3400–3413.

(87) Hung, I.; Uldry, A.-C.; Becker-Baldus, J.; Webber, A. L.; Wong, A.; Smith, M. E.; Joyce, S. A.; Yates, J. R.; Pickard, C. J.; Dupree, R.; Brown, S. P. Probing Heteronuclear ^{15}N− ^{17}O and ^{13}C− ^{17}O Connectivities and Proximities by Solid-State NMR Spectroscopy. *Journal of the American Chemical Society* **2009**, *131*, 1820–1834.

(88) Chopin, L.; Vega, S.; Gullion, T. A MAS NMR Method for Measuring ^{13}C-^{17}O Distances.

Journal of the American Chemical Society **1998**, *120*, 4406–4409.

(89) Goldbourt, A.; Vega, S.; Gullion, T.; Vega, A. J. Interatomic Distance Measurement in Solid-State NMR between a Spin-1/2 and a Spin-5/2 Using a Universal REAPDOR Curve. *Journal of the American Chemical Society* **2003**, *125*, 11194–11195.

(90) Chen, L.; Lu, X.; Wang, Q.; Lafon, O.; Trébosc, J.; Deng, F.; Amoureux, J. P. Distance Measurement between a Spin-1/2 and a Half-Integer Quadrupolar Nuclei by Solid-State NMR Using Exact Analytical Expressions. *Journal of Magnetic Resonance* **2010**, *206*, 269–273.

(91) Hung, I.; Gan, Z.; Wu, G. Two- And Three-Dimensional ^{13}C-^{17}O Heteronuclear Correlation NMR Spectroscopy for Studying Organic and Biological Solids. *Journal of Physical Chemistry Letters* **2021**, *12*, 8897–8902.

(92) Levitt, M. H. *Spin Dynamics: Basics of Nuclear Magnetic Resonance*, Second.; Wiley & Sons Ltd: Chichester, UK, 2008.

(93) Slichter, C. P. *Principles of Magnetic Resonance*, 3rd Enlarg.; Cardona, M., Fulde, P., von Klitzing, K., Queisser, H.-J., Lotsch, Helmut, K. V., Eds.; Springer, 1990.

(94) Michaelis, V. K.; Griffin, R. G.; Corzilius, B.; Vega, S. *Handbook of High Field Dynamic Nuclear Polarization*; Michaelis, V. K., Griffin, R. G., Corzilius, B., Vega, S., Eds.; Wiley, 2020.

(95) Ernst, R. R.; Anderson, W. A. Application of Fourier Transform Spectroscopy to Magnetic Resonance. *Review of Scientific Instruments* **1966**, *37*, 93–102.

(96) Brinkmann, A. Introduction to Average Hamiltonian Theory. I. Basics. *Concepts in Magnetic Resonance Part A: Bridging Education and Research* **2016**, *45A*, 1–19.

(97) Smith, S. A.; Palke, W. E.; Gerig, J. T. The Hamiltonians of NMR. Part I. *Concepts in Magnetic Resonance* **1992**, *4*, 107–144.

(98) Klinowski, J. NMR of Solids, Theory. In *Encyclopedia of Spectroscopy and Spectrometry*; Elsevier, 2016; pp 175–180.

(99) Andrew, E. R.; Bradbury, A.; Eades, R. G. Removal of Dipolar Broadening of Nuclear Magnetic Resonance Spectra of Solids by Specimen Rotation. *Nature* **1959**, *183*, 1802–1803.

(100) Andrew, E. R. Magic Angle Spinning in Solid State n.m.r. Spectroscopy. *Philosophical Transactions of the Royal Society of London. Series A, Mathematical and Physical Sciences* **1981**, *299*, 505–520.

(101) Gerstein, B. C. High Resolution Solid State Nmr and Magic Angle Spinning. *Advances in Colloid and Interface Science* **1985**, *23*, 45–66.

(102) Bennett, A. E.; Rienstra, C. M.; Auger, M.; Lakshmi, K. V.; Griffin, R. G. Heteronuclear Decoupling in Rotating Solids. *The Journal of Chemical Physics* **1995**, *103*, 6951–6958.

(103) Shaka, A. J.; Keeler, J. Broadband Spin Decoupling in Isotropic-Liquids. *Progress in Nuclear Magnetic Resonance Spectroscopy* **1987**, *19*, 47–129.

(104) Fung, B. M.; Khitrin, A. K.; Ermolaev, K. An Improved Broadband Decoupling Sequence for Liquid Crystals and Solids. *Journal of Magnetic Resonance* **2000**, *142*, 97–101.

(105) Griffiths, J. M.; Griffin, R. G. Nuclear Magnetic Resonance Methods for Measuring Dipolar Couplings in Rotating Solids. *Analytica Chimica Acta* **1993**, *283*, 1081–1101.

(106) Griffin, R. G. Dipolar Recoupling in MAS Spectra of Biological Solids. *Nature Structural Biology* **1998**, *5*, 508–512.

(107) Zhao, X.; Edén, M.; Levitt, M. H. Recoupling of Heteronuclear Dipolar Interactions in Solid-State NMR Using Symmetry-Based Pulse Sequences. *Chemical Physics Letters* **2001**, *342*, 353–361.

(108) Gullion, T. Detecting ^{13}C-^{17}O Dipolar Interactions by Rotational-Echo, Adiabatic-Passage, Double-Resonance NMR. *Journal of Magnetic Resonance, Series A* **1995**, *117*, 326–329.

(109) Jameson, C. J. Understanding NMR Chemical Shifts. *Annual Review of Physical Chemistry* **1996**, *47*, 135–169.

(110) Morcombe, C. R.; Zilm, K. W. Chemical Shift Referencing in MAS Solid State NMR.

Journal of Magnetic Resonance **2003**, *162*, 479–486.

(111) Herzfeld, J.; Berger, A. E. Sideband Intensities in NMR Spectra of Samples Spinning at the Magic Angle. *The Journal of Chemical Physics* **1980**, *73*, 6021–6030.

(112) Mason, J. Conventions for the Reporting of Nuclear Magnetic Shielding (or Shift) Tensors Suggested by Participants in the NATO ARW on NMR Shielding Constants at the University of Maryland, College Park, July 1992. *Solid State Nuclear Magnetic Resonance* **1993**, *2*, 285–288.

(113) Fernandez, C.; Pruski, M. Probing Quadrupolar Nuclei by Solid-State NMR Spectroscopy: Recent Advances. *Topics in Current Chemistry* **2012**, *306*, 119–188.

(114) Pyykkö, P. Year-2017 Nuclear Quadrupole Moments. *Molecular Physics* **2018**, *116*, 1328–1338.

(115) Man, P. P. Chapter 1: Basic Principles. In *NMR of Quadrupolar Nuclei in Solid Materials*; Wasylishen, R. E., Ashbrook, S. E., Wimperis, S., Eds.; John Wiley & Sons, Ltd: Chichester, UK, 2012; pp 3–16.

(116) Vega, A. J. Chapter 2: Quadrupolar Nuclei in Solids. In *NMR of Quadrupolar Nuclei in Solid Materials*; Wasylishen, R. E., Ashbrook, S. E., Wimperis, S., Eds.; John Wiley & Sons, Ltd, 2012; pp 17–44.

(117) Smith, J. A. S. Nuclear Quadrupole Resonance Spectroscopy: General Principles. *Journal of Chemical Education* **1971**, *48*, 39–49.

(118) Bryce, D. L.; Wasylishen, R. E. Quadrupolar Nuclei in Solids: Influence of Different Interactions on Spectra. In *Encyclopedia of Magnetic Resonance*; John Wiley & Sons, Ltd: Chichester, UK, 2011; pp 63–73.

(119) Grandinetti, P. J.; Ash, J. T.; Trease, N. M. Symmetry Pathways in Solid-State NMR. *Progress in Nuclear Magnetic Resonance Spectroscopy* **2011**, *59*, 121–196.

(120) Andrew, E. R.; Szczesniak, E. A Historical Account of NMR in the Solid State. *Progress in Nuclear Magnetic Resonance Spectroscopy* **1995**, *28*, 11–36.

(121) Lowe, I. J. Free Induction Decays of Rotating Solids. *Physical Review Letters* **1959**, *2*, 285–287.

(122) Nishiyama, Y. Solid-State NMR under Ultrafast MAS Rate of 40-120 KHz. In *Experimental Approaches of NMR Spectroscopy: Methodology and Application to Life Science and Materials Science*; Springer, Singapore, 2017; pp 171–195.

(123) Laage, S.; Sachleben, J. R.; Steuernagel, S.; Pierattelli, R.; Pintacuda, G.; Emsley, L. Fast Acquisition of Multi-Dimensional Spectra in Solid-State NMR Enabled by Ultra-Fast MAS. *Journal of Magnetic Resonance* **2009**, *196*, 133–141.

(124) Hahn, E. L. Spin Echoes. *Phys. Rev* **1950**, *80*, 580–601.

(125) Bodart, P. R.; Amoureux, J.-P.; Dumazy, Y.; Lefort, R. Theoretical and Experimental Study of Quadrupolar Echoes for Half-Integer Spins in Static Solid-State NMR. *Molecular Physics* **2000**, *98*, 1545–1551.

(126) Eichele, K. WSolids1 NMR Simulation Package, 1.21.3. Universität Tübingen 2015.

(127) Hohenberg, P.; Kohn, W. Inhomogeneous Electron Gas. *Physical Review* **1964**, *136*, B864.

(128) Schreckenbach, G.; Ziegler, T. Calculation of NMR Shielding Tensors Based on Density Functional Theory and a Scalar Relativistic Pauli-Type Hamiltonian. The Application to Transition Metal Complexes. *International Journal of Quantum Chemistry* **1997**, *61*, 899–918.

(129) Wolff, S. K.; Ziegler, T. Calculation of DFT-GIAO NMR Shifts with the Inclusion of Spin-Orbit Coupling. *Journal of Chemical Physics* **1998**, *109*, 895–905.

(130) Van Lenthe, E.; Baerends, E. J. Density Functional Calculations of Nuclear Quadrupole Coupling Constants in the Zero-Order Regular Approximation for Relativistic Effects. *Journal of Chemical Physics* **2000**, *112*, 8279–8292.

(131) te Velde, G.; Bickelhaupt, F. M.; Baerends, E. J.; Fonseca Guerra, C.; van Gisbergen, S. J. A. A.; Snijders, J. G.; Ziegler, T. Chemistry with ADF. *Journal of Computational*

Chemistry **2001**, *22*, 931–967.

(132) Baerends, E. J. ADF 2019.3, SCM, Theoretical Chemistry. Vrije Universiteit: Amsterdam, The Netherlands 2014.

(133) Fonseca Guerra, C.; Snijders, J. G.; te Velde, G.; Baerends, E. J. Towards an Order-. *Theoretical Chemistry Accounts* **1998**, *99*, 391.

(134) Vosko, S. H.; Wilk, L.; Nusair, M. Accurate Spin-Dependent Electron Liquid Correlation Energies for Local Spin Density Calculations: A Critical Analysis. *Canadian Journal of Physics* **1980**, *58*, 1200–1211.

(135) Becke, A. D. Density-Functional Exchange-Energy Approximation with Correct Asymptotic Behavior. *Physical Review A* **1988**, *38*, 3098–3100.

(136) Perdew, J. P. Density-Functional Approximation for the Correlation Energy of the Inhomogeneous Electron Gas. *Physical Review B* **1986**, *33*, 8822–8824.

(137) Perdew, J. P. Erratum: Density-Functional Approximation for the Correlation Energy Ofthe Inhomogeneous Electron Gas. *Physical Review B* **1986**, *34*, 7406.

(138) Van Lenthe, E.; Baerends, E. J.; Snijders, J. G. Relativistic Total Energy Using Regular Approximations. *The Journal of Chemical Physics* **1994**, *101*, 9783–9792.

(139) Adiga, S.; Aebi, D.; Bryce, D. L. EFGShield - A Program for Parsing and Summarizing the Results of Electric Field Gradient and Nuclear Magnetic Shielding Tensor Calculations. *Canadian Journal of Chemistry* **2007**, *85*, 496–505.

(140) Pines, A.; Gibby, M. G.; Waugh, J. S. Proton-Enhanced Nuclear Induction Spectroscopy. A Method for High Resolution NMR of Dilute Spins in Solids. *The Journal of Chemical Physics* **1972**, *56*, 1776–1777.

(141) Yamada, K.; Hashizume, D.; Shimizu, T.; Deguchi, K. N-(Fluoren-9-Ylmethoxy-Carbon-Yl)-L-Isoleucine. *Acta Crystallographica Section E: Structure Reports Online* **2008**, *64*, o1533–o1533.

(142) Draper, E. R.; Morris, K. L.; Little, M. A.; Raeburn, J.; Colquhoun, C.; Cross, E. R.;

McDonald, T. O.; Serpell, L. C.; Adams, D. J. Hydrogels Formed from Fmoc Amino Acids. *CrystEngComm* **2015**, *17*, 8047–8057.

(143) Yamada, K.; Hashizume, D.; Shimizu, T.; Ohki, S.; Yokoyama, S. A Solid-State ^{17}O NMR, X-Ray, and Quantum Chemical Study of N-α-Fmoc-Protected Amino Acids. *Journal of Molecular Structure* **2008**, *888*, 187–196.

(144) Nour, S.; Widdifield, C. M.; Kobera, L.; Burgess, K. M. N.; Errulat, D.; Terskikh, V. V; Bryce, D. L. Oxygen-17 NMR Spectroscopy of Water Molecules in Solid Hydrates. *Canadian Journal of Chemistry* **2016**, *94*, 189–197.

(145) Tang, C.; Smith, A. M.; Collins, R. F.; Ulijn, R. V; Saiani, A. Fmoc-Diphenylalanine Self-Assembly Mechanism Induces Apparent pKa Shifts. *Langmuir* **2009**, *25*, 9447–9453.

(146) Rossini, E.; Bochevarov, A. D.; Knapp, E. W. Empirical Conversion of pKa Values between Different Solvents and Interpretation of the Parameters: Application to Water, Acetonitrile, Dimethyl Sulfoxide, and Methanol. *ACS Omega* **2018**, *3*, 1653–1662.

(147) Yates, J. R.; Pickard, C. J.; Payne, M. C.; Dupree, R.; Profeta, M.; Mauri, F. Theoretical Investigation of Oxygen-17 NMR Shielding and Electric Field Gradients in Glutamic Acid Polymorphs. *Journal of Physical Chemistry A* **2004**, *108*, 6032–6037.

(148) Gervais, C.; Dupree, R.; Pike, K. J.; Bonhomme, C.; Profeta, M.; Pickard, C. J.; Mauri, F. Combined First-Principles Computational and Experimental Multinuclear Solid-State NMR Investigation of Amino Acids. *Journal of Physical Chemistry A* **2005**, *109*, 6960–6969.

(149) Shigeki Kuroki; Kazuo Yamauchi; Isao Ando; Akira Shoji; Takuo Ozaki. ^{17}O-Isotope Labeling and Hydrogen-Bonded Structure Investigation in Peptides and Polypeptides by Solid State ^{17}O NMR. *Current Organic Chemistry* **2001**, *5*, 1001–1015.

(150) Yamada, K.; Dong, S.; Wu, G. Solid-State ^{17}O NMR Investigation of the Carbonyl Oxygen Electric-Field-Gradient Tensor and Chemical Shielding Tensor in Amides. *Journal of the American Chemical Society* **2000**, *122*, 11602–11609.

(151) Zhu, J.; Lau, J. Y. C.; Wu, G. A Solid-State ^{17}O NMR Study of L-Tyrosine in Different

Ionization States: Implications for Probing Tyrosine Side Chains in Proteins. *Journal of Physical Chemistry B* **2010**, *114*, 11681–11688.

(152) Yamada, K.; Shimizu, T.; Yoshida, M.; Asanuma, M.; Tansho, M.; Nemoto, T.; Yamazaki, T.; Hirota, H. Solid-State ^{17}O NMR Study of Small Biological Compounds. *Zeitschrift fur Naturforschung - Section B Journal of Chemical Sciences* **2007**, *62*, 1422–1432.

(153) Wu, G. Oxygen-17 NMR Studies of Organic and Biological Molecules. *Encyclopedia of Magnetic Resonance* **2011**.

(154) Martin, R. W.; Zilm, K. W. Preparation of Protein Nanocrystals and Their Characterization by Solid State NMR. *Journal of Magnetic Resonance* **2003**, *165*, 162–174.

(155) Gregory, R. B.; Gangoda, M.; Gilpin, R. K.; Su, W. The Influence of Hydration on the Conformation of Lysozyme Studied by Solid-state ^{13}C-NMR Spectroscopy. *Biopolymers* **1993**, *33*, 513–519.

(156) McDowell, L. M.; Schaefer, J. High-Resolution NMR of Biological Solids. *Current Opinion in Structural Biology* **1996**, *6*, 624–629.

(157) Wasylishen, R. E.; Bryce, D. L. A Revised Experimental Absolute Magnetic Shielding Scale for Oxygen. *Journal of Chemical Physics* **2002**, *117*, 10061–10066.

(158) Pople., J. A.; Beveridge, D. L. Approximate Molecular Orbital Theory for Inorganic Molecules. In *Approximate Molecular Orbital Theory*; McGraw-Hill Book Company: New York, 1970; pp 110–113.

(159) Xing, P.; Li, P.; Chen, H.; Hao, A.; Zhao, Y. Understanding Pathway Complexity of Organic Micro/Nanofiber Growth in Hydrogen-Bonded Coassembly of Aromatic Amino Acids. *ACS Nano* **2017**, *11*, 4206–4216.

(160) Yamada, K.; Hashizume, D.; Shimizu, T. N-(Fluoren-9-Ylmethoxy-Carbon-Yl)-l-Leucine. *Acta Crystallographica Section E: Structure Reports Online* **2008**, *64*.

(161) Balbirnie, M.; Grothe, R.; Eisenberg, D. S. An Amyloid-Forming Peptide from the Yeast Prion Sup35 Reveals a Dehydrated β-Sheet Structure for Amyloid. *Proceedings of the National Academy of Sciences of the United States of America* **2001**, *98*, 2375–2380.

(162) Liebman, S. W.; Derkatch, I. L. The Yeast [PSI+] Prion: Making Sense of Nonsense. *Journal of Biological Chemistry* **1999**, *274*, 1181–1184.

(163) Krishnan, R.; Lindquist, S. L. Structural Insights into a Yeast Prion Illuminate Nucleation and Strain Diversity. *Nature* **2005**, *435*, 765–772.

(164) Van Der Wel, P. C. A.; Lewandowski, J. R.; Griffin, R. G. Solid-State NMR Study of Amyloid Nanocrystals and Fibrils Formed by the Peptide GNNQQNY from Yeast Prion Protein Sup35p. *Journal of the American Chemical Society* **2007**, *129*, 5117–5130.

(165) Nelson, R.; Sawaya, M. R.; Balbirnie, M.; Madsen, A.; Riekel, C.; Grothe, R.; Eisenberg, D. Structure of the Cross-β Spine of Amyloid-like Fibrils. *Nature* **2005**, *435*, 773–778.

(166) Sawaya, M. R.; Sambashivan, S.; Nelson, R.; Ivanova, M. I.; Sievers, S. A.; Apostol, M. I.; Thompson, M. J.; Balbirnie, M.; Wiltzius, J. J. W.; McFarlane, H. T.; Madsen, A.; Riekel, C.; Eisenberg, D. Atomic Structures of Amyloid Cross-β Spines Reveal Varied Steric Zippers. *Nature* **2007**, *447*, 453–457.

(167) Diaz-Avalos, R.; Long, C.; Fontano, E.; Balbirnie, M.; Grothe, R.; Eisenberg, D.; Caspar, D. L. D. Cross-Beta Order and Diversity in Nanocrystals of an Amyloid-Forming Peptide. *Journal of Molecular Biology* **2003**, *330*, 1165–1175.

(168) Debelouchina, G. T.; Bayro, M. J.; Van Der Wel, P. C. A.; Caporini, M. A.; Barnes, A. B.; Rosay, M.; Maas, W. E.; Griffin, R. G. Dynamic Nuclear Polarization-Enhanced Solid-State NMR Spectroscopy of GNNQQNY Nanocrystals and Amyloid Fibrils. *Physical Chemistry Chemical Physics* **2010**, *12*, 5911–5919.

(169) Van Der Wel, P. C. A.; Lewandowski, J. R.; Griffin, R. G. Structural Characterization of GNNQQNY Amyloid Fibrils by Magic Angle Spinning NMR. *Biochemistry* **2010**, *49*, 9457–9469.

(170) Van Der Wel, P. C. A.; Hu, K. N.; Lewandowski, J.; Griffin, R. G. Dynamic Nuclear

Polarization of Amyloidogenic Peptide Nanocrystals: GNNQQNY, a Core Segment of the Yeast Prion Protein Sup35p. *Journal of the American Chemical Society* **2006**, *128*, 10840–10846.

(171) Ozef, J.; Lewandowski, R.; Van Der Wel, P. C. A.; Rigney, M.; Grigorieff, N.; Griffin, R. G.; Structural Complexity of a Composite Amyloid Fibril. *J. Am. Chem. Soc* **2011**, *133*, 14686–14698.

(172) Sawaya, M. R.; Rodriguez, J.; Cascio, D.; Collazo, M. J.; Shi, D.; Reyes, F. E.; Hattne, J.; Gonen, T.; Eisenberg, D. S. Ab Initio Structure Determination from Prion Nanocrystals at Atomic Resolution by MicroED. *Proceedings of the National Academy of Sciences of the United States of America* **2016**, *113*, 11232–11236.